NMR OF HPMCAS/ACETONE MIXTURES TO CHARACTERIZE CONCENTRATION AND TEMPERATURE DEPENDENT MOLECULAR DYNAMICS AND INFORM SDD DROPLET DRYING MODELS

by

Nathan Hu Williamson

A thesis submitted in partial fulfillment
of the requirements for the degree

of

Master of Science

in

Chemical Engineering

MONTANA STATE UNIVERSITY
Bozeman, Montana

August 2014

DEDICATION

This thesis is dedicated to Mom, Trina and Julie: I couldn’t have done it without your support.

TABLE OF CONTENTS

TABLE OF CONTENTS - CONTINUED

LIST OF TABLES

Table Page

LIST OF FIGURES

Figure Page

LIST OF FIGURES – CONTINUED

Figure Page

LIST OF FIGURES – CONTINUED

Figure Page

ABSTRACT

Hydroxypropyl methylcellulose acetate succinate (HPMCAS)-based spray-dried dispersions (SDDs) have been shown to offer significant bioavailability enhancement for drugs with low aqueous solubility. However, the impact of macroscale process conditions on microscale droplet drying and the impact of droplet drying history on SDD physical stability, dissolution performance and particle properties are not well understood. Mass transfer to the droplet surface is diffusion limited, and quantifying the mutual diffusivity over the solvent content and wet-bulb temperatures experienced during drying is crucial to modeling droplet drying. This research used nuclear magnetic resonance (NMR) to probe the concentration and temperature dependence of molecular scale interactions within binary systems of HPMCAS polymer and acetone. This data can be incorporated into SDD droplet drying models.

Following the generalized droplet drying model of Handscomb and Kraft [1], a specific SDD modeling procedure was developed. A preliminary form was coded in MATLAB using the finite difference method to approximate the drying time-dependent solvent concentration profiles over the changing droplet radius based on the governing equation for mass conservation.

Mixtures of HPMCAS with acetone and wet placebo SDD were tested using high-field NMR. Pulsed gradient stimulated echo (PGSTE) NMR experiments resolved self-diffusion of solvent and polymer. Solvent concentration dependence of the mutual diffusivity was related to a free-volume fit of the acetone self-diffusivity. Multidimensional T_1-T_2 correlation and T_2-T_2 exchange experiments separated proton populations based on correlations of spin-lattice T_1 to spin-spin T_2 relaxation times and discerned time-dependent mixing between T_2 populations. T_1 and T_2 relaxation times depend on the mediation of dipolar coupling by rotational motions; therefore these experiments indicate molecular rotational mobility. Temperature dependence of self-diffusivity and T_1-T_2 correlation measured within a rubbery as well as a glassy HPMCAS/acetone sample indicated that these measurements can determine the thermodynamic phase of polymer-solvent systems.

Progression of the SDD droplet drying model and the fundamental aspect of the research on polyelectrolyte and polymer dynamics expanded the current knowledge of polymer glass transition behavior, network formation, and aging. This research demonstrates the potential use of NMR to characterize and quantify mobility and mass transfer of polymers and other pharmaceutically-relevant materials.

NUCLEAR MAGNETIC RESONANCE THEORY

An Introduction to Nuclear Magnetization

Nuclear magnetization is caused by the nuclear spin imparting a magnetic moment on the nuclei [2]. In analogy to classical mechanics, the spin quantum number can be thought of as due to a delocalized electric charge spinning, and thus inducing a magnetic field vector. Whereas nuclei with multiple protons will have multiple spins interacting, a proton or a hydrogen nucleus will have a single spin. Outside of a magnetic field, the spins from hydrogens within a sample, for example those on water molecules, are oriented randomly, and the magnetic vectors sum to zero.

When a magnetic field is applied, the only possible quantum states predicted by the Schrodinger Equation via a spin interacting with its environment due to the Zeeman interaction are positive spin ½ and negative spin ½, corresponding to the spins being aligned parallel and anti-parallel with the magnetic field (B_0) [2]. The parallel state is slightly more stable than the anti-parallel state, with an energy difference of Planck's constant times the gyromagnetic ratio (specific to each atom) times the magnetic field strength; $\hbar\gamma B_0$. This stability difference makes the distribution of spins within the water sample slightly skewed towards the parallel state, giving the sample a net magnetization vector pointing parallel with the applied field.

In statistical mechanical terms, the most probable state of spins within the system is governed by the Boltzmann distribution [2]. There are two consequences of this. First, in a high-field NMR magnet, the parallel and anti-parallel energy difference is at least 5 orders of magnitude smaller than the Boltzmann energy, k_BT, thus the dynamics of the

sample is not disturbed by NMR experiments. Second, the ability to receive a signal from the net magnetization of the spins requires that there be a difference in the average number of spins in the parallel versus the anti-parallel state. The Boltzmann distribution shows that the difference skews more and more as the magnetic field increases, thus the larger the magnetic field, the more signal.

The Application of NMR and Spin Nutation

In a magnetic field, spins precess about the applied field at the Larmor Frequency which is equal to the gyromagnetic ratio of the nuclei multiplied by the magnetic field strength: $\omega_0 = \gamma B_0$ [2]. The Larmor frequency is in the radiofrequency (RF) range. In order to acquire signal from the sample, a resonant RF pulse applied by the RF coil which jackets the sample is used to tip the net magnetization vector out of equilibrium and away from the field direction. After this pulse, the spins precess in phase at the Larmor frequency about the B_0 field. The net magnetization from these spins is thus precessing, and induces electric current in the RF coil. Fig. 1.1 shows the net magnetization vector on a Cartesian grid before, during, and after an RF pulse.

In Figure 1.1, the net magnetization vector is initially aligned with the B_0field along the longitudinal (Z) axis. A pulse of radio frequency energy tipping the magnetization vector into the transverse plane is shown in the middle image. After the pulse, the transverse magnetization vector precesses about the longitudinal axis at the Larmor frequency.

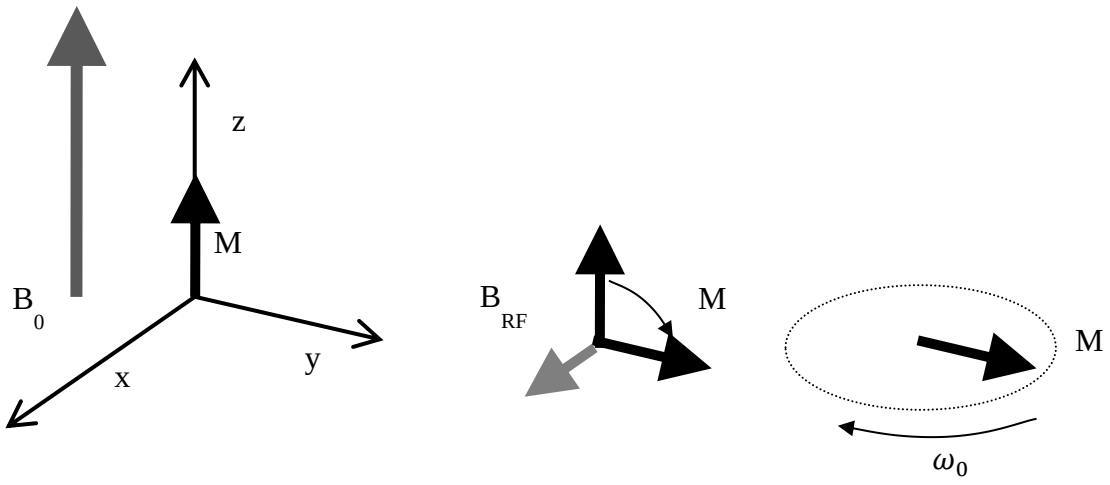

Figure 1.1. Nutation of the net magnetization vector during a 90° RF pulse.

The RF coil simultaneously measures the magnitude of signal in the x and y axes, referred to as the transverse plane. The signal measured in the x and y axis allow for the decomposition of the transverse magnetization vector into real and imaginary components. If the reference-frame of signal acquisition is slightly off resonance from the hydrogen spins' Larmor frequency, what is seen on the NMR spectrometer after the RF pulse is a sinusoidal exponential decay of the NMR signal. A generalized image of the x and y (real and imaginary) components of the magnetization vector is shown in Fig. 1.2.

The decay of the NMR signal is due to T_2^*, which includes all of the spin dephasing effects of T_2 or spin-spin relaxation, to be discussed later, as well as additional dephasing due to an inhomogeneous magnetic field over the sample volume. As a NMR parameter, T_2^* is the time constant for the exponential decay of the NMR signal with the form: $S = S_0 \exp\left(-\frac{t}{T_2^*}\right)$.

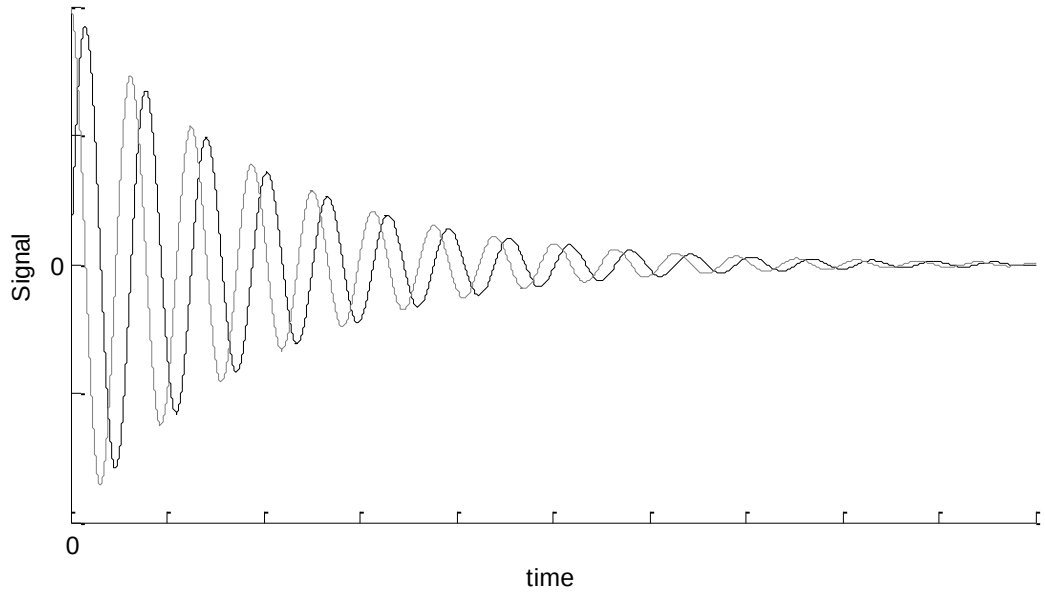

Figure 1.2. The real and imaginary components of a FID with the reference frequency off resonance from the single Larmor frequency.

As a quick note on spectroscopy, the acquired signal can be Fourier transformed to reveal the Larmor frequencies present within the sample. In liquid-state NMR, in the motional narrowing regime [3], frequency spectra are delta functions on the frequencies present convoluted with Lorentzians of widths inversely related to the T_2 of the components. Because a single frequency is present in the FID shown in Fig. 1.2, its Fourier transform would show a single Lorentzian with a peak shifted slightly from the reference frequency.

The Bloch Equations

The dephasing from effects which are constant during the NMR timescale such as magnetic field inhomogeneity can be refocused by the time reversing effect of the Hahn spin echo [4]. However, the irreversible relaxation mechanisms causing the transverse

magnetization to dephase away by spin-spin relaxation (T_2) and the longitudinal magnetization to come to equilibrium by spin-lattice relaxation (T_1) are ever present. The change in magnetization in the Cartesian directions is governed by the Bloch equations[5]:

$$\frac{dM_x}{dt} = \gamma M_y \left(B_0 - \frac{\omega_{ref}}{\gamma}\right) - \frac{M_x}{T_2}$$

$$\frac{dM_y}{dt} = \gamma B_{RF} - \gamma M_x \left(B_0 - \frac{\omega_{ref}}{\gamma}\right) - \frac{M_y}{T_2} \qquad (1.1)$$

$$\frac{dM_z}{dt} = \gamma M_y B_{RF} - \frac{M_z - M_0}{T_1}$$

The Bloch equations in the rotating frame combine the effects of nutation, precession, and relaxation into differential equations that are useful for understanding NMR phenomena. The RF pulse causes a magnetic field in the X-direction, and thus a precession through an angle of the magnetization, as seen in the middle image of Figure 1.1. The terms in x and y which include $B_0 - \frac{\omega_{ref}}{\gamma}$ account for the Larmor frequency spinning faster or slower than the reference frequency, and thus adding a sinusoidal behavior to the magnetization in the x and y Cartesian directions. This precession of the magnetization in the transverse plane is shown in the third image in Fig. 1.1. The sinusoidal change in magnitude of the x and y (real and imaginary) components are shown in Fig. 1.2. Spin-spin or T_2 relaxation is the dephasing of the spin vectors over time, resulting in a loss of phase coherence of the magnetization in the transverse plane. As seen in the Bloch equations, T_2 relaxation only affects the component of the magnetization that is in the transverse plane. Spin-lattice or T_1 relaxation is the spins

coming to equilibrium with the surrounding magnetic (B_0) field. In the Bloch equations, T_1 affects the magnetization in the Z direction. The solutions to the Bloch equations for relaxation of signal from arbitrary initial conditions are:

$$M_{xy}(t) = M_{xy}(0)exp\left(-\frac{t}{T_2}\right)$$

$$M_z(t) = M_0 + (M_z(0) - M_0)exp\left(-\frac{t}{T_1}\right) \quad (1.2)$$

Note that T_1 and T_2 are simply time constants in this phenomenological description of NMR relaxation. However, there is a molecular basis for relaxation.

Relaxation

NMR relaxation happens through the coupling of fields and a spontaneous emission without a spin interacting with other fields is improbable. The primary interactions which may cause changes in nuclear magnetization are internuclear and intranuclear dipolar interactions. A nuclei possessing spin must have a dipole, and it can couple with the surrounding dipole tensors to induce magnitude and direction changes in magnetization relative to the B_0 field.

One can imagine a hydrogen (proton) spin on a water molecule tumbling in space and experiencing directional dipolar interactions with neighboring nuclei on other molecules as well as its own molecule while precessing about the local magnetic field. In addition, one can imagine how these interactions will result in phase shifts (spin-spin relaxation) due to changing magnetic fields and thus Larmor frequency fluctuations, resulting in a loss of ensemble spin phase coherence. Stochastic fluctuations in the

Larmor frequency and a Langevin approach to its interpretation is the basis behind R. Kubo's stochastic theory on line shape and relaxation [3].

Unlike spin-spin relaxation, spin-lattice relaxation involves energy exchange between a spin and its surroundings (lattice) in quantized amounts equal to the energy difference between the parallel and anti-parallel state of the spin ($\hbar\omega_0$) and thus causing transitions between these states. These exchanges of radio frequency energy by dipolar interactions between spins and the lattice cause the sample magnetization to equilibrate with the B_0 field.

In a liquid system, isotropic and fast molecular motions cause the dipolar interactions to average to zero. Motional averaging thus leads to slow dephasing and a T_2 around a second. In application, this timescale gives the NMR experimenter sufficient time to manipulate the signal for the purposes of imaging or measurement of translational motion. In liquids the T_1 is equal to T_2 because the molecular frequencies of (rotational) motion present induce Larmor frequency fluctuations and spin-state transitions synonymously. If the spin system is embedded in an ordered lattice, these interactions sensitive to orientation cause spin phase coherence to quickly dephase in a microsecond or less. At the same time the net magnetization can require days (in the case of diamond) to equilibrate. Note that the transition from liquid to solid state, as will be seen later in this thesis, comes with diminishing ability to perform such experiments.

The short T_2 and long T_1 of a solid state system, the T_2 equal to T_1 in liquid systems and the divergence of T_1 from T_2 was shown by Bloembergen, Purcell and Pound and was explained with the rotational correlation model [6]. An equation for the T_1

relaxation rate can be found through time-dependent perturbation theory involving the transition of spins between two energy states. The most amenable form involves spectral density functions, $J^{(q)}(\omega)$, where ω is in itself a spectrum of the frequencies of translational, vibrational, and rotational motions inherent to the molecular ensemble. The T_2 relaxation rate can be found through density operator formalism in the rotating reference frame. In quantum mechanics, the density matrix provides the ensemble averaged expectation value for a given NMR measurement, bridging between quantum mechanics and polarization and coherence phenomena by statistical mechanics. The relaxation rate is a function of how the spectral density functions overlap with the frequencies which induce transitions. These transition frequencies include ω_0 and $2\omega_0$, and there is a zero frequency component for T_2 dephasing. For spin ½ nuclei, the equations for the T_1 and T_2 relaxation rates are[2]:

$$\frac{1}{T_1} = \left(\frac{\mu_0}{4\pi}\right)^2 \gamma^4 \hbar^2 \frac{9}{8}\left[J^{(1)}(\omega_0) + J^{(2)}(2\omega_0)\right]$$

$$\frac{1}{T_2} = \left(\frac{\mu_0}{4\pi}\right)^2 \gamma^4 \hbar^2 \frac{9}{8}\left[\frac{1}{4}J^{(0)}(0) + \frac{5}{2}J^{(1)}(\omega_0) + \frac{1}{4}J^{(2)}(2\omega_0)\right] \qquad (1.3)$$

where μ_0 is the magnetic moment.

The spectral density functions can be modeled for a system based on its molecular dynamics. One of physical significance to the fluctuations in dipole-dipole interactions that occur in liquids is the isotropic rotational diffusion model. Dipolar interactions arise by the rotations of the dipole vector coupling with the applied field and other spins. The correlation time, τ_c, is used as a measure of the rate of rotational diffusion, and can be

thought of as the time required for a molecule to forget its initial angular location and rotation rate. The spectral density functions are[2]:

$$J^{(0)}(\omega) = \frac{24}{15r_{ij}^6}\frac{\tau_c}{1+\omega^2\tau_c^2}$$

$$J^{(1)}(\omega) = \frac{4}{15r_{ij}^6}\frac{\tau_c}{1+\omega^2\tau_c^2} \qquad (1.4)$$

$$J^{(2)}(\omega) = \frac{16}{15r_{ij}^6}\frac{\tau_c}{1+\omega^2\tau_c^2}$$

The power of six on r_{ij}, which is the distance between coupling nuclei, shows that only the nearest neighbors matter.

A plot of T_1 and T_2 as a function of the correlation time using the relaxation rates of equation 3 with the spectral density equations (1.4) is shown in Fig. 1.3. A correlation time of 10 picoseconds predicts a T_1 and T_2 of roughly a second, similar to that of free water at room temperature. With increasing correlation time, for example through increasing viscosity or molecular size, the T_2 and T_1 decrease together. However, T_1 reaches a minimum when the correlation time is equal to the inverse of the field strength and begins to increase with increasing correlation time while T_2 continues to decrease. The minimum in T_1 is due to the $1+\omega^2\tau_c^2$ in the denominators of the spectral density functions of Equation (1.4). Short correlation times make the denominator small such that the linear term, τ_c, in the numerator dominates and long correlation times make the denominator large such that the quadratic term, $\omega^2\tau_c^2$, dominates. T_2 doesn't have the minimum because of the zero frequency spectral density component which allows τ_c to dominate at all frequencies. To reiterate this complex phenomena, energy is most

efficiently transferred between the spins and the lattice and the magnetization comes to equilibrium as quickly as possible when the spectrum of molecular motions includes a correlation frequency (τ_c^{-1}) equal to the Larmor frequency. Note that what was implied by the spectrum of molecular motions, and is not shown with the simplified rotational correlation model, is that molecular tumbling is not the only motion which allows coupling of fields. It would seem that restricted vibrations and rotations of individual spin bearing nuclei on a large molecule, as well as restricted motions such as those present in large molecular networks become the primary means of averaging frequency perturbations from dipolar interactions in molecules which are unable to tumble.

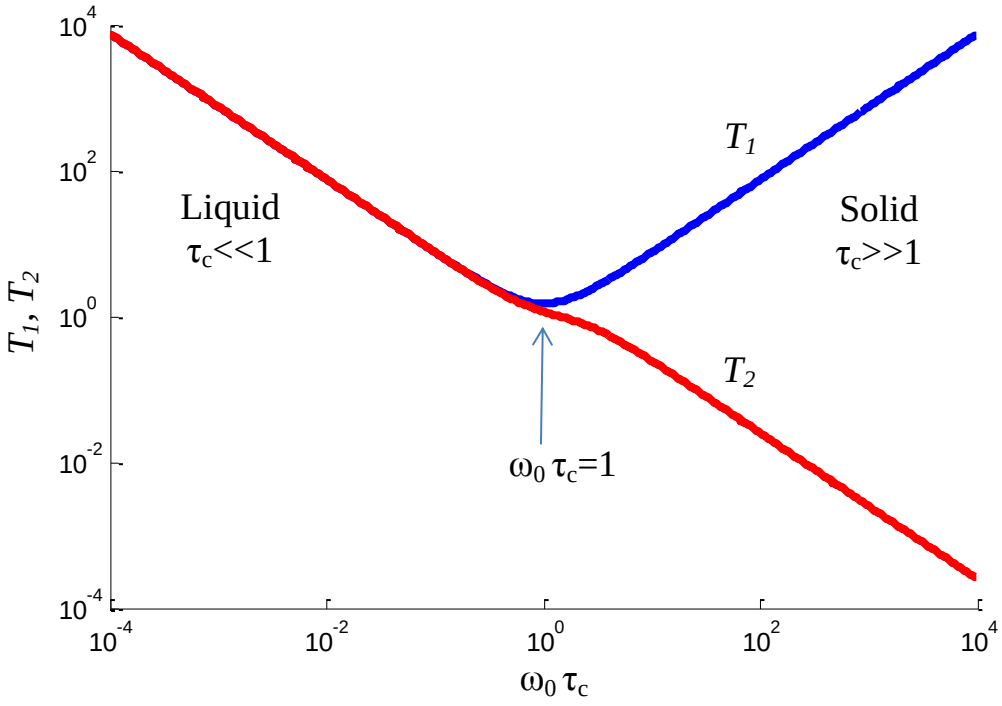

Figure 1.3. The T_1 and T_2 relaxation times predicted by the rotational correlation model as a function of the rotational correlation time τ_c using (1.3) and (1.4) [2, 6].

The correlation time has quantitative meaning when it arises from solving the rotational diffusion equation, a parabolic partial differential equation, for a rigid sphere of radius a using the method of separation of variables and seeking an exponential solution to the resulting time dependent ordinary differential equation. The correlation time is simply the negative inverse of that which multiplies by time in the exponential:

$$\tau_c = \frac{a^2}{D_s} = \frac{\pi \eta a^3}{k_B T} \tag{1.5}$$

where D_s is the spherical diffusivity and η is the viscosity [7, 8]. Equation (1.5) shows that the particle size, the surrounding molecular viscosity, and the temperature all directly affect the correlation time and thus the relaxation rates.

Basic Pulse Sequences to Measure Relaxation

There are two standard methods of measuring T_1 and T_2; the T_1 inversion recovery (T_1 IR) pulse sequence and the Carr-Purcell-Meiboom-Gill (CPMG) pulse sequence [9-11]. A pulse sequence is a timing sequence, visualizing when the spectrometer performs certain actions. These actions include those performed by the RF coil such as RF pulses and signal acquisition, and those performed by the gradient set.

The effect of an RF pulse, laid out in Fig. 1.1, is to coherently excite spins through an angle relative to the longitudinal axis; the effect of a 90° pulse was shown in Fig. 1.1. A Fourier relationship exists between the shape of the pulse in time and the shape of the pulse in the frequency domain. Hard pulses are short in the time-domain and excite all the Larmor frequencies within the sample. Soft pulses selectively excite a frequency bandwidth of the sample. A gradient in the magnetic field can be directionally applied

over the sample by the gradient set and will, among other purposes, play a pivotal role to phase encode for molecular displacements in pulsed gradient stimulated echo (PGSE) experiments.

The T_1 IR sequence, shown in Fig. 1.4, starts with a 180° pulse exciting the net magnetization to directly oppose the B_0 field. The sequence then has an inversion time, a time over which the sample is able to relax solely by T_1 due to all of the magnetization being present in z axis. When the 90° pulse is applied and signal acquisition occurs, the amount of signal observed is dependent on the amount of net magnetization which was present prior to the pulse. Typically when measuring T_1, the pulse sequence will run multiple times using logarithmically incremented inversion times and acquiring the FID associated with each inversion time. The first acquired (real and imaginary) points of every FID are extracted and the points are coherently phased to be entirely real. A regression of the inversion time versus the resulting real signal at each inversion time to Equation (1.2) can be performed to solve for T_1.

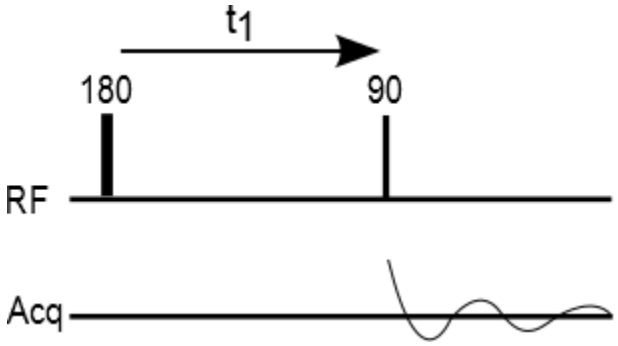

Figure 1.4. The T_1 IR pulse sequence

The CPMG sequence, shown in Fig. 1.5, starts with a 90° pulse to excite the net magnetization into the transverse plane. After the τ time, a 180° pulse reverses the sense

of precession, and at the time 2 τ the first echo is acquired. This is exactly the Hahn spin echo, which refocuses the dephasing effects from magnetic field inhomogeneity such that the echo is weighted by true T_2 as opposed to T_2^*. Many additional spin echoes (thousands) are trained back to back, spaced apart in time by 2τ and sandwiched between 180° pulses. T_2 can be found by extracting the maximum signal magnitude from each echo in the train, plotting versus time, and performing an exponential fit of the form seen in Equation (1.2).

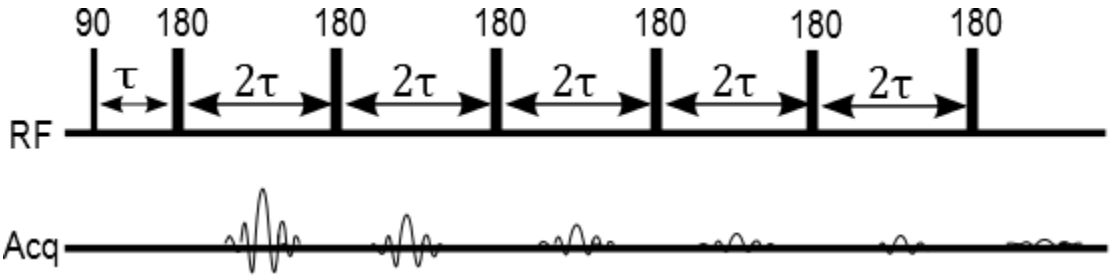

Figure 1.5. The CPMG pulse sequence for measurement of T_2 relaxation

ADVANCED TOPICS

Diffusion

Because pulsed gradient NMR measures the translational motion of ensembles of molecules, a complete understanding of stochastic motion is necessary. The way that a chemical engineer often looks at diffusion is mutual diffusion; the ability of a system to rid a concentration gradient. Fick's first law of binary diffusion is often cited (2.1):

$$J = -D_{AB}\frac{\partial C_A}{\partial x} \tag{2.1}$$

Fick's law states that the diffusive flux of component A, J, is equal to the mutual diffusion coefficient D_{AB} times the gradient in concentration of component A. The negative sign implies that the flux moves from high concentration to low concentration. Fick's law is phenomenological, but the diffusion coefficient having units of $\frac{m^2}{s}$ is well founded, as will be seen.

The idea of diffusion can also be applied to systems in equilibrium, and even systems of like molecules, as is well understood by the pulsed gradient NMR researcher, and this type of diffusion is called self-diffusion. Self-diffusion was explained by Albert Einstein in 1905 to understand Robert Brown's observation by microscope of the movement of pollen particles dispersed in water and thus called Brownian motion [12]. Einstein characterized self-diffusion of the Brownian particle as the balance between the thermal fluctuation of the system and the frictional drag on the particle. To get to his famous result, the approach of Paul Langevin will be used. The 1D Langevin equation (Eqn. 2) is a force balance on the Brownian particle.

$$m\ddot{x} = F(t) - F_d \tag{2.2}$$

By Newton's second law, the mass, m, times the acceleration of the particle, $\ddot{x}$, is equal to the random fluctuating force $F(t)$ that continually disturbs the particle minus the frictional drag force on the particle, F_d. The drag force on the spherical particle can be equated to Stokes' drag: $F_d = \zeta\dot{x}$ where $\dot{x}$ is the particle velocity and ζ equals $6\pi\mu R$. Equation two is a stochastic differential equation due to the fluctuating force, $F(t)$. Multiplying equation two by $x(t)$, rewriting the left side using integration by parts, and taking the ensemble average results in equation (2.3):

$$m\left[\frac{d}{dt}\langle x\dot{x}\rangle - \langle\dot{x}^2\rangle\right] = -\zeta\langle x\dot{x}\rangle + \langle xF(t)\rangle \tag{2.3}$$

The ensemble average is a necessary step in making the stochastic differential equation solvable. Realize, however, that the solution is now the average over many of the particle fluctuation, or of many independent identically distributed particles undergoing a fluctuation. In either case, fluctuations must happen on a time scale which is much smaller than the time scale of observation. The mean squared velocity times the particle mass, $m\langle\dot{x}^2\rangle$, in equation 3 must equal twice the equilibrium kinetic energy associated with the particle's translational motion in one dimension: k_BT by the equipartition of energy. The variables which make up the term $\langle xF(t)\rangle$ will be assumed uncorrelated, such that $\langle xF(t)\rangle = \langle x(t)\rangle\langle F(t)\rangle$; the fluctuations are not dependent on the particle location. Because the fluctuation force is completely random, the average of the vector sum of many fluctuations is zero. This requirement also leads to zero mean displacement; intuitively realized by the mean displacement of an ensemble of independent identically distributed particles undergoing a fluctuation being zero. (2.3) becomes:

$$m\frac{d}{dt}\langle x\dot{x}\rangle - k_B T = -\zeta\langle x\dot{x}\rangle \tag{2.4}$$

With the initial condition that $x(0) = 0$, the solution to Equation 4 is:

$$\langle X\dot{X}\rangle = \frac{k_B T}{\zeta}\left[1 - \exp\left(-\mathrm{t}/\mathrm{t}_\zeta\right)\right] \tag{2.5}$$

where $\mathrm{t}_\zeta = \frac{m}{\zeta}$ and $X(t)$ is the particle's displacement from its origin. Using integration by parts to re-write the left hand side of (2.5) as $\frac{1}{2}\frac{d}{dt}\langle X^2\rangle$ and then integrating from 0 to t results in:

$$\langle X^2\rangle = \frac{2k_B T}{\zeta}\left[\mathrm{t} - \mathrm{t}_\zeta\left(1 - \exp\left(-\mathrm{t}/\mathrm{t}_\zeta\right)\right)\right] \tag{2.6}$$

Equation (2.6) shows that the mean squared displacement displays separate behavior depending on the time over which the particle is observed. A system described by (2.5), known as an 'Ornstein-Uhlenbeck' process, has the property that behavior over longer and longer time scales exponentially asymptotes to the mean behavior. Equation (2.7) shows the short time limit and the long time limit, where the short time limit is analyzed by first re-writing the exponential in (2.6) using up to second order terms of its Taylor expansion.

$$\lim_{t\to 0}\langle X^2\rangle = \frac{k_B T}{m}\mathrm{t}^2 \tag{2.7}$$

$$\lim_{t\to \infty}\langle X^2\rangle = 2\frac{k_B T}{\zeta}\mathrm{t}$$

In the short time limit, the particle's mean displacement is ballistic; proportional to the time of observation. This leads to the mean squared displacement being proportional to time squared. In the long time limit, the particle's motion is stochastic and its mean

squared displacement is proportional to time. The time scale which separates the transition from ballistic to stochastic motion, t_ζ in (2.5), is the correlation time for velocity fluctuations. From the definition that $\mathrm{t}_\zeta = \frac{m}{\zeta} = \frac{m}{6\pi\mu R}$, the correlation time for water molecules is $1.6 * 10^{-13}$ seconds, and intuitively this is the time between molecular collisions. The correlation time for a 2 micron diameter colloidal particle in water is $6 * 10^{-8}$s, and this can be understood at the time scale over which the particle's inertia, carrying the particle in a ballistic manner, becomes sufficiently dampened by hydrodynamic interactions with the surrounding water such that it shows no memory of the initial velocity. Thus, the correlation time is intrinsically related to the velocity autocorrelation function. What Einstein realized, as can be seen by (2.7), was that the 'rate' of mean squared displacement of a Brownian particle, or the self-diffusion coefficient, is equal to the ratio of the thermal fluctuations, which disturb the particle, to the drag, which restores the particle towards equilibrium. Using the equation for Stoke's drag, this is the Stokes-Einstein-Sutherland equation for self-diffusivity:

$$D = \frac{k_B T}{\zeta} = \frac{k_B T}{6\pi\mu R} \tag{2.8}$$

Combining (2.8) with (2.7), one sees that in the diffusive regime, $\langle X^2 \rangle = 2Dt$, as in the Fick's law case, the diffusivity has units of $\frac{m^2}{s}$.

Characterizing Avogadro's number of particles undergoing stochastic motion lends itself to understanding through statistics. This was seen previously when taking the ensemble average of the force balance (2.2). What follows will show that the parabolic differential equation which governs the change in time and space of the humanly

identifiable and conserved quantities: mass, momentum, or heat, is physically grounded in diffusive or stochastic motion.

The conditional probability density in 1-D, $P(x_0|x,t)$, is the probability that a particle starting at x_0 is at x after a time t. What is even more useful to the PGSE NMR experimenter is the average propagator:

$$\bar{P}(X,t) = \int p(x_0)\, P(x_0|x_0 + X, t) dx_0 \tag{2.9}$$

The average propagator is the probability that a particle displaces by X over a time interval t[2] and is a summation of the conditional probability over all starting locations and all particles respectively. The probability density function, $p(x_0)$, is the probability of finding a particle at x_0 at the starting time, t_0. All of these functions have the property that the integral over the range of possible displacement is equal to 1: $\int_{-\infty}^{\infty} P(x)dx = 1$. Also, these functions can be acted on by differential equations such that they can be the dependent variable in the parabolic partial differential equation governing diffusion. For convenience of the imagination the conditional probability is used:

$$\frac{\partial}{\partial t} P(x_0|x_0 + X, t) = D \frac{\partial^2}{\partial x^2} P(x_0|x_0 + X, t) \tag{2.10}$$

Consider a system of an infinite medium of identical particles with equal average spacing. A particle within this medium can be chosen and (2.9) governs the evolution of the conditional probability function. Because the initial location of the particle is known, the initial condition is a delta function at x_0. The solution to this differential equation is:

$$P(x_0|x_0 + X, t) = \frac{1}{\sqrt{4\pi D t}} exp\left(\frac{-X^2}{4Dt}\right) \tag{2.11}$$

Comparing (2.9) to the normalized Gaussian function: $f(x) = \frac{1}{\sqrt{2\pi\sigma^2}} exp\left(\frac{-(x-\mu)^2}{2\sigma^2}\right)$, it is seen that the conditional probability function is a Gaussian with zero mean $(\mu = 0)$ and variance: $\sigma^2 = 2Dt$. Realizing that the variance is the second moment minus the first moment squared, which is the mean squared minus the squared mean, the familiar result of $\langle X^2 \rangle = 2Dt$ is found.

Fig. 2.1 shows (2.9) plotted at time intervals, revealing how the Gaussian curve gets shorter and broader with time. Of course, as time approaches infinity, so too does the variance of the Gaussian, such that total uncertainty of the particle location is approached.

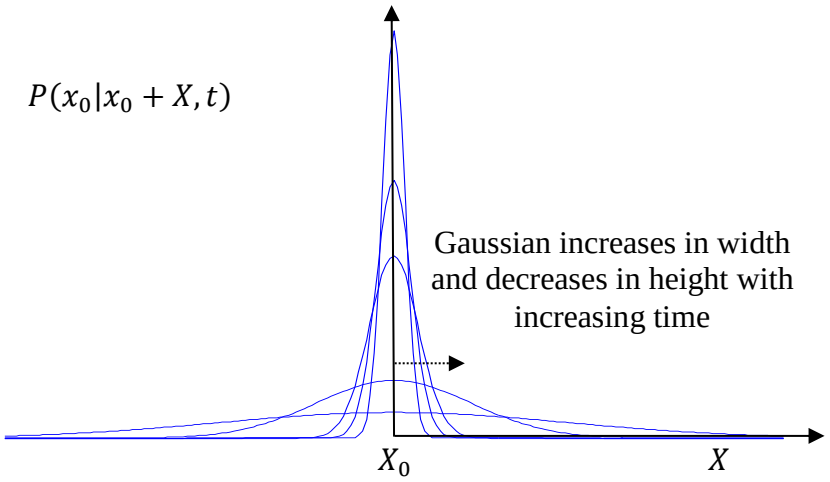

Figure 2.1. The evolution of the conditional probability of displacements of a particle undergoing stochastic motion in an infinite medium.

This analysis provides a physical understanding for what is too often looked at from the thermodynamic perspective; the reason that Fick's law (2.1), works is because

of the ever-present writhing thermal motions; the second law of thermodynamic is observed because of the ubiquity of stochastic processes.

Polymer Dynamics

A polymer is a molecule containing many covalently bonded base units called mers. The degree of polymerization or number of mers within a polymer can range from thousands to millions. Polymers are often, though not necessarily, linear chains, such that mers are bound end to end in a long strand. This thesis studies the polymer hydroxypropyl methylcellulose acetate succinate (HPMCAS) produced by Shin-Etsu. HPMCAS polymer has a cellulosic backbone with hydroxypropyl, methyl, acetate and succinate functional groups randomly substituted onto the cellulose, with three sites possible per cellulose mer. The polymer backbone as well as the possible functional groups is shown in Fig. 2.2.

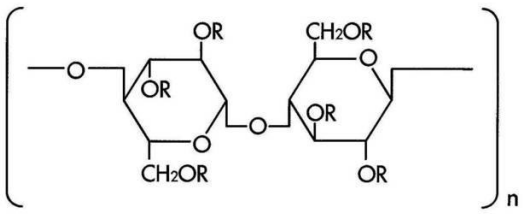

R = -H
-CH3
-CH2CH(CH3)OH
-COCH3
-COCH2CH2COOH
-CH2CH(CH3)OCOCH3
-CH2CH(CH3)OCOCH2CH2COOH

Figure 2.2. Hydroxypropyl methylcellulose acetate succinate (HPMCAS) molecular structure including the possible substituent groups[13].

Along with the type of polymer, solvent, and the degree of polymerization, polymer dynamics in solution is dependent on the concentration of polymer and the temperature. At the lowest weight percent, known as the dilute regime, polymer molecules interact primarily with the solvent and don't feel the surrounding polymer molecules. As polymer concentration is increased past the overlap concentration, C*, the pervaded volume of polymer gyrations overlap with that of other polymer molecules. Increasing the concentration past the entanglement concentration, C^e, results in sample-spanning entanglements. A polymer molecule is now required to take a tortuous path to move through the polymer matrix. Note that not all polymers entangle, due to the length of the polymer being too short to restrict the polymer to curvilinear diffusion. The regimes separated by the overlap concentration are displayed in Fig. 2.3 [14]. The polymers' dynamics within these regimes is unique and requires individual attention. Of particular interest within this thesis is polymer diffusion within each of these regimes.

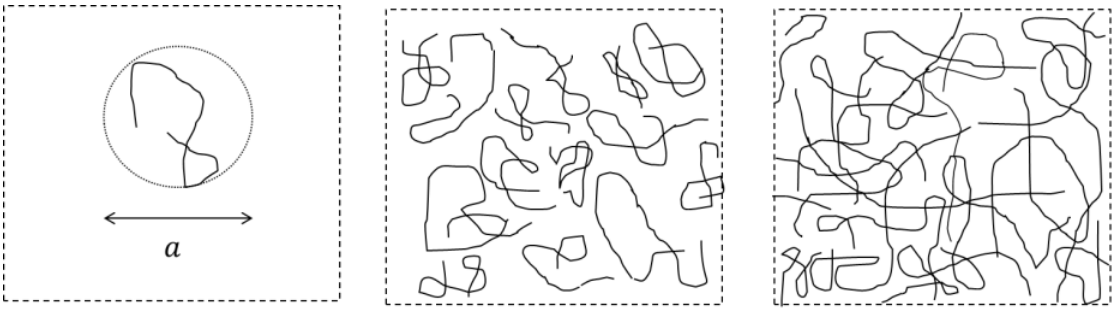

Figure 2.3. Pictorial representations of the three polymer regimes and the concentrations which define them.

Self-diffusion of polymer molecules within the dilute regime can be modeled by hydrodynamic considerations similar to the Stokes-Einstein-Sutherland equation, (2.8). This equation shows that the self-diffusion coefficient, which governs the rate of mean squared displacement of the molecule, is a ratio of the random thermal fluctuations caused by collision of solvent molecules, to the restoring force, caused by the drag on the particle as it moves through the fluid. This equation takes into account hydrodynamic interactions between the molecule and surrounding solvent molecules. These long range forces acting on the surrounding fluid due to the motion of the particle dominate during polymer diffusion in the dilute regime. Because the molecule and the solvent which moves with it are not spherical, the drag is not necessarily that of a sphere as in (2.8). Zimm found a form for the self-diffusion coefficient of the polymer where he solved for the drag on the polymer molecule as it pulls along solvent within its pervaded volume, effectively modeling the polymer as a solid that is the size of the pervaded volume[14, 15]:

$$D = \frac{8}{3\sqrt{6\pi^3}} \frac{k_B T}{\mu R} \tag{2.12}$$

The Zimm model for self-diffusion of a polymer molecule is valid not only for length scales longer than the hydraulic radius of the molecule, but also for sections of the molecule diffusing over distances smaller than the hydraulic radius. During this time, the polymer section doesn't yet realize that it is attached to the rest of the polymer molecule. As longer periods of time pass, the section feels the shackling effects of neighboring parts of the chain as it tries to diffuse longer distances. Neighboring parts are then included in the diffusive motion, increasing the size (radius) of the diffusing blob. This continues

until diffusive motion includes the entire chain. Simply put, diffusion of part of the polymer over a certain length scale smaller than the entire molecule involves diffusion of a part of the polymer and its pervaded volume with a size equal to that length scale. The time scale which separates the sub-diffusive motion of parts of the chain from diffusive motion of the entire chain is the Zimm time, $\tau_z \approx \frac{{R_h}^2}{D}$, where R_h is the hydraulic radius of the polymer molecule. Diffusive motion on longer time scales will involve the entire chain and mean squared displacement scales linearly with time. On smaller time scales, Zimm diffusion dictates that mean squared displacement scales with the size of the sections involved in diffusion on that time scale.

Adding the Zimm relaxation time for polymer modes, to take into account the growing length scale of the diffusing blob, it is possible to find a proportionality relationship for the mean squared displacement of a mer[14]:

$$\langle Z^2 \rangle \approx b^2 \left(\frac{t}{t_0}\right)^{2/3} \text{ for } t_0 < t < \tau_z \tag{2.13}$$

In (2.13), t_0 is the diffusive time scale of one Kuhn length, b. The Kuhn length is defined by the freely jointed chain, made up of units of length b, which is equivalent in mean squared radius and maximum end to end distance as the polymer molecule. Between t_0 and τ_z, (2.13) shows that the mean squared displacement scales with time to the power of 2/3, our first example of subdiffusion.

Zimm motion most readily applies in dilute solutions. As the concentration of polymer increases, the forces exerted by one polymer molecule on another hinder motion more than the drag of the solvent. Though dilute solutions are not studied in this thesis, this gives us an understanding of how polymer physicists imagine that polymers diffuse.

We see the re-occurrence of the Stokes-Einstein-Sutherland equation (2.8) in Zimm's equation for diffusivity (2.12), and simple relationships between measureable quantities and the polymer size make these intriguing models. In this research, the idea of blob diffusion, similar to the coupled polymer blobs which cause Zimm motion, is proposed to exist over many networked polymer molecules, though no proof of this has been seen.

Another simple model of polymer dynamics is called Rouse motion [16], which applies to melts of polymer, too short to entangle, without any solvent. Rouse motion is more applicable in these systems than Zimm motion because hydrodynamic interactions, as well as excluded volume interactions, are screened in melts. Rouse motion models the polymer molecule as a chain of beads attached together by springs, creating a coupled harmonic oscillator. The thermal energy which randomly moves a bead is dampened by the spring on either side and imparts energy onto the neighboring beads. The length scale of a bead is given the Kuhn length. As in Zimm motion, relaxation modes involve coherent motion of a number of beads. The relaxation time for the pth mode has the form[14]:

$$\tau_p \approx \tau_0 \left(\frac{N}{p}\right)^2 \text{ for } p = 1,2,\dots,N. \tag{2.14}$$

From this equation, the analogy to the modes of a guitar string can be seen; p=1 is the longest relaxation mode, involving the entire molecule, p=2 is the second longest and involves half the molecule, and this continues to the shortest mode, $p = N$, which involves a single bead.

The Rouse model is often useful in understanding viscoelastic behavior, but the relevant aspect to us is the subdiffusive motion which the Rouse model predicts. On time

scales shorter than the Rouse time, $\tau_R = \tau_{p=1}$, and longer than the shortest relaxation time, t_0, the mean squared displacement of a monomer scales with the mean squared size of the relaxing section of beads involved in the motion. Putting this in terms of the relaxation times results in the following form:

$$\langle Z^2 \rangle \approx b^2 \left(\frac{t}{t_0}\right)^{1/2} \text{ for } t_0 < t < \tau_R \tag{2.15}$$

Equation (2.15) shows that under Rouse motion, the mean squared displacement scales to the power of ½. Over observation times, $t < \tau_R$, the number of beads coherently participating in Rouse motion increases with this same ½ power, and the form for the self-diffusion coefficient of a mer on a polymer undergoing rouse motion is:

$$D \approx \frac{k_B T}{\zeta} \left(\frac{t}{t_0}\right)^{1/2} \text{ for } t_0 < t < \tau_R \tag{2.16}$$

This equation is similar to, and indeed it was obtained using, the Stokes-Einstein-Sutherland equation (2.8).

In this chapter, we have discussed many pertinent pieces of the scientific development of polymer dynamics; the Rouse and Zimm models were discovered in the 1950s [15, 16], but both required the contributions of P. Langevin, A. Einstein, and E. Sutherland 50 years prior. One additional key contribution to the current understanding of polymer dynamics was the reptation model of entangled polymer molecule proposed by P.G. De Gennes in 1971 [17].

Polymer Reptation is the forward and backward snake-like motion that a long polymer molecule must take to diffuse independently through the polymer matrix which topologically constrains it to a tube. Parts of the polymer exhibit curvilinear diffusion by

rouse motion within and along the confining tube. There are 4 important time-scales which separate different observed sub-diffusive motion of the entangled strand. These are, in order of length, the shortest relaxation time, τ_0, the relaxation time of the entanglement strand, τ_e, the rouse time, τ_R, and the reptation time, τ_{rep}. These are diffusive time-scales of key length scales of the entangled polymer. The τ_e is the time necessary for the polymer to feel the walls of its confining tube, and the τ_{rep} is the time necessary for the polymer to diffuse out of its original confining tube. On time-scales between τ_0 and τ_e, a mer of the molecule doesn't yet know that it is confined to a tube and still exhibits Rouse motion. Between τ_e and τ_R, parts of the polymer move by Rouse motion along the tube length, and because the curve of the tube confines the spatial directions of motion, the mean-squared displacement shows a unique $t^{1/4}$ scaling. At times longer than τ_R, each monomer diffuses coherently and snakelike along the tube, and because of the restriction of the diffusion to the contour of the tube, the mean squared displacement scales with $t^{1/2}$. Once the polymer breaks free of its initial confining tube, at $t = \tau_{rep}$, diffusive motion is again observed. These timescales are summarized in (2.17).

$$\begin{aligned} \langle Z^2 \rangle &\sim t^{1/2} \text{ for } t_0 < t < \tau_e \\ \langle Z^2 \rangle &\sim t^{1/4} \text{ for } \tau_e < t < \tau_R \\ \langle Z^2 \rangle &\sim t^{1/2} \text{ for } \tau_R < t < \tau_{rep} \\ \langle Z^2 \rangle &\sim t^{1} \text{ for } \tau_{rep} < t \end{aligned} \tag{2.17}$$

Studying semidilute mixtures of long linear polymer chains, Callaghan's NMR group saw all three subdiffusive regimes during observation times which the polymers were confined to their tubes through the subdiffusive scaling of mean squared

displacement with time, including the $t^{1/4}$ fingerprint of reptation [18, 19]. On time scales longer than the polymer is confined to a single tube length, Callaghan saw the mean squared displacement of the polymer again vary linearly with time.

Free-Volume Theory

Self-diffusion can be connected to mutual diffusivity through the free-volume theory of Vrentas and Duda [20, 21]. The free-volume theory is based on the total volume in liquid systems being made up of the pervaded volume or the hard core volume of molecules, and free volume. A certain portion of the free-volume is too near the surrounding molecules and would require too much energy for a molecule to occupy. Subtracting this interstitial free-volume from the total free-volume, what is left is the hole free-volume[22]. The basic idea behind the free-volume theory is that the self-diffusivity of a molecular species is equal to the probability that a hole of free-volume sufficiently large to fit a molecule forms next to the molecule multiplied by the probability that the molecule has sufficient energy to jump to the hole. For a 2-component system of solvent (component 1) and polymer (component 2), the solvent self-diffusivity, D_1, can be described in terms of free-volume parameters by:

$$D_1 = D_{01} exp\left(\frac{-\left(\omega_1 \hat{V}_1^* + \omega_2 \xi \hat{V}_2^*\right)}{\hat{V}_{FH}/\gamma}\right) \tag{2.18}$$

where ω_1 and ω_2 are the mass fractions of solvent and polymer and $\hat{V}_1^*$ and $\hat{V}_2^*$ are the specific volume of the hole needed for a jump by the solvent and polymer respectively. Similar to the shortest mode in the Rouse model of polymer dynamics, $\hat{V}_2^*$ is some

portion of the polymer molecule which moves coherently. The pre-exponential factor, D_{01}, is a temperature dependent parameter related to the energy required for a molecule to break free from its confining hole. The overlap factor, γ, accounts for the overlap in free volume shared by adjoining molecules, $\hat{V}_{FH}$, is the specific hole free-volume, and ξ is the ratio between the critical hole volume necessary for a solvent jump to that of a polymer jump. The ratio of $\hat{V}_{FH}$ to γ is:

$$\frac{\hat{V}_{FH}}{\gamma} = \frac{K_{11}}{\gamma}\omega_1\left(K_{21} - T_{g1} - T\right) + \frac{K_{12}}{\gamma}\omega_2\left(K_{22} - T_{g2} - T\right) \tag{2.19}$$

where K_{11} and K_{21} are free-volume parameters of the solvent and K_{12} and K_{22} are free-volume parameters of the polymer and T_{g1} and T_{g2} are the pure component glass transition temperatures of the solvent and polymer[21]. The polymer and solvent free volume parameters, K_{11}, K_{21}, K_{12}, and K_{22}within (2.19) show the same form as the empirical Williams-Landel-Ferry (WLF) parameters within the WLF equation, used in the method of reduced variables to construct polymer system master curves of rheological quantities, such as the complex dynamic modulus[23]. Equation (2.19) is a summation of the specific hole free-volume added to the system by the polymer and the solvent and assumes that the pure components have the same specific hole free-volumes as the components in mixture. The forms of (2.18) and (2.19) allow for combining parameters in data fitting by nonlinear regression [24]. The temperature dependence of D_{01} is:

$$D_{01} = D_0 exp\left(-\frac{E}{RT}\right) \tag{2.20}$$

creating a new pre-exponential factor, D_0, and an activation energy parameter. From the Arrhenius form of (2.20), it is clear from that D_{01} is the probability that the molecular component has sufficient thermal energy to break free of its current potential well formed by neighboring molecules.

If all of the parameters in (2.18), (2.19), and (2.20) can be found, then the solvent self-diffusivity can be predicted over a range of temperatures and concentrations. The next step is to relate the self-diffusivity to the mutual diffusivity, however there is no theory that can do this without unsubstantiated relationships or simplifications [20]. The one exception is that in the limit of a component concentration approaching zero the self-diffusivity of that component becomes equal to the mutual diffusivity.

Both self and mutual diffusion can be related to friction coefficients, similar to the drag coefficient in the Stokes-Einstein-Sutherland equation, except that the frictional interactions are split up into those between like molecules (ζ_{11} and ζ_{22}) and those between unlike molecules (ζ_{12}) [25]. Self-diffusion involves all three friction coefficients, whereas mutual diffusion involves only the friction coefficient for interactions between unlike molecules, preventing a closed form relation between the two. One simplification in free-volume theory literature is use of the fact that the solvent self-diffusivity is much larger than the polymer self-diffusivity, which allows for the closed form relation seen in (2.21). A consequence of this simplification is that by basing the mutual diffusivity on only the solvent self-diffusivity, the predicted mutual diffusivity will diverge from the actual diffusivity at low solvent weight fractions and become

meaningless at infinite dilution of polymer ($\omega_2 \to 0$) where the mutual diffusivity is equal to the polymer self-diffusivity[20].

$$D = \frac{D_1 \omega_1 \omega_2}{RT}\left(\frac{\partial \mu_1}{\partial \omega_1}\right)_{T,P} \tag{2.21}$$

The solvent chemical potential, μ_1, directly related to the thermodynamic activity of the solvent, a_1, can be calculated with use of the Flory-Huggins model[26]:

$$\mu_1 - \mu_1^0 = RT \ln a_1 \; = RT\left[\ln \varphi_1 + \left(1 - \frac{1}{r}\right)\varphi_2 + \chi {\varphi_2}^2\right] \tag{2.22}$$

where μ_1^0 is the arbitrary reference condition chemical potential, $\varphi_1 = 1 - \varphi_2$ is the solvent volume fraction, r is the number of mers in the polymer molecule and is large enough to ignore its reciprocal, and $\chi = fn(\omega_1)$ is the Flory-Huggins interaction parameter, added to capture unequal component interaction energies, which can be fit using solubility data. Combining equations (2.19) through (2.22) into a single equation, acting the derivative on (2.22), and absorbing $\left(\frac{\omega_1 \omega_2}{RT}\right)$ into D_0 results in [22]:

$$D = D_0 exp\left(-\frac{E}{RT}\right) exp\left(\frac{-\left(\omega_1 \hat{V}_1^* + \omega_2 \xi \hat{V}_2^*\right)}{\frac{K_{11}}{\gamma}\omega_1\left(K_{21} - T_{g1} - T\right) + \frac{K_{12}}{\gamma}\omega_2\left(K_{22} - T_{g2} - T\right)}\right) \tag{2.23}$$

$$(1 - \varphi_1)^2 (1 - 2\chi\varphi_1)$$

The usefulness of the free volume theory has been to predict the mutual diffusivity based on tabulated or otherwise experimentally obtainable pure component properties [27, 28].

Glass Transition

The rubber to glass transition of a fluid is the critical slowing down of the molecular scale dynamics within a fluid as the system is cooled from above to below the glass transition temperature ($T_{g)}$. The glass transition is a second order thermodynamic transition and is identifiable through a discontinuity in the [29, 30]. The temperature dependence of measurable kinetic quantities, such as viscosity and self-diffusivity, change continuously and smoothly over the glass transition, and additionally, locating T_g through the discontinuity in the thermal expansion coefficient is dependent on the measurement timescale, and thus the value of T_g is somewhat ambiguous[31].

Viscosity measurements of glass forming systems have shown Arrhenius, or an exponential relation to the inverse temperature, as well as super-Arrhenius, or an upward curvature to the inverse temperature dependence [32]. Arrhenius glass formers are said to be strong glasses, whereas super-Arrhenius glass formers are fragile [33]. Recent research has identified a general fragile to strong crossover among glass forming liquids which occurs at the dynamic crossover temperature T_X [32]. The onset of dynamic arrest or jamming at temperatures below T_X is due to the limited amount of free-volume within the system preventing molecules from displacing, similar to the occurrence of a traffic jam when the average distance between cars on a road becomes too short [34]. Researchers have suggested that T_X, which occurs at higher temperatures than the glass transition, is as important as T_g in understanding transport properties of glass-forming liquids, however this research will focus on the measurable changes between the rubbery ($T > T_g$) to glassy ($T < T_g$) state of HPMCAS/acetone systems [31, 32].

The size of a free-volume hole necessary for a displacement is equal to the size of the molecule for small molecules such as acetone [35]. For polymer molecules, the size is the minimum portion of the molecule which moves coherently to make a displacement step, similar in definition to the bead size of the Rouse model. The free-volume within the system is shared; used by all components for displacements. Solvent and polymer jumping units are not necessarily equal in size, and this leads to glass transitions for each diffusing component, though the lowest glass transition temperature, that of the smallest component, is typically the reported value [23].

In this research, the glass transition temperature of HPMCAS/acetone mixtures is estimated using the Fox equation [36]:

$$\frac{1}{T_g} = \frac{\omega_1}{T_{g1}} + \frac{\omega_2}{T_{g2}} \tag{2.24}$$

This phenomenological equation, based on the pure component glass transition temperatures, T_{g1} and T_{g2}, is seen to fit the T_g of diluent and polymer as well as copolymer systems. Model and experiments by Fox have shown that T_g increases and, at temperatures above 0 K, free-volume decreases with increasing polymer molecular weight [37, 38]. For the polystyrene polymer melts on which Fox researched, it was hypothesized that a decrease in molecular weight led to a substitution of covalent bonds for van der Waals bonds. The increase in concentration of van der Waals bonds resulted in an increase in free-volume due to the weak nature of and longer distance between these bonds.

One simple measure of the degree of system glassines is the ratio of the glass transition temperature to the system temperature: $\frac{T_g}{T}$ [39]. Because glassiness relates to molecular mobility, this ratio is used in the pharmaceutical industry for comparisons of relative system mobility [40].

Magnetic Resonance Imaging

Nuclear magnetic resonance imaging (MRI) involves the use of magnetic field gradients to spatially encode for position within the sample via the phase shift of spin isochromats. Image contrast can be obtained via differences in spin density, T_1, T_2, or diffusion rates. The elegant relationship between phase and position is due to a Fourier transform relationship between the normalized NMR signal, S_N, and the normalized spin density, ρ.

$$S_N(\boldsymbol{k}) = \int \rho\,(\boldsymbol{r}) \exp(i\boldsymbol{k}\cdot\boldsymbol{r})\, d\boldsymbol{r} \;\overset{\boldsymbol{FT}}{\leftrightarrow}\; \rho(\boldsymbol{r}) = (2\pi)^{-1} \int S_N\,(\boldsymbol{k})\, exp(i\boldsymbol{k}\cdot\boldsymbol{r})\, d\boldsymbol{k} \quad (2.25)$$

In (2.25), $\boldsymbol{k} = \gamma\delta\boldsymbol{G}$, with units of radians per meter, is a reciprocal space vector. Equation (2.25) shows that by designing NMR pulse sequences which probe *k* –space, one can image spin density as a function of position, $\boldsymbol{r}$, within the sample. In order to create an NMR image, one must sample a grid of discrete points in *k*-space. Due to the Fourier relation (2.25), the image resolution or pixel size, Δl, in real space is determined by the reciprocal of the maximum *k*-space value that is sampled; $\Delta l = \frac{\pi}{k_{max}}$. In addition, the image field of view (FOV) is dictated by the inverse of the difference between *k*-

space points; FOV $= \frac{2\pi}{\Delta k} = \frac{2\pi N}{k_{max}}$ where N is the number of points acquired in the *k*-space direction.

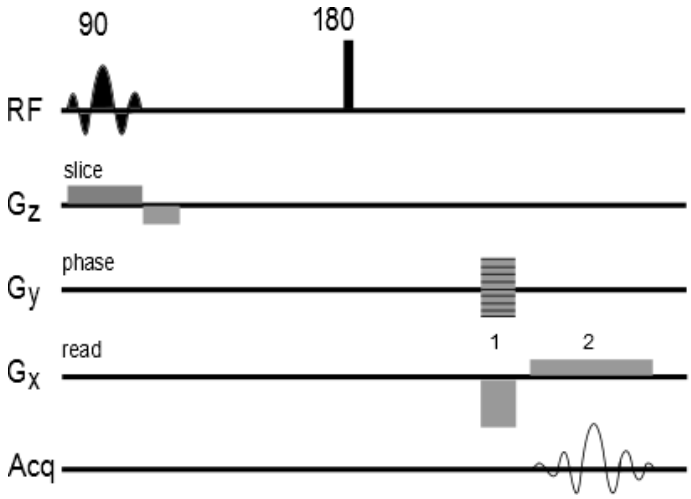

Figure 2.4. Basic 2D MRI imaging pulse sequence

A basic two-dimensional imaging sequence is shown in Figure 2.4. The gradient directions correspond to the read, phase, and slice directions. The 90° selective excitation pulse during the z-gradient selectively allows spins only from a certain slice in the sample to continue through the pulse sequence. If the sample is oriented along the z-direction, as is the case with the Bruker 250 MHz and 300 MHz magnets, then this pulse sequence will take an axial image. There is a gradient in Larmor frequencies within the sample during the applied z gradient. The soft sinc 90° pulse applied in the time domain is a rectangular pulse in the frequency domain and is only felt by spins with Larmor frequencies within a certain frequency range, and thus a slice normal to the z direction is selected. A schematic showing the progression through *k*-space is shown in Fig. 2.5. The dephasing caused by the first combined negative x and y gradient lobes, labeled 1 in Fig. 2.4, leads to spins which are at the point $(-k_{max\,x}, -k_{\max\,y})$ to be in phase with the

receiver. This path through *k*-space is shown by the line labeled 1 in Fig. 2.4. The read gradient, with the application time centered on the spin echo, is labeled 2 on Fig. 2.4. This gradient causes a path through *k*-space from $(-k_{max\,x}, -k_{\max\,y})$ to $(+k_{max\,x}, -k_{\max\,y})$. While the read gradient is applied, the real and imaginary signal is acquired at increments spaced by the dwell time. The acquisition time divided by the dwell time equals the number of acquired points on the traverse of *k*-space.

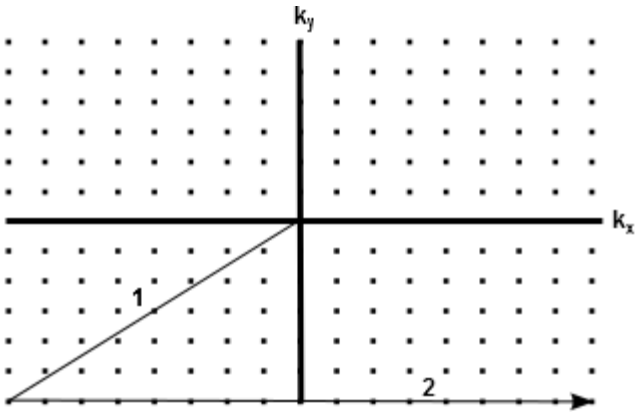

Figure 2.5. The path through k-space of the basic 2D NMR imaging sequence (Fig. 2.4).

By cycling through evenly spaced gradient values in the y-direction, all of the *k*-space points in Fig. 2.5 can be acquired, leading to a two-dimensional data set which contains a map of signal magnitude and phase at each point in *k*-space. Fourier transforming this data set in the $\boldsymbol{k}_x$ and $\boldsymbol{k}_y$ direction results in a spin density image. This image will be T_2 weighted by the echo time, T_1 weighted by the repetition time, and diffusion weighted by the pixel resolution [41]. One common practice is to add additional echoes to the sequence in Figure 1, making sure to get to the origin of *k*-space after signal is acquired and before the next 180, and traversing the same line of *k*-space at each signal

echo. By fitting a single T_2 relaxation rate to the exponential signal decay at each pixel, a T_2 image can be made. This pulse sequence, known as the multi-spin multi-echo (MSME) sequence, adds no additional time to the basic imaging sequence and can still be used to make spin density images.

Pulsed Gradient Spin Echo NMR

A pair of equal and opposite effective gradient pulses to dephase and refocus signal separated by an observation time allows for sensitivity to displacements of spins during that time. Spins which are excited into the transverse plane and precessing at the Larmor frequency will have their local Larmor frequency changed under the influence of a gradient in the magnetic field due to the relation $\omega_0 = \gamma(\boldsymbol{B}_0 + \boldsymbol{B}(Z))$. A gradient over the sample pulsed for a time δ thus results in the spins' phase being shifted by some angle depending on their location. Relative to no gradient this phase shift is simply $\phi(Z,t) = t \times \boldsymbol{B}(Z)$. As shown in Fig. 2.6, the gradient pulse winds up a helix of phase shifts into the spins within the sample along its application direction. A single gradient pulse encodes for position and, in the pulsed gradient spin echo experiment, an additional gradient pulse encodes for displacement. The tighter the helix, from either larger applied gradient or longer gradient pulse duration, leads to more sensitivity to displacement.

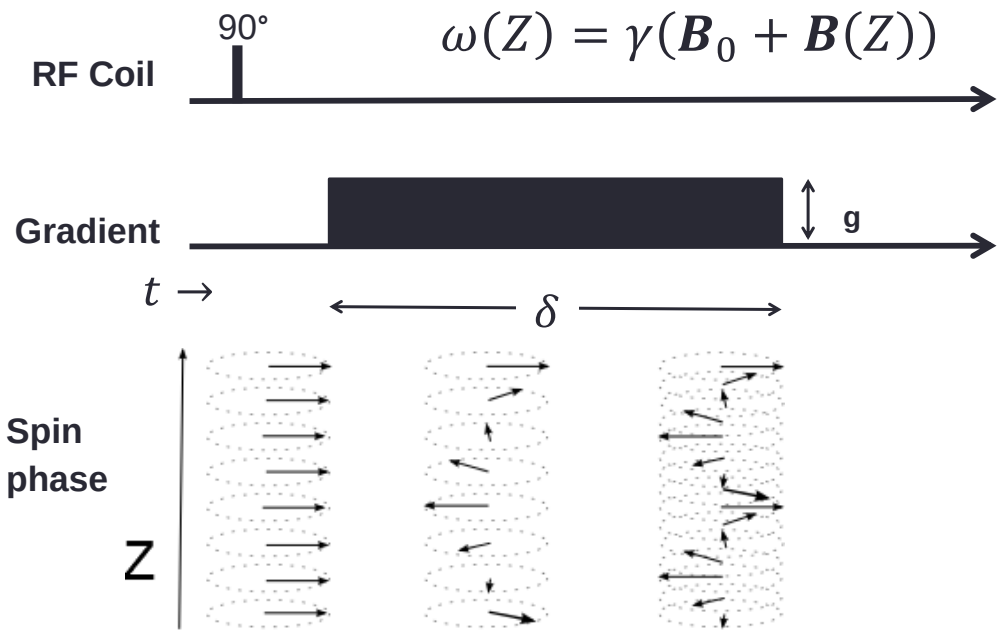

Figure 2.6. The effect of a gradient pulse on the relative phase of spins. The gradient pulse winds up a phase helix due to the location dependent Larmor frequency.

There are many combinations of gradients which are possible. The only requirement is that the zeroth moment of the gradients be equal to zero when signal is acquired, such that a gradient echo and a spin echo are formed at the same time. The requirement that the zeroth moment of the gradients be equal to zero is shown in (2.26).

$$\int_0^t \boldsymbol{g}^*(t')dt' = 0 \tag{2.26}$$

Higher order gradient moments become important in understanding how displacing spins will experience a phase shift under the influence of a gradient. The phase shift of a nuclear spin at time t, $\phi_j(t)$, which moves along a path $\boldsymbol{r_j}(t')$ in an effective gradient $\boldsymbol{g}^*(t')$ is:

$$\phi_j(t) = \gamma \int_0^t \boldsymbol{g}^*(t') \cdot \boldsymbol{r_j}(t')dt' \tag{2.27}$$

The effective gradient, $\boldsymbol{g}^*$, used in (2.26) and (2.27) takes into account the effect of RF pulses on the spin precession phase shift. The component of the magnetization in the longitudinal axis, which has no precession, is free from dephasing caused by magnetic gradients. Thus, any gradient applied when the magnetization is stored in the longitudinal axis is effectively zero. This is the case of spoiler gradients which are used in pulsed gradient stimulated echo experiments to dephase any left-over precession while the desired magnetization is stored in the longitudinal axis. Also, when a 180° RF pulse is applied, the phase shifts from the previous applied gradients are reversed. Thus, any gradient applied before a 180° RF pulse is effectively opposite its original sign.

The normalized echo amplitude, $E(t)$, allows for a simplified way to understand the signal echo amplitude and phase change due only to the applied gradients and not to other relaxation effects:

$$E(t) = \frac{M_+(t)_{\boldsymbol{g}^*(t')\neq 0}}{M_+(t)_{\boldsymbol{g}^*(t')=0}} \tag{2.28}$$

In (2.28), $M_+ = M_x + iM_y$ is the component of spin magnetization which can contribute to the NMR signal. It is useful to think about how individual spins will contribute to the normalized echo signal. The component of the normalized echo signal from spin j is:

$$E_j(t) = \exp\left(i\gamma \int_0^t \boldsymbol{g}^*(t') \cdot \boldsymbol{r_j}(t')dt'\right) = \exp\big(i\gamma\phi_j(t)\big) \tag{2.29}$$

Euler's formula, $e^{ix} = \cos(x) + i\sin(x)$, makes it apparent that the phase shift truly is a shift in the phase of precession of the spin and that phase shifts which are multiples of 2π

radians will still be exactly in phase with spins which have experienced no phase shift. Of course, it is the ensemble average of the phase shifted signals which create the echo amplitude in (2.28). However, (2.29) can easily relate to (2.28) in the case of coherent motion where all spins follow the same path relative to their starting position and therefore experience the same phase offset from the applied gradient.

In this case of coherent motion, the path of the ensemble of spins can be approximated by a Taylor series expansion about t=0:

$$\boldsymbol{r}(t') = r_0 + \boldsymbol{v_0}t' + \frac{1}{2}\boldsymbol{a}_0 t'^2 + H.O.T. \tag{2.30}$$

By inserting (2.30) into (2.29), the normalized signal amplitude can be related to the moments of the gradient, where the gradient moment of order n is:

$$M_n = \int_0^t t'^n \boldsymbol{g}^*(t')dt' \tag{2.31}$$

By nulling certain gradient moments with the design of the effective gradient sequence, pulse sequences become sensitive to certain order derivatives of the motion [42]. As stated in (2.26), pulse gradient sequences in general all null the zeroth moment, such that they are not sensitive to initial locations of the spin isochromats. A single PGSE nulls only the zeroth gradient moment, making the pulse sequence sensitive to coherent velocity and acceleration. A double PGSE nulls the zeroth and first gradient moments, making it insensitive to velocity and is therefore very useful in discerning incoherent motion such as dispersion when there is also coherent velocity.

Understanding the effect of incoherent motion within gradients on the normalized echo signal is easiest when starting from the Bloch-Torrey equation for diffusion and flow[43]:

$$\frac{\partial M_+}{\partial t} = -i\gamma \boldsymbol{r} \cdot \boldsymbol{g}^*(t) M_+ - \frac{M_+}{T_2} + D\boldsymbol{\nabla}^2 M_+ - (\boldsymbol{v} \cdot \boldsymbol{\nabla}) M_+ \tag{2.32}$$

Equation (2.32) is essentially a differential magnetization balance, adding advection and diffusion of the magnetization to the Bloch equation which accounts for signal relaxation by T_2. This differential equation can be solved for any general pulse gradient sequence, and for such a sequence which satisfies the gradient echo condition, (2.26), the normalized echo signal is:

$$E(t) = \exp\left[-D\gamma^2 \int_0^t \left(\int_0^{t'} \boldsymbol{g}^*(t'')dt''\right)^2 dt'\right] \exp\left[i\gamma \boldsymbol{v} \cdot \int_0^t \int_0^{t'} \boldsymbol{g}^*(t'')dt''\, dt'\right] \tag{2.33}$$

The gradient integrals in (2.33) can be solved specifically for certain pulse sequences, such that the found echo signal can be related to bulk velocity and effective dispersion of spins within the sample. The diffusive (dispersive) component contained within the first exponent will always be negative to satisfy the second law of thermodynamics and therefore leads to echo attenuation with increasing gradient strength. The coherent bulk flow component of the second exponent shows an imaginary number in the exponent which will oscillate the phase of the echo with increasing gradient strength. Because the acquired echo contains both real and imaginary components, the phase offset of the

normalized echo can be used to find bulk flow, $\boldsymbol{v}$, and the normalized echo attenuation can be used to find the effective dispersion coefficient.

In this thesis, the pulsed gradient stimulated echo experiment, shown in Fig. 2.7, is used to find effective self-diffusion coefficients. This pulse sequence starts with a 90° RF pulse which turns the spins into the transverse plane, and the spins begin to precess at their Larmor frequency. The dephasing gradient pulse winds a helical phase shift in the spin isochromats along the direction of the applied gradient. This magnetic gradient pulse is applied for a duration δ with magnitude g in the direction that displacements are to be measured. Another 90° RF pulse stores the magnetization in the transverse plane, saving the magnetization from T_2 decay. A spoiler gradient is applied, while the magnetization is in the transverse plane, to dephase any remaining signal. The importance of this is so that the third 90° pulse affects all spin isochromats in the same way, turning them again into the transverse plane. This third 90° pulse reverses the direction of precession of the spin isochromats from their original precession, making the first gradient pulse effectively negative. The rewind gradient pulse is applied after a time Δ from the start of the dephasing gradient pulse. The rewind gradient pulse, equal in magnitude and duration to the dephasing gradient pulse, satisfies the gradient echo condition seen in (2.26), refocussing the phase of spin isochromats which observed no net displacement over the observation time Δ. Signal is acquired at the spin echo. Because the entire echo is acquired, the echo contains information on the spectral frequencies within the sample.

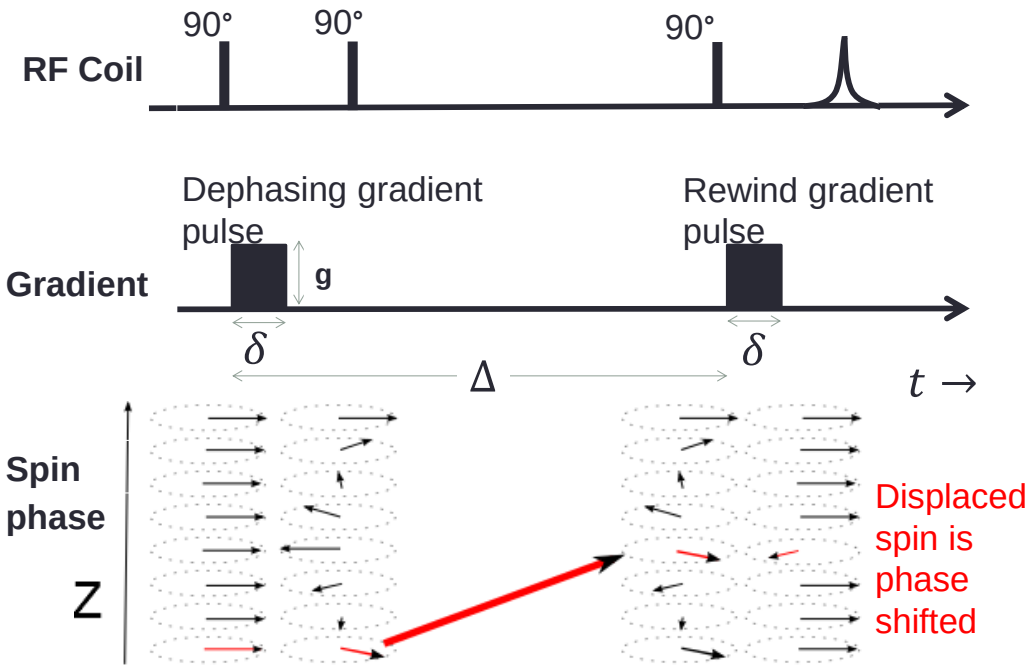

Figure 2.7. The pulsed gradient stimulated echo experiment encodes for translational motion of the spins within the sample. Displacements of spins in the direction of gradient application during the observation time, Δ, results in a phase shift when signal is acquired.

The PGSE sequence is most often ran multiple times with incremental gradient values. Therefore, the normalized echo signal is often viewed as the echo at a certain gradient point. The normalized echo attenuation at gradient point g is:

$$E(g) = \exp\left[i\gamma\delta\boldsymbol{g}\cdot\boldsymbol{v}\Delta - \gamma^2 g^2\delta^2 D(\Delta - \frac{\delta}{3})\right] \tag{2.34}$$

When there is no bulk flow in the sample, (2.34) simply reduces to the Stejskal-Tanner relation for the attenuation of the echo amplitude[44]:

$$S(g)/S(0) = \exp\left[-\gamma^2 g^2\delta^2 D(\Delta - \frac{\delta}{3})\right] \tag{2.35}$$

The Stejskal-Tanner relation shows that the signal attenuation at a certain gradient point normalized to the zero gradient point is a function of parameters of the pulse sequence, the gyromagnetic ratio, and the diffusion coefficient. The slope of $\gamma^2 g^2 \delta^2 (\Delta - \frac{\delta}{3})$ versus the log of signal echo attenuation of multiple gradient points is the self-diffusion coefficient. The Stejskal-Tanner method for finding self-diffusion coefficients can be used for systems which do not display purely diffusive motion; for example stochastic motion which changes depending on the observation time scale, such as restricted diffusion and polymer reptation[18], and systems which display stochastic motion due to mixing, such as turbulence and dispersion. In each of these cases, it is necessary to analyze the diffusion only over the gradient range which corresponds to 10% to 30% signal attenuation. The reason for this is that the probability of displacements to occur requires higher and higher moments of the probability distribution function as one moves away from the mean displacement. Near the mean displacement, the probability of displacement will have Gaussian characteristics and can be more easily described with the second moment of the probability distribution, which is the mean squared displacement of the molecules and corresponds with the diffusion coefficient.

A third relation between the PGSE experiment and translational motion is with use of the propagator. In the special case of the narrow gradient pulse approximation ($\delta \ll \Delta$) such that spins don't move considerably, (2.36) is valid.

$$E(\boldsymbol{g}, \Delta) = \int \rho(r) \int P(\boldsymbol{r}|\boldsymbol{r}', \Delta) \exp(i\gamma\delta \boldsymbol{g} \cdot [\boldsymbol{r} - \boldsymbol{r}']) d\boldsymbol{r}' d\boldsymbol{r} \tag{2.36}$$

Equation (2.36) states that the PGSE echo signal, when applying a gradient, $\boldsymbol{g}$, and using an observation time, Δ, is equal to the sum of all signal phase shifts from all spins due to displacements from their initial locations $\boldsymbol{r}$ to their final locations $\boldsymbol{r}'$ over the observation time. In order to define the signal space in which the propagator is sampled, the variable $\boldsymbol{q}$ is defined: $\boldsymbol{q} = \gamma\delta\boldsymbol{g}$. Note that $\boldsymbol{q}$ is simply the area under the square gradient pulse in the PGSE experiment multiplied by the gyromagnetic ratio. Now, (2.36) can be re-written using the new variable $\boldsymbol{q}$**.**

$$E(\boldsymbol{q},\Delta) = \int \rho(r) \int P(\boldsymbol{r}|\boldsymbol{r}',\Delta)\exp(i\boldsymbol{q}\cdot[\boldsymbol{r}-\boldsymbol{r}'])d\boldsymbol{r}'d\boldsymbol{r} \tag{2.37}$$

In Equation (2.37), it is clear that phase shifts only depend on the dynamic displacement**:** $\boldsymbol{R} = \boldsymbol{r} - \boldsymbol{r}'$**.** Equation (2.37) can be further simplified by the definition of the average propagator $\overline{\mathrm{P}}$:

$$\overline{\mathrm{P}}\ (\boldsymbol{R},t) = \int \rho(\boldsymbol{r})P(\boldsymbol{r}|\boldsymbol{r}+\boldsymbol{R},t)d\boldsymbol{r} \tag{2.38}$$

Equation (2.38) shows that the propagator is the probability that a particle displaces by $\boldsymbol{R}$ over the time interval t. Applying both of these changes to (2.38) yields (2.39):

$$E(\boldsymbol{q},\Delta) = \int \overline{\mathrm{P}}\ (\boldsymbol{R},\Delta)exp(i\boldsymbol{q}\cdot\boldsymbol{R})d\boldsymbol{R} \tag{2.39}$$

Equation (2.39) displays a Fourier transform relation between the echo signal and the propagator. A resolved propagator (many *q*-points) is worth a thousand words in describing molecular dynamics.

Multidimensional NMR

Multidimensional NMR experiments correlate populations of spins in multiple parameter spaces [45]. The additional range provided by the additional dimension allows for better differentiation of the ensembles of molecular scale interactions occurring within a system. Examples of 2D NMR experiments of this type include T_1-T_2, T_2-T_2, and D-T_2. By tacking a CPMG onto the end of a T_1 inversion recovery, another CPMG, or a PGSE, spins which experience the relaxation or dephasing from the first part of the pulse sequence are then subject to an entire CPMG train, during which the echo signal is acquired. Regardless of the experiment, this concept of multiplexing, or the encoding of signal in multiple independent dimensions, is what defines multidimensional NMR.

The Inverse Laplace Transform

Common in the analysis of the three experiments listed above is the use of the inverse Laplace transform (ILT) to reveal the distribution of relaxation rates or diffusion coefficients of the NMR signal, as well as the intensity weighting of these distributions. The inverse Laplace transform of the NMR signal, $S(t)$, and the forward Laplace transform of the distribution of relaxation rates present in the sample, $f(R)$, are shown in (2.40):

$$f(R) = L^{-1}\{S(t)\}$$
$$S(t) = L\{f(R)\} = \int_0^\infty f(R)\exp(-Rt)\,dR \tag{2.40}$$

It is apparent from (2.40) that the ILT is a valuable tool of the NMR experimenter, however it is ill posed and must be implemented carefully.

The ILT is ill posed because numerical solutions of its analytical expression diverge from the true solution with the presence of noise and are not unique solutions. One method of implementation is the regularized non-negative least squares inversion. First, this method requires that all relaxation rates present in the distribution $f(R)$ be positive. The method deems the 'simplest solution' which minimizes the mean-squared error to be the best solution. By choosing the simplest of the solutions, smooth distributions of the fewest number of populations are favored over narrow peaked distributions of many relaxing populations. This is known as the principle of parsimony, and is implemented with a smoothness operator. The weight on the smoothness operator, α^2, can be varied, and the challenge to the experimenter is to pick the α^2 which minimizes the error but only just. The importance of this is the realization that distributions found by the regularized non-negative least squares method are prone to 'pearling', creating multiple peaks to represent a single population.

Using the ILT in the analysis of the two dimensional data sets from T_1-T_2 and D-T_2 experiments, populations of spins with a certain T_1 or diffusion coefficient are correlated to also having a certain T_2. The T_2-T_2 experiment includes a mixing time before the second CPMG sequence and can reveal spins which have changed their T_2 relaxation rate during the mixing time due to changes in environment by movement or (hydrogen) exchange.

<u>T_1-T_2 Correlation Experiment</u>

The T_1-T_2 correlation pulse sequence, shown in Fig. 2.8., is essentially a CPMG sequence tacked onto the end of an inversion recovery sequence. Both of these standard

experiments were discussed in Chapter 1. First, the inversion recovery portion starts with a 180° pulse which inverts the net magnetization along the longitudinal axis. The magnetization must relax back to equilibrium solely by T_1, or spin-lattice relaxation. During the inversion time, t_1, the magnetization makes some portion of its exponential decay towards its equilibrium value. The 90° pulse brings the magnetization back into the transverse plane, and the signal, which has already been encoded for T_1 during t_1, will be encoded for T_2 during t_2. The CPMG train is a series of 180° pulses spaced by 2τ. Between consecutive 180° pulses, the dephasing due to magnetic field inhomogeneity is refocused in an echo. If the pulses are close enough together then the echo signal lost between each echo is due solely to T_2. The NMR spectrometer turns on the receiver in between sending out RF power for the 180° pulses to acquire the echo train. The pulse sequence cycles through a list of incremented inversion times and, after some phase cycling and averaging, the final product that is extracted from the data is a two dimensional data set containing the maximum signal acquired from each echo in the echo train for every inversion time. So, for example, an experiment with 32 inversion times and 6000 acquired echoes for every inversion time will result in a data matrix of size 32X6000.

The signal located in each cell has experienced a certain amount of T_1 relaxation during an inversion time, t_1, and a certain amount of T_2 relaxation during the preceding portion of the CPMG train, t_2. A two dimensional inverse Laplace transform (2D ILT) pulls out the relaxation rates and the magnitudes of the populations with these relaxation rates that are necessary to fit the data.

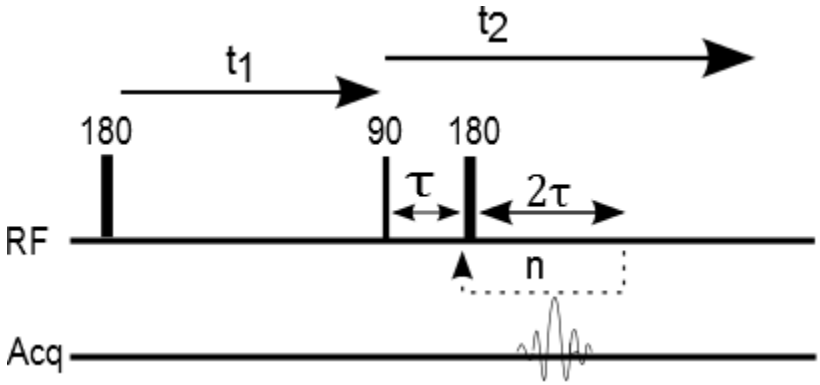

Figure 2.8. The T_1-T_2 pulse sequence

The T_1 and T_2 values associated with each population relate to the type of molecule on which the spins are attached as well as the molecular environment of the spins. The reasons for this can be explained through the rotational correlation model, shown in Fig. 1.3 and discussed in chapter 1.

T_2-T_2 Exchange Experiment

The T_2-T_2 exchange experiment, shown in Fig 2.9, is two CPMG sequences separated by a stimulated echo. The transverse magnetization sees some amount of T_2 relaxation, dictated by the number of echoes in loop n and the τ time, and is then stored in the longitudinal axis for a mixing time. The mixing time allows spins to change T_2 environments by displacement or chemical exchange (if there are multiple types of ionically bonded protons within the sample). The signal, which was encoded for T_2 during the first CPMG train, t_1, is encoded at a later time during the second CPMG sequence, t_2, with the receiver gated to acquire the peak of each echo. The data analysis is the same as for the T_1-T_2 sequence.

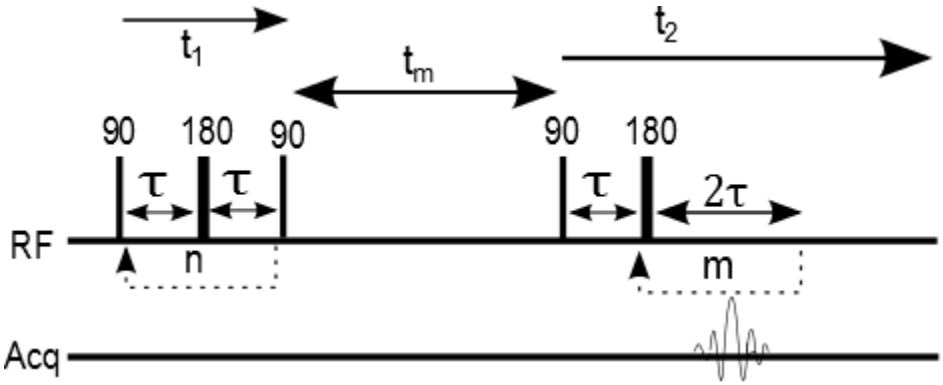

Figure 2.9. The T_2-T_2 pulse sequence

The resulting correlation maps show populations at locations corresponding to values of T_2 during the first and second encoding periods: (T_2^{1st}, T_2^{2nd}). Populations lying on the $T_2^{1st}=T_2^{2nd}$ line are spins with the same T_2 during both encoding periods. Populations off of this line were in different environments during the two encoding periods. Though exchange still occurs during the encoding periods, the growth in off axis peaks with increased mixing time can give a time scale of the exchange process [46].

Velocimetry

By combining pulsed gradients with an imaging sequence, diffusion and flow due to signal attenuation and phase shift within each pixel can be revealed. One such sequence is shown in Fig. 2.10. This sequence is robust; it can lead to images revealing the self-diffusion/dispersion coefficient or the bulk velocity within each pixel, or one could obtain propagators for each pixel. This sequence is sufficient for systems that show flow patterns that exist over long periods of time such as laminar flow. It is not capable of measuring time-sensitive flows such as turbulence due to the time needed for such an experiment being much longer than the time scales of fluctuations in flow patterns. The

spin precession phase shift of two points in *q*-space is all that is required to image velocity, so for this goal typically the sequence will ramp through only two PGSE gradient values.

Many velocimetry pulse sequences have been developed for imaging time-sensitive flows. The fastest methods are capable of acquiring all *k*-space points in one pass. One example, rapid acquisition relaxation enhanced imaging (RARE), involves a CPMG type echo train, phase encoding to different starting points in *k*-space so that the read gradient traverses different lines of *k*-space each time.

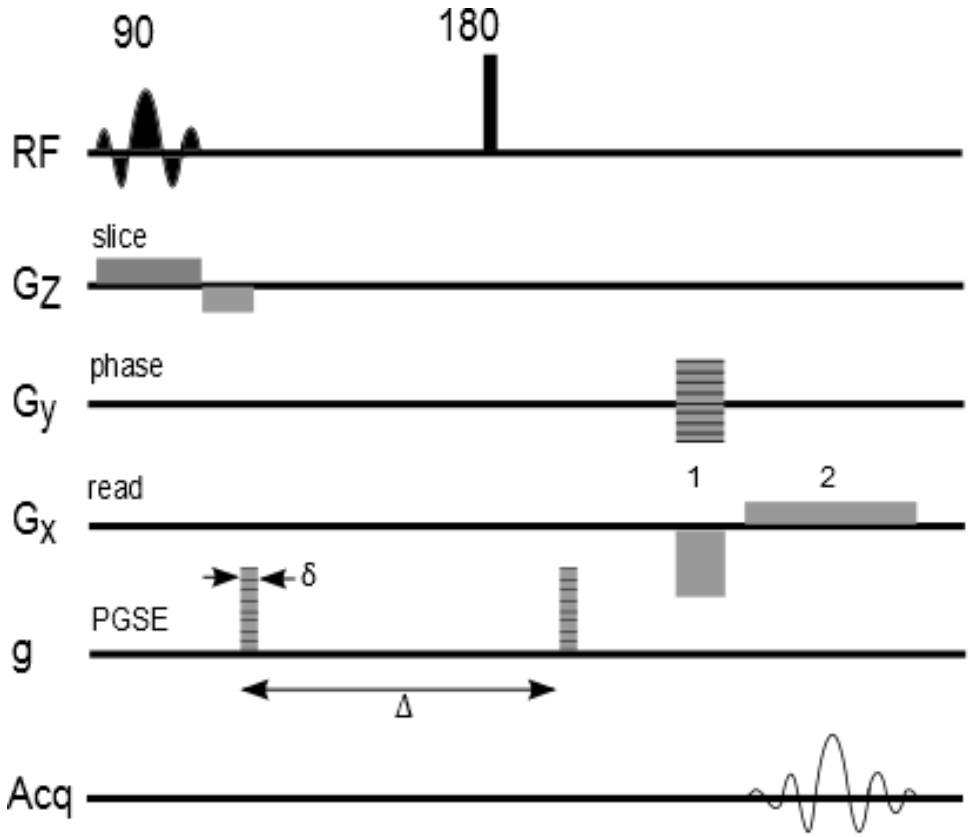

Figure 2.10. Dynamic imaging pulse sequence

DROPLET DRYING MODEL FOR SPRAY DRIED DISPERSIONS

Introduction

Spray drying is the industrial choice for creating dried powders such as detergents, dried milk, coffee extracts and solid dosage pharmaceuticals [47]. By spraying a feed solution, emulsion, or suspension through an atomizer into a chamber with hot inert gas, liquid droplets are dried.

Spray drying with solubilizing polymers has been shown to produce amorphous dispersions of insoluble drugs which can be more readily absorbed into the blood stream than neat active pharmaceutical ingredients (APIs) due to improvement in sustained supersaturation of free drug in the GI fluid [48]. Though APIs are often quick to crystallize, by spray drying with an ingestible amphiphilic polymer, such as hydroxypropyl methylcellulose acetate succinate (HPMCAS), APIs are locked in a kinetically stable state due to the small rate of diffusion within the solid form. HPMCAS has a high glass transition temperature that results in the glassy, low mobility, state of the solid SDD at ambient conditions. Acetone is a common solvent for making spray dried dispersions (SDDs) due to its high volatility at ambient temperature and solvation properties. Depending on the product, the temperature of the inlet drying gas stream can be well above or below the boiling point of the solvent, but due to evaporative cooling, SDDs have minimal exposure time (typically, much less than 1 sec) to the inlet gas. Hence, the bulk gas temperature in the chamber is much lower than the inlet drying gas temperature, which lowers the risk of denaturing the drug. Creating and maintaining an amorphous dispersion requires balancing drug loading in the dispersion, throughput (i.e.

solvent choice, drying gas flow rate, solution flow rate, and process temperatures), and residence time within the dryer.

Droplet drying history contributes to determining SDD chemical and physical stability, dissolution performance and particle and bulk powder properties. Droplet drying history, such as time of exposure to different temperatures and to varying partial pressures of solvent, leads to the formation of time dependent concentration gradients within the droplet. As such, the goal of this research is to improve understanding of how macro-scale process conditions impact droplet drying and droplet drying history. A model to predict the evolving radial concentration of a drying droplet containing acetone and HPMCAS was developed and preliminary testing completed[1]. What follows is the theory behind the droplet drying model, which Handscomb and Kraft first used to develop a model to simulate any spray-dried droplet [1, 49, 50]. In doing so, many of the features specific to certain drying droplets are generalized. In order to pick out necessary features from Handscomb and Kraft's model, a more specific look at spray-dried dispersions is taken during model development.

Following a generalized liquid droplet with dissolved solids through the drying process, surface moisture is removed at a constant rate until the droplet forms a surface shell due to its high solids content [51]. The droplet temperature will tend towards the wet bulb temperature, and will stay slightly above that temperature as long as the surface is saturated with moisture [1].

---

[1] This feasibility model is expected to eventually be extended to model droplet drying behavior of API-containing formulations as well as formulations containing alternate solvents and polymers.

The wet bulb temperature is the lowest temperature that a liquid saturated surface can reach during drying by a bulk gas phase at a given temperature and pressure. If the gas stream is not humid before hitting the surface, then the gas temperature is defined as the dry bulb temperature [52]. With acetone solvent, this will mean a significant drop in temperature. A psychrometric chart of an acetone-nitrogen system can give a fair estimate; a drop of pure acetone will cool to -10° C (the wet bulb temperature) if dry nitrogen gas at 20° C (the dry bulb temperature) is blowing onto it [53]. Evaporative cooling, such as is described here, largely prevents droplets and hence API from being exposed to the inlet gas temperature.

Before and after shell formation, depending on the structural properties of the shell, the droplet will shrink due to solvent volume loss. Drying will transition from a constant rate to a falling rate when the moisture at the droplet surface falls below a critical value, which may coincide with shell formation [51]. As the surface moisture content drops below saturation, the droplet temperature rises towards the boiling (or dry bulb) temperature. As the solvent which wets the droplet surface evaporates, the liquid forms menisci in the gaps between solid particles. The menisci support a pressure drop between the gas-phase pressure and the liquid just inside of the menisci equal to $\Delta P = \frac{2\gamma}{R_M}$ where γ is the surface tension of the liquid phase and R_M is the radius of curvature of the menisci [50]. When first forming, the shell will deform easily to the applied pressure and the radii of curvature stay large. As the shell thickens and becomes more closely packed with solids, its strength increases and it can support menisci with smaller radii of curvature.

The pressure drop across the menisci put the liquid phase under tension and drive the solid particles toward the center of the droplet to equilibrate. The shell will continue to thicken and the droplet will continue to shrink as long as the pressure drop across the shell is great enough to buckle the shell. If the pressure drop across the shell is no longer large enough to buckle the shell, then the shell is structurally capable of supporting itself and the droplet stops shrinking.

At this point, two extreme methods of moisture removal are possible due to the droplet morphology. In dry shell drying, the droplet evaporates off solvent at the growing shell-droplet core interface and solvent travels as a vapor through the porous solid shell. Wet shell drying will occur if the shell remains moist and is accompanied by bubble formation due to the necessity of volume conservation. When the bubble meets the shell and can expand no further, dry shell drying is invoked. Among these drying methods, droplet morphologies can deviate from the ideal. These drying routes and particle morphologies which can be observed in spray drying are seen in Figure 3.1.

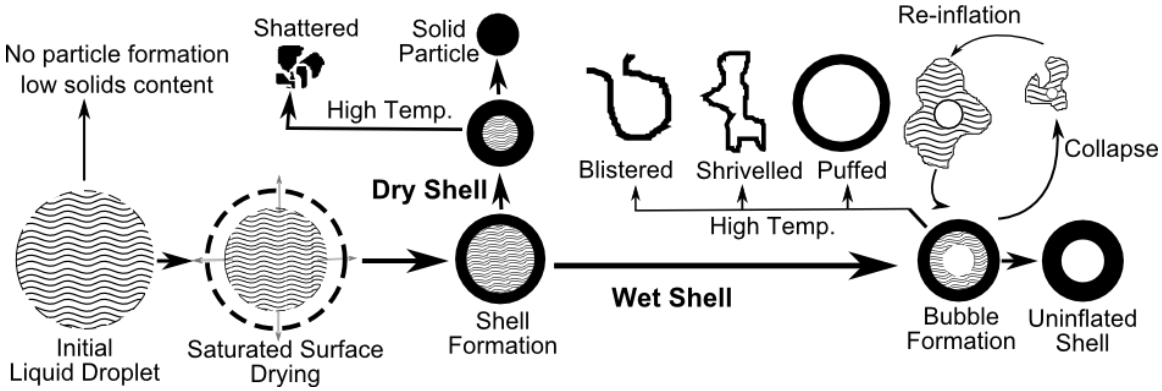

Figure 3.1. Schematic showing the types of drying that can occur as well as the possible particle morphologies for a spray dried droplet containing suspended solids[1].

Model Development

The Handscomb and Kraft model includes a core droplet description and structural sub-models. The core droplet description is a volume-averaged transport equation for the solute within an ideal binary solution and a population balance equation for the discrete suspended solids. These equations are coupled due to solute which can nucleate or grow solid particles and the intrinsic volume average over the continuous phase which models the effects of a changing porous network. A structural sub-model (shell thickening, wet shell, dry shell, or slow boiling) is enacted to simulate various particle morphologies and drying routes. Upon shell formation, the shell thickening sub-model is assumed and, based on changing pressures acting on the droplet as well as the strength of the shell, the model can switch structural sub-models. It may be possible to capture the drying dynamics of a SDD utilizing certain parts of the Handscomb and Kraft model.

Currently, the SDD will be modeled as a binary mixture of acetone and HPMCAS. In extending the model to include API, the system will be viewed as a pseudo-binary mixture where API and polymer are lumped together into a single solute component solvated by acetone. The ability to model solute, solvent, and solid, as is presented in Handscomb and Kraft's model, adds the next level of complexity and should be undertaken if the simpler model inadequately represents drying dynamics when API is present, or if the model goals include spatial evolution of API concentration.

An energy balance over the entire droplet will take into account the mass transfer dynamics changes with temperature. Certain morphological features will be included in

the model with the assumption that all SDDs follow the same drying route. This model will be useful in predicting droplet drying times and acetone moisture profiles throughout drying at various spray drying parameter values such as; inlet gas temperature, solution flow rate, temperature and composition, relative droplet velocity, and initial droplet diameter. Though the evolution of droplet morphology assumes a spherical droplet, the predicted final droplet surface area and volume may be useful information.

Governing Transport Equation

With acetone self- diffusion coefficients as a function of HPMCAS polymer concentration known for the HPMCAS-acetone binary solution, the polymer can be modeled as part of the continuous phase.

The differential mass balance on solvent, A, with no chemical reactions and assuming constant density, is:

$$\rho \frac{\partial \omega_A}{\partial t} + \boldsymbol{\nabla} \cdot \boldsymbol{n}_A = 0 \tag{3.1}$$

where ω_A is the mass fraction of solvent and $\boldsymbol{n}_A$ is the mass flux of solvent relative to a fixed reference plane. The mass flux of solvent, assuming Fick's Law of Binary Diffusion to be valid, has the form [54]:

$$\boldsymbol{n}_A = \rho_A \boldsymbol{v} - \rho D \boldsymbol{\nabla} \omega_A \tag{3.2}$$

where $\boldsymbol{v}$ is the mass averaged velocity of the fluid at a position. Fick's law states that the flux of mass is proportional to the gradient in concentration, and therefore D is by definition the concentration diffusion coefficient. Nonequilibrium thermodynamics predicts that other diffusional driving forces will arise in the presence of a pressure or

temperature gradient [54]. With the assumption of a low Biot Number [1], the temperature gradient is negligible. The pressure gradient, which could be on the order of 40 MPa over the droplet shell [50], will be currently neglected. Within nonequilibrium thermodynamics, concentration diffusion also implies diffusion due to an activity gradient. For a binary system, the activity is primarily a function of the mass fraction. It may be possible to use a mutual diffusion coefficient as a function of mass fraction to take this into account and continue to follow the Fick's Law approach. Note also that NMR self-diffusion coefficient data may be used for this purpose if knowledge of activity coefficients can be obtained [55].

To find closure to the flux form (3.2), it is necessary to analyze how the diffusion of one species will impart motion on the other, and thus $\boldsymbol{v}$. Boundary conditions are utilized for this. When the droplet is shrinking, the mass flux of one component being equal and opposite to the mass flux of the other component is valid and necessary to satisfy continuity when there is no density variation among the components and mixtures. This arises due to the boundary condition that the evaporative flux is equal and opposite the flux of mass towards the droplet center. In the shell, the polymer is deemed stagnant; its flux is zero. In the droplet core, during wet shell drying, the boundary condition at the bubble interface shows that $\boldsymbol{v} = \boldsymbol{v}_{Bub}$, the rate of bubble growth in the radial direction. Table 1 shows all of the flux forms and over which domains the model uses them. More information on the domains is given in the section titled 'Structural sub-model'.

Table 3.1. The flux forms used in the model and their respective domains

Domain of Interest	Solvent Flux Form
Droplet before shell formation, Droplet core during shell thickening	$\boldsymbol{n_A} = -\rho D \boldsymbol{\nabla} \omega_A$
Droplet Shell	$\boldsymbol{n_A} = -\frac{\rho D \boldsymbol{\nabla} \omega_A}{1 - \omega_A}$
Droplet core during wet shell drying	$\boldsymbol{n_A} = \rho_A \boldsymbol{v_{Bub}} - \rho D \boldsymbol{\nabla} \omega_A$

The droplet is approximated as a perfect sphere with gradients in concentration only occurring in the radial direction. This allows solving only the differential mass balance in the radial direction to be necessary.

The differential mass balance is coupled to an energy balance by the saturation pressure and the diffusion coefficient, both due to their temperature dependence. Also, the shell is the volume of the droplet which is in a glassy state; this is defined by the droplet temperature being below the local glass transition temperature. Other parameters are assumed to negligibly impact the drying dynamics and their values are calculated at an average temperature over the drying history and held constant. The dimensionless Biot number is the ratio of thermal resistance inside the droplet to the thermal resistance in the boundary layer between the bulk gas and the droplet surface. There is assumed to be no temperature variation within the droplet because the Biot number is small for drying droplets [1]. The energy balance over the entire droplet of radius, R, is:

$$\frac{4}{3}\pi R^3 \rho \left(C_{pA}\omega_A + C_{pB}(1-\omega_A)\right)\frac{dT}{dt} = \dot{Q} - m_{vap} 4\pi R^2 \left(\Delta H_{vap} + C_p(T_{ref} - T)\right) \tag{3.3}$$

The heat capacity, C_p, is assumed constant with respect to temperature. The rate of heat penetrating the droplet, $\dot{Q}$, and the rate of acetone evaporation, m_{vap}, are both calculated by a method which Abramzon and Sirignano (1989) used in their 'Droplet vaporization model for spray combustion calculations'[56].

Boundary Conditions

Acetone will leave the droplet surface due to an activity gradient between acetone in the liquid droplet interface and the bulk gas phase, whereas all non-volatile HPMCAS will stay within the droplet [1]. The boundary condition at the droplet surface is found by equating the flux of solvent at the droplet surface to the vaporization flux [1]:

$$\frac{\rho}{\omega_A} D \frac{\partial \omega_A}{\partial r}\Big|_{r=R} = m_{vap} \tag{3.4}$$

Volume conservation necessitates that the solvent mass flux be related to the rate of droplet shrinkage, before shell formation and during shell thickening, by [1]:

$$\frac{dR}{dt} = -\frac{m_{vap}}{\rho_A^0} \tag{3.5}$$

where ρ_A^0 is the density of the pure solvent. The evaporative flux from the droplet surface is calculated using a method, based on film theory [54], developed by Abramzon and Sirignano (1989) [56]:

$$m_{vap} = 2\pi \bar{\rho}_g \bar{D}_g R \, Sh^* \ln(1 + B_M) \tag{3.6}$$

Where $\bar{\rho}_g$ and $\bar{D}_g$ are the average density and binary diffusion coefficient in the gas film, and $B_M = \frac{Y_{As} - Y_{A\infty}}{1 - Y_{As}}$ is the Spalding mass transfer number. The Sherwood number is the ratio of convective to diffusive mass transfer within the gas film between the droplet

surface and the bulk gas. Equation 6 uses a modified Sherwood number, Sh^*, which accounts for the larger film thickness due to the presence of Stephan flow. The mass fraction of solvent vapor at the surface of the droplet, Y_{As}, can be approximated from the mass fraction in the liquid phase by a modified form of Raoult's Law which accounts for the non-ideality within the liquid mixture by including the activity coefficient [26]:

$$Y_{As} = \gamma_A^L \omega_A|_{r=R} \, P_A^*/P \tag{3.7}$$

The vapor saturation pressure for the pure solvent as a function of temperature, $P_A^*(T)$, for many common pure liquids, including acetone, is well defined. The activity coefficient at the liquid droplet surface, γ_A^L, is a function of the component ratios and temperature, neglecting pressure effects.

Assuming droplet symmetry allows for a zero net flux boundary condition at the droplet center. For the boundary condition at the shell interface, the flux of solvent from either side of the shell is set equal.

During the wet shell drying regime, a symmetric bubble forms at the center of the droplet [49]. This bubble is assumed to be saturated vapor, and any solvent flux necessary to form the bubble is neglected. Thus, the boundary condition at the bubble edge is:

$$\rho D \frac{\partial \omega_A}{\partial r}|_{r=R_{Bub}} = \rho_A^0 \boldsymbol{v}_{Bub} \tag{3.8}$$

The rate of bubble growth, $\boldsymbol{v}_{Bub}$, is related to the volume loss during wet shell drying by:

$$\boldsymbol{v}_{Bub} = \frac{m_{vap}}{\rho_A^0}\left(\frac{R}{R_{Bub}}\right)^2 \tag{3.9}$$

where R_{Bub} is the bubble radius. Note from equation 9 that the bubble radius must be initially present with a finite length to avoid an infinite bubble growth rate.

Structural Sub-models

The choice of which structural sub-models to add to the model and when they should be enacted within the model is based on knowledge of SDDs. Scanning electron microscope (SEM) images of SDDs post-drying published in Friesen et al. (2008) show particle collapse and shriveling [48]. The polymeric skin of SDDs deform in response to the pressure drop over the shell during drying, reducing the droplet volume. Note that this is different than the shell buckling in particulate droplets because the surface area of the polymeric skin is fixed during deformation. The SEM images of SDDs show wrinkles with widths on the sub-micron scale [48]. One could imagine high pressure-drops forcing the polymer shell to fold in and engulf itself. This engulfing process could be the way that a polymeric skin buckles. If so, then shell thickening should be included in the drying droplet model. It has been found by Bend Research Inc. that dried SDDs are typically hollow. Including the formation and growth of a centrally located bubble within the droplet will take into account the hollow nature of the SDD as well as the constant surface area but changing volume which an initially spherical droplet must undergo to become collapsed and shriveled.

With the only routes to a hollow, collapsed or shriveled particle in Figure 3.1 being through wet shell drying, the SDD droplet drying model will postulate wet shell drying, as opposed to dry shell drying, upon cessation of shell thickening.

It is necessary to create a decision-making process to dictate when a modeled SDD droplet will form a shell, when the shell should become stationary, and when wet shell drying should end:

Shell Formation. Polymer solutions show a transition from liquid to solid-like when cooled over a certain temperature range and a certain point within this rage is defined as the glass transition temperature, T_{glass}, which is a function of the polymer concentration. The shell will be defined by where the local glass transition temperature is greater than the droplet temperature.

Stationary Shell. To find when the shell can hold up against the pressure acting over it, we look to the Handscomb and Kraft model, where it is seen that this will occur when the following inequality is satisfied [50]:

$$\frac{R(R-T)}{T} * m_{vap} < \frac{k}{\mu_A} \frac{2E\rho_A^0}{\sqrt{3(1-\nu^2)}} \tag{3.10}$$

In (3.10); R is the particle radius, T is the shell thickness, m_{vap} is the evaporative flux of solvent off the droplet, k is the permeability of the shell, μ_A is the viscosity of the solvent, ρ_A^0 is the solvent material density, E is the Young's modulus of the shell, and ν is its Poisson's ratio. Assuming that these parameters do not vary with the changing droplet conditions, the right hand side of (3.10) is a constant. The permeability could be estimated based on Clague's 1997 model for fibrous media if the solids (polymer) volume fraction was known [57]. Literature values of Young's modulus and Poisson's ratio for a similar polymer in the glassy state should suffice for use in (3.10).

A final note about the parameters on the right hand side of (3.10) is that one could potentially design when spray dried particles will become rigid by altering these parameters, for example by decreasing the degree of polymerization of the polymer one would expect to decrease the Young's modulus of the shell, and therefore postpone when

the shell stops thickening. Equation (3.10) is based on Darcy's law, used to obtain the pressure acting on the shell due to solvent flow through its pores, and Timoshenko's derivation of when a spherical shell will buckle under a uniform external pressure.

End of Wet Shell Drying. The simulation ends at the end of wet shell drying; this is the point when the central bubble reaches the shell and can expand no further. In the Handscomb and Kraft model this defines the transition point to dry shell drying [49]. All of the equations which the code uses to decide when to switch sub-models are seen in Figure 3.2. The figure also gives visualization for what the evolution of the modeled droplet looks like.

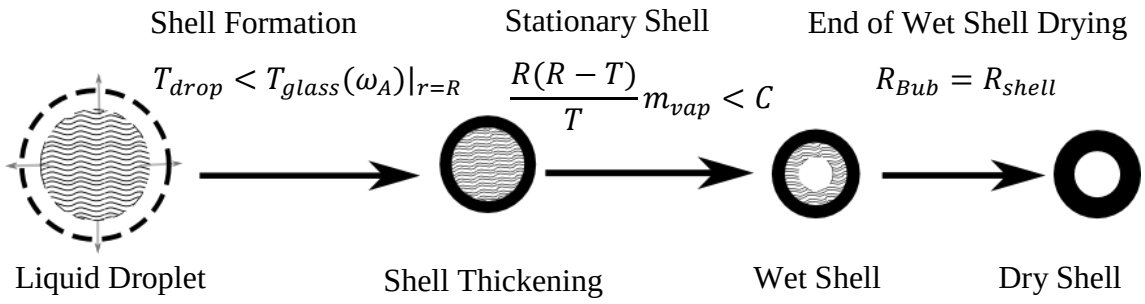

Figure 3.2. The decision making process for switching sub-models. Each droplet figure and corresponding sub-model name signifies the essential modeling domains (droplet core, shell, bubble, and dry shell). The three equations are used to decide when to switch sub-models. C equals the right hand side of equation 3.10.

Model Implementation

The model was implemented in MATLAB using the finite difference method to approximate the solutions to the governing transport equation. At the time of writing this thesis, the model included only the liquid droplet drying sub-model, though a shell with a thickness of one tenth the droplet radius was used to have finely spaced nodes over the

region of strong concentration gradient. The energy balance has not yet been implemented. Values pertinent to the calculation of the boundary condition were rough estimates on the conditions within the spray dryer. The MATLAB code is included in Appendix B of this thesis.

The governing transport equation in spherical coordinates after combining (3.1), (3.2), the solvent flux form for the droplet before shell formation from Table 3.1, and enacting the differential operators is:

$$\frac{\partial \omega_A}{\partial t} = -v_{mesh}\frac{\partial \omega_A}{\partial r} - D_a\frac{2}{r}\frac{\partial \omega_A}{\partial r} - \frac{\partial D_a}{\partial r}\frac{\partial \omega_A}{\partial r} - D_a\frac{\partial^2 \omega_A}{\partial r^2} \tag{3.11}$$

The v_{mesh} term is necessary to subtract out the artificial bulk flow due to the changing particle radius and thus nodal point locations. At each node, v_{mesh} is the velocity of the node and is simply a linear interpolation between 0 at the droplet center and $\frac{dR}{dt}$ at the droplet radius. The spatial derivative of the diffusivity is nonzero because it is a function of concentration. The terms v_{mesh} and $D_a = fn(\omega_A)$ make this a nonlinear partial differential equation that must be approximated by numerical methods. The finite difference method [58] was chosen due to simplicity of implementation.

The code uses 10 equally spaced nodes in the droplet core and 10 equally spaced nodes in the droplet shell with one shared node. The code involves stepping through time in the outer loop and stepping through space in the inner loop. At each timestep, the finite difference method sequentially approximates the change in nodal concentrations by approximating the spatial derivatives in the governing transport equation with linear gradients in concentration between nodes from the previous time step. Applying the

finite difference method [58] to (3.11) and solving for the concentration at node j and time step $i+1$ results in:

$$\omega_{A,i+1,j} = \omega_{A,i,j} + \Delta t\left(-v_{mesh}\frac{\omega_{A,i,j+1}-\omega_{A,i,j}}{h} - D_a\frac{\omega_{A,i,j+1}-\omega_{A,i,j-1}}{Rh} - \frac{D_{a,i,j+1}-D_{a,i,j-1}}{2h}\frac{\omega_{A,i,j+1}-\omega_{A,i,j-1}}{2h} - D_a\frac{\omega_{A,i,j+1}-2\omega_{A,i,j}+\omega_{A,i,j-1}}{h^2}\right) \tag{3.12}$$

where Δt is the timestep size and h is the distance between nodes. The forward difference approximation looking upwind was used for the spatial derivative with v_{mesh} in order to avoid instability from the convective term feeding off this derivative. The first and second order central difference approximations were used for all other first and second order derivatives with respect to radius.

The parameters used in (3.6) to calculate the mass flux at the droplet surface are listed in Table 3.2. The thermodynamic activity in the modified Raoult's law was set to 1, thus essentially using the basic form of Raoult's law. The vapor saturation pressure (P_A^*) using the Clausius Clapyeron equation, heat of vaporization, viscosity, thermal conductivity, density, heat capacity, vapor diffusivity, and Prandlt number were found for pure acetone liquid and nitrogen gas at 300 K in Perry's Chemical Engineers' Handbook [59]. System-dependent parameters, such as the temperature, pressure, bulk acetone mass fraction in the gas phase, particle velocity, and droplet radius were rough estimates. The mutual diffusion coefficient in the liquid phase, D_a, is an exponential fit to the acetone self-diffusion coefficient data in Fig 4.1 at acetone mass fractions greater than 0.1. Note

that the mutual diffusion coefficient is not equal to a component's self-diffusion coefficient. The initial acetone mass fraction was set to 0.8 at all nodes.

Table 3.2. Parameters used in the model simulation

Parameter Name	Value
Avg. density in gas film ($\bar{\rho}_g$)	1.2 kg/m^3
Avg. diffusivity in gas film ($\bar{D}_g$)	1.3×10^{-5} m^2/s
Initial Droplet Radius	20 μm
Sherwood Number (Sh^*)	2.6
P_A^*/P	0.328
Bulk gas phase acetone mass fraction ($Y_{A\infty}$)	0.1
Diffusivity in liquid phase (D_a)	$4 \times 10^{-9} e^{-2.7(1-\omega_A)}$ m^2/s
Initial acetone mass fraction	0.8

The parameters in Table 3.2 were used in the drying droplet model with 1 million time steps. The time steps were quadratically spaced for more initial resolution while still allowing the model to run for 1 second. The mass fraction profiles at 50 quadratically spaced time steps are presented in Figure 3.3a. The initial condition is the line at a mass fraction of 0.8 from the radius of 0 to 20 μm. In the following time step, the mass fraction profile takes on a steep profile near the droplet surface while still maintaining 0.8 mass fraction solvent near the center. The mass fraction of acetone at the surface continues to drop and the flux of acetone to the surface moves further towards the droplet center in subsequent profiles. In the 5th profile, the acetone mass fraction at the center has dropped below its initial value of 0.8 and the droplet radius has decreased to 18.5 μm. The mass fraction at the droplet center first falls below 0.3 around 70 ms. The trend of decreasing fractions of acetone along subsequent profiles continues and the profiles flatten and begin

to change very little to not at all as equilibrium is approached and reached during the 1 second time interval. From the change in droplet radius during the 1 second, shown in figure 3.3b, it is clear that the droplet has equilibrated. The final mass fraction and droplet radius is 0.13 and 12.3 µm.

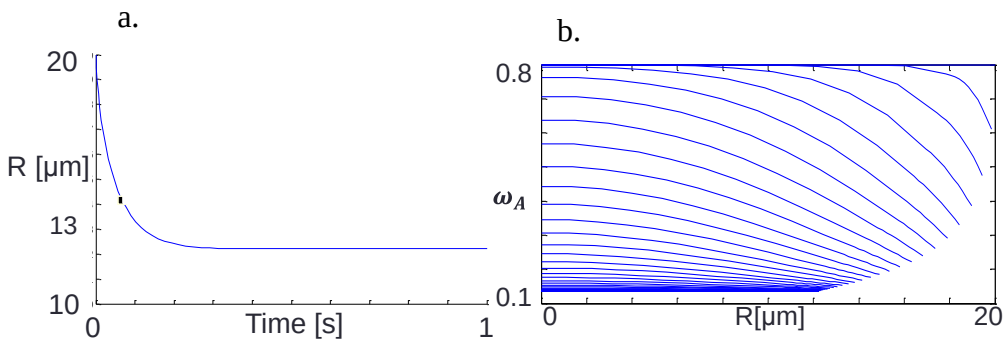

Figure 3.3a (left): The simulated mass fraction profiles at quadratically spaced time steps. The profiles evolve from the first profile at t=0 which is ω_A=0.8 at every node to the last profile at t= 1 s which is ω_A=0.13 at every node.
Figure 3.3b (right): The simulated droplet radius as a function of drying time.

From the change in volume, one can calculate the change in droplet mass and this can be compared to the change in mass of acetone. The ratio between these two values is 5.12, indicating that mass is not at all conserved. The reason for this is due to the approximation of the true curved profiles with straight lines, thus some of the acetone is lost in the model before it gets to the surface. Compounding this problem is the use of a million timesteps, however less timesteps caused divergence of solutions.

True spray dried droplets do not equilibrate with the gas phase during drying of a second, indicating that the model drastically under-predicts the drying time. The reason is the use of the acetone self-diffusion coefficient rather than the mutual diffusion

coefficient. The self-diffusion coefficient is proportional to the mean squared displacement of the molecules of interest over an observation time and the mutual diffusion coefficient is the ability of the system to rid a concentration gradient. Only when the mass fraction of the component of interest approaches zero are these equal, and the fit used for the diffusivity does not represent the drastic decrease from the logarithmic trend which occurs at low acetone concentrations. It is possible to create a mutual diffusion coefficient model based on the free-volume theory using the complementary data of inverse gas chromatography, sorption experiments, rheology, and PGSE NMR [24, 27, 60]. This is work in progress in collaboration with Dr. R.P. Danner's lab in the Department of Chemical Engineering at Penn State.

Future Work

More work is necessary to have a model that is close to validation. A diffusion coefficient model is the greatest setback. An energy balance and the additional sub-models still need to be added in. It is unknown whether the shell transitioning to a glassy state is the point when the shell first turns solid. At the glass transition, the shell will absolutely be solid, however the shell may appear solid on the drying time-scale with greater amounts of acetone present. This later definition seems more in line with a Deborah number description; at what concentration do the polymer molecules within the shell no longer relax and flow/shear past one another on the timescale of the changing droplet radius[61, 62]?

The right-hand side of (3.10) has many parameters which are difficult to identify, though a close guess may be adequate. The time to switch between sub-models should

not affect drying time predictions significantly due to this only affecting the droplet surface area which is accessible for evaporation.

At this time, the science behind the model seems appropriate for modeling a spray dried droplet. The finite-difference method may be limiting the model from converging when strong concentration gradients are present. Implementation of the actual, smaller, diffusivity within the model will predict an even stronger concentration gradient at the droplet surface and lead to increased problems. Other PDF approximation methods may be more appropriate for this problem.

This model will be revised for a tertiary system and track the API component. The current research is a necessary step towards this long-term goal.

DIFFUSION AND RELAXATION NMR TO PROBE THE DYNAMICS OF HPMCAS POLYMER MIXTURES

Introduction

Hydroxypropyl methylcellulose acetate succinate (HPMCAS) polymer is a pharmaceutical excipient commonly used to create spray dried dispersions (SDDs) of amorphous drug due to its significant bioavailability enhancement for drugs with low aqueous solubility[48]. In the spray drying process a solution of excipient, drug, and organic solvent (~85% wt.) such as acetone is pumped through an atomizer and into a drying chamber as a hot nitrogen gas stream quickly evaporates solvent off the initially liquid droplets, creating solid (<5% wt. acetone) spray dried particles in seconds. Residual solvent is removed over the course of hours during secondary drying. Once the SDD is incorporated into its final drug dosage form, for example a tablet, the dosage form must have quantified long-term stability or shelf life, during which time the drug is known to not crystalize.

Diffusive mobility of SDD components is a primary factor in the creation and maintenance of an amorphous homogeneous spray-dried dispersion. Droplet and particle drying are limited by diffusion of solvent to the surface. SDD stability is determined by mobility of the drug molecules through the polymer matrix, for which the translational and rotational polymer self-diffusion plays a critical role. Highlighted here is a study of the molecular-scale dynamics of HPMCAS/acetone mixtures by NMR.

Initial goals for this research included developing a droplet drying model relevant to HPMCAS-based spray-dried dispersions. The necessary parts of Handscomb's

generalized drying droplet model were identified and a straightforward approach to modeling the concentration profile of a drying droplet was laid out in Chapter 3. The primary unknown in this model was the mutual diffusion coefficient of the system as a function of temperature and concentration. Initially, this was the reasoning behind finding self-diffusion coefficients of HPMCAS/acetone mixtures with pulsed gradient stimulated echo (PGSE) NMR. It was shown in Chapter 2 that self-diffusion can be connected to mutual diffusivity through the free-volume theory of Vrentas and Duda [20, 21].

Measurements of HPMCAS self-diffusion indicates the polymer dynamics scale with concentration as established from polymer dynamics theory [63]. Interesting results were obtained with the use of the inverse Laplace transform (ILT) to separate HPMCAS populations based on rates of diffusion.

In NMR, spin-spin or T_2 relaxation is a parameter intrinsic to any experiment, as it governs the experimental timescale. With the removal of acetone, the system moves to greater degrees of solidity and the T_2 limits the experimental possibilities. The T_2 relaxation rate relates directly to and gives information about the molecular rotational mobility. It was found that T_1-T_2 experiments worked particularly well in identifying consistent relaxing populations. T_2-T_2 experiments revealed exchange between separate fast-relaxing populations. Variable temperature PGSE and T_1-T_2 experiments were run on two samples, with one sample (45% wt. acetone) in the rubbery state and the other sample (10% wt. acetone) near or below its glass transition temperature. These measurements determine the molecular dynamics associated with the glass transition.

Wet SDD was obtained, and PGSE, T_1, T_2, T_1-T_2, and T_2-T_2 experiments were performed on these near solid-state samples.

Past research involving PGSE in cellulosic excipient systems studied self-diffusion of the solvent and a solute component at solvent weight fractions above 0.5 [64, 65]. These researchers didn't study the polymer self-diffusion and to our knowledge no research has used multidimensional relaxation and diffusion NMR experiments on such systems. Solvent self-diffusion coefficient measurements by PGSE NMR were used in conjunction with sorption experiments by Yapel et al. to provide free-volume parameters for the mutual diffusion model of water in gelatin [24]. Self-diffusivity of water in gelatin was measured for five samples with weight fractions of water at and less than 0.37 at temperatures of 15.2° C and 40.2° C. In this research, solvent self-diffusion was studied over an extensive concentration range, creating the potential to test the free-volume theory.

PGSE NMR self-diffusion measurements of all three components of solutions containing polystyrene polymer, thetrahydrofuran solvent, and hexaflourobenzene as a ternary probe component, were published by von Meerwal, Amis, and Ferry [66] and showed good agreement with the reptation plus scaling model of de Gennes [67]. Researchers studying the hydrogel formation of Tropoelastin with PGSE NMR identified the nonlinearity of Stejskal-Tanner plots as being due to multiple aggregation states of Tropoelastin [68]. Similar conclusions are made in this research using nonlinear data fitting or Inverse Laplace Transform methods to obtain distributions of HPMCAS self-diffusivity.

Methods

Sample Preparation

The pharmaceutical excipient Hydroxypropyl methylcellulose acetate succinate MG grade (HPMCAS-MG) polymer made by Shin-Etsu Chemical Co., Ltd. was obtained from Bend Research Inc. LF grade (HPMCAS-LF) was obtained from Merck & Co., Inc. Mixtures of HPMCAS and acetone were prepared by stirring with magnetic stir plate and stir bar. For mixtures above roughly 75% wt. acetone, the samples were mixed to the desired concentrations and pipetted into 5 mm NMR tubes. Because the viscosities of mixtures below 75% wt. acetone were too great to pipette into NMR tubes, mixtures in this range were prepared by repeatedly adding more solution to NMR tubes and evaporating acetone. As acetone was the only volatile component, the final weight percent was determined by weighing. Once at the desired weight percent, tubes were equilibrated for times ranging from 4 days to half a year. Based on a mutual diffusivity estimate of 10^{-10} m^2/s and a diffusive length scale of 2 cm, the time-scale to equilibrate concentration gradients for these samples is 50 days. Roughly 25 samples containing HPMCAS-MG were prepared, and of these, 15 samples were repeatedly dried, capped, experimented on, and filled with more solution. Six of these repetitions were performed on 10 of the 15 tubes to attain samples of sufficient volume to fill the RF coil and provide concentrations less than 30% wt. acetone. Five tubes survived all 6 repetitions due to sample losses from breakage and bubble formation. Three samples containing HPMCAS-LF were made over a smaller range of weight fractions in order to compare the molecular dynamics between LF and MG systems.

Four samples of wet spray dried dispersion (SDD) obtained from Bend Research Inc. containing primarily HPMCAS and acetone, though some other solvents were present in minor proportions. The HPMCAS was the only non-volatile component. Two of the samples were collected before secondary drying (labeled 23B) and two more were collected after secondary drying (labeled 23A). Residual solvent analysis was performed on collections of the SDD batch pre and post-secondary drying using gas chromatography with a flame ionization detector. From this, it was determined that the SDD contained 2.28% wt. acetone pre-secondary drying and 1.58% wt. acetone post-secondary drying. The four samples were caped in 5 mm diameter NMR tubes and mailed overnight from Oregon to Montana in a chilled and insulated container. The SDD samples were then stored at -20° C to prevent sample change through aging or solvent loss.

Experimental Setup

PGSE Measurements. Pulsed gradient measurements were performed on a Bruker Avance III NMR spectrometer at a ^{1}H resonance frequency of 250.12 MHz with a Micro5 probe and gradient set, capable of applying 3 T/m in all directions, and a Diff30 gradient set, with 17.8 T/m maximum gradient strength in the z direction only. With the PGSE parameters used in this research, the maximum gradient of the Diff30 can attenuate the signal from hydrogen spins with a diffusivity of $3x10^{-13}$ m^2/s by 30%. The 90° RF pulse times were 100 μs. The dwell time and number of acquired points (real and imaginary) was 25 μs and 8192 points for experiments specific to the HPMCAS and 100 μs and 4096 points for experiments specific to the acetone, resulting in a sweep width of 80ppm (20,000 Hz) and 20ppm (5,000 Hz) respectively. Experiments used a 10 s

repetition time along with a spoiler recovery sequence to dephase any transverse magnetization before the start of consecutive scans. The PGSE experiments specific for acetone used 64 averages and those for HPMCAS used 128. Trapezoidal shaped gradient pulses with ramp times automatically set by the Diff module of TopSpin 3.2 were applied.The PGSE pulse sequence was shown and described in Fig. 2.7. The PGSE used gradient durations δ = 1 ms and observation times typically of Δ = 50 ms, though longer observation times were used to test for time-dependent dynamics. The τ time, the time between the first and second 90° pulses in the PGSE sequence, was between 1 ms and 3 ms, scaling with the maximum gradient. For Stejskal-Tanner analysis of PGSE experiments, 16 linearly spaced gradient values were used, with the maximum gradient specified such that the spectral component of interest saw roughly 30% attenuation (M/M_0=0.7). For data analyzed by inverse Laplace transform, 64 or 128 linearly spaced gradient values were used, with maximum gradients specified to see M/Mo between 0.1 and 0.7. Because of the short T_2 of the HPMCAS polymer relative to the acetone, it was found that spectral resolution of the HPMCAS could only be obtained for gradient values high enough to fully attenuate signal from the faster diffusing acetone. To accomplish this, the gradient list for experiments specific to the HPMCAS started with a gradient value of 1 to 4 T/m, corresponding to a $\gamma^2 g^2 \delta^2 (\Delta - \delta/3)$ of $3.6\text{x}10^9$ and $5.7\text{x}10^{10}$ s/m^2. These values are sufficient to reach 99% signal attenuation from spins with a diffusivity of $1.3\text{x}10^{-9}$ m^2/s and $8.1\text{x}10^{-11}$ m^2/s respectively. All parameters were tested on 5% water in deuterated water and glycerol and showed diffusivities consistent with published data[69] [70].

The parameters for PGSE experiments performed on the solvent in the wet SDD samples required adjustment due to the low solvent content and T_2 relaxation of the signal. For these experiments, δ was set to 0.55 ms and the maximum gradient value was 10 T/m. This shortened τ from 2.5 ms to 2 ms, which gave a significant increase in signal. The other major component of τ is the gradient stabilization time; a delay after each gradient pulse to allow the gradient in magnetization to decay away such that no gradient is present during the first RF pulse of the stimulated echo or acquisition. Decreasing this was not tested. A minimum of 1024 averages were used to obtain sufficient signal from the acetone.

Relaxation Measurements. T_1-T_2 correlation and T_2-T_2 exchange experiments were performed on a Bruker Avance III NMR spectrometer at a ^{1}H resonance frequency of 300.2 MHz with a Micro2.5 probe. These pulse sequences are shown in Fig. 2.8 and Fig 2.9. The 90° and 180° pulse times were 5 and 10 μs. The τ and dwell time was a minimum of 12 and 0.5 μs. The number of acquired echoes was 6000. The T_1 encoding portion of the T_1-T_2 experiments used 32 logarithmically spaced inversion times between 1 ms and 50 s and a repetition time of 25 s. The first T_2 encoding period of the T_2-T_2 experiments cycled the number of echoes through 32 logarithmically spaced and even whole numbers between 2 and 3908. The repetition time (TR) was 25 s for the T_1-T_2 experiments and 10 s for T_2-T_2 experiments.

Temperature dependent PGSE experiments with the 250 MHz spectrometer and T_1-T_2 correlation experiments with the 300 MHz spectrometer were performed on a 45% wt. ace. sample and a 10% wt. ace. sample at 6 K increments between 255 K and 303 K.

The rate of temperature change was 12 degrees a day. The temperature was ramped from one temperature extreme to the other and then a few temperatures were tested again ramping in the opposite direction. It was assumed that the change in partial pressure of solvent was negligible. Bubbles, which could change size with temperature, were not present in the active region of the RF coil. The temperature was controlled with flowing nitrogen gas and the standard BTU setup for the AVANCE III spectrometer. The system was allowed to equilibrate for at least 30 minutes after a temperature change before tuning and matching, shimming, and finding the correct pulse power for the subsequent experiment.

Experimental Analysis

The PGSE experiments were Fourier transformed, noise was baseline subtracted, and signal magnitude at each gradient value was found for the spectral peak of interest. The spectrally resolved self-diffusion coefficient was then found by the Stejskal-Tanner method [44], explained in Chapter 2, which governs the signal attenuation due to diffusion during a PGSE experiment.

Two dimensional (2D) experiments, as well as spectrally resolved attenuation vs *q*-space data from select PGSE experiments, were processed by 2D inverse Laplace transform (2D ILT) software to reveal the rates of relaxation of the NMR signal, as well as the weighting/magnitudes of these rates. This ILT software uses regularized non-negative least squares; minimizing the error in the fit of the relaxation rates to the data while using a smoothness parameter, α. The smoothness parameter was chosen such that the error was minimized but only just, as less smooth distributions are prone to

'pearling'[2]. By running the α-loop, a value of 10^9 for the smoothness parameter, α, was found to correctly balance between these two effects for all experiments and was used for all ILTs. The number of points in each direction of the ILT distribution was held constant at 32. Repetition over many samples allowed for consistent features within the relaxation distributions to be identified.

Results and Discussion

Self-diffusivity of Acetone: Weight Percent Dependence

The self-diffusion coefficient measurements of acetone in HPMCAS/acetone mixtures at ambient conditions (21° C) for samples of 100% wt. acetone to 1.6% wt. acetone are presented in Fig. 4.1. Over this range, acetone diffusivity changed from that of pure acetone, $4x10^{-9}$ m^2/s, to $6x10^{-12}$ m^2/s, only slightly more that the smallest diffusions measured for HPMCAS. The diffusivities of acetone show a consistent exponential dependence on weight percent for solvent concentrations above 20% wt. acetone. A 10% wt. sample and the SDD samples, all near or below the glass transition temperatures predicted by the Fox equation (2.24), show a precipitous drop from this trend. The logarithmic dependence on weigh percent is a common characteristic of solvent self-diffusion in polymer systems [55, 64] and the drop-off at lower weight percent is predicted by the free-volume theory of Vrentas and Duda and is due to free-volume reduction causing dynamic arrest[20, 24, 34].

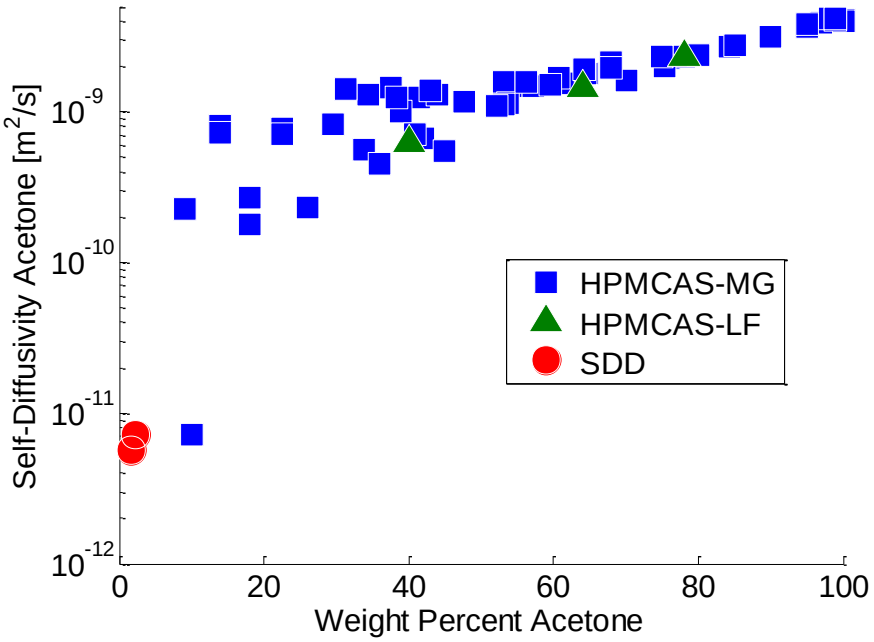

Figure 4.1. The acetone self-diffusivity measured for varied weight percent samples of HPMCAS/acetone at 21° C.

The diffusivity measurements show sample to sample repeatability at acetone content greater than roughly 60% wt. and an increasing amount of scatter, or inconsistent diffusivities between samples of the same weight percent, at lower solvent concentrations. It is believed that sample tubes have equilibrated macro-scale concentration gradients before NMR experimentation. Consecutive experiments ran with different parts of the same sample within the active region of the RF coil show consistent diffusivities, showing that concentration gradients do not exist along the length of the sample tube. In addition, relaxation populations within T_1-T_2 correlation maps (discussed below) show consistent T_2 distribution width. Because the populations' T_2 change drastically with weight percent, the breadth of these distributions in a sample containing macro-scale concentration gradients within the RF active region would cover a larger

range in T_2. All the same, re-measurements of self-diffusion on sealed samples with weight percents in the region of scatter show a decreasing trend in the diffusivity of the acetone with equilibration time. This data, presented in Fig. 4.2, shows a diffusivity range as large as the scatter in Fig. 4.1.

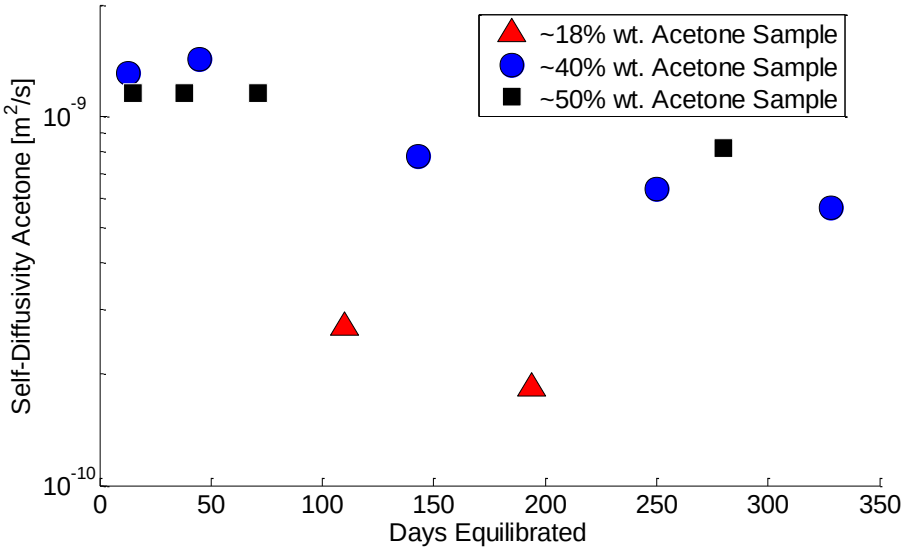

Figure 4.2. Effects of sample equilibration time on acetone self-diffusivity

One explanation for the scatter that remains is that sample aging is occurring on the micro-scale [39, 71]. Aging is characterized by a redistribution of configurational entropy and free-volume, bringing the system towards equilibrium on time scales of weeks to years due to long relaxation times. Among a landscape of amorphous micro-domains, the micro-domains sample more and more amorphous microstates and tend to stay in the more stable of microstates longer. The deceasing trend in diffusivity seen in Fig. 4.2 and the scatter in Fig. 4.1 can be explained by the system becoming more stable with time as it samples many different microstates, and the most stable microstates will have long residence times. Aging in a glassy system is characterized by a stretched

exponential, and with more data the time-dependent decrease in diffusivity could potentially be fit by such an equation[71].

A particular sample which was held at 30% wt. acetone for roughly 100 days and then slowly dried to 10% wt. over 2 months was measured to have an acetone self-diffusivity of $7.2x10^{-12}$ m^2/s. This data point in Fig. 4.1 shows a marked decrease in diffusivity from the logarithmic dependence on weight percent which held at higher acetone content. During the drying time, the system had time to find more favorable energy states through molecular rearrangement. At ambient temperature, a polymer/solvent system changes from a rubbery state to a glassy state and becomes increasingly glassy when decreasing the solvent weight percent due the change in the glass transition temperature T_g. At 21° C, the 10% weight acetone sample was predicted by the Fox equation (2.24) to be within a few degrees of T_g using a T_{g1}(acetone)=60 K [72] and a T_{g2}(HPMCAS)=393 K [72, 73]. As discussed in Chapter 2, the precipitous decrease in acetone self-diffusivity near the glass transition is consistent with the decrease in concentration of free volume limiting the diffusive mobility by dynamic arrest of the molecules [34].

It can be seen on Fig. 4.1 that the acetone self-diffusivity of the 10% wt. acetone sample was similar to values measured for the two wet SDD samples, $7.2x10^{-12}$ m^2/s and $5.7x10^{-12}$ m^2/s at 2.3% wt. and 1.6% wt. respectively. In the glassy state, the free-volume theory predicts the solvent self-diffusivity to continue dropping with increasing system glassiness, or decreasing solvent content, due to the sensitivity of self-diffusivity to free-volume changes. In analogy to the traffic jam, as the average distance between cars (the

free volume) decreases to a point that jamming or dynamic arrest occurs, the sensitivity to changes in the average distance becomes great and the speed of the traffic jam will continue to slow drastically as this average distance decreases [34]. Because the SDDs were brought from a solution >80% wt. acetone to a glassy state in seconds, this rapid quench may have prevented the system from finding its most stable conformation. The state of disequilibrium may create a higher driving force for polymer rearrangement and result in a higher self-diffusivity than in the equilibrium state. The same property which makes SDDs useful as a dosage form for drug prone to crystallization also makes the molecules more diffusively mobile relative to a slowly aged and dried sample. Additionally, if in fact the SDD is in an amorphous state of disequilibrium, aging will occur on some timescale, and PGSE NMR may be able to measure the progression.

Self-diffusivity measurements of the SDD samples had low signal to noise due to the small amount of acetone accompanying the short T_2 of the acetone present. The signal acquisition from these experiments, even with 1024 averages, showed noise on the order of the signal, however Fourier transformation revealed a single peak which had a magnitude 30 times greater than the average of the noise before baselining.

Self-diffusivity measurements were performed on three HPMCAS/acetone mixtures using a specific batch of the HPMCAS-LF grade. This was done to determine the impact of different HPMCAS grades on the NMR data generated for the MG grade primarily used in this study. HPMCAS-LF is an alternate grade of HPMCAS to the MG variety which is reported to have a slight change in its pH solubility due to differences in substituent content and its initial dry form is a finer powder than the MG grade [74].

Shown by Figure 4.1, the acetone self-diffusivities measured on HPMCAS-LF/acetone mixtures aligned with the diffusivities of HPMCAS-MG/acetone mixtures at all concentrations measured.

The acetone data was used to fit free-volume theory (FVT) parameters for the self-diffusivity equations, (2.18) and (2.19), following the procedure outlined in Yapel et al. [24]. Literature-reported values and the values found from fitting routines for parameters and combinations of parameters are shown in Table 4.1. The acetone FV parameters, $\frac{K_{11}}{\gamma}$, $K_{21} - T_{g1}$, and $\hat{V}_1^*$, were presented in Hong et al. [27] and Zielinski et al. [28] with inconsistency and led to different FTV parameter sets. Table 4.1 shows the FVT parameter sets found when using the acetone parameters reported in Hong et al. as well as those reported in Zielinski et al.[27, 28]. The values of the pre-exponential D_{01}, equal to 3.53 x10^{-8} $\frac{m^2}{s}$ with the parameters from Hong et al., or 9.83 x10^{-7} $\frac{m^2}{s}$ with the parameters from Zielinski et al., were found by linear regression of the self-diffusion data to ω_1=1, and is consistent with the reported value of Zielinski when the corresponding free-volume parameters are used [27, 28]. The Arrhenius temperature dependence of the pre-exponential factor D_{01}, shown in (2.21), was neglected as in the analysis of Yapel et al. [24]. A 3-parameter non-negative least squares regression of the acetone self-diffusivity data was used to find the remaining free-volume parameters. The function was fixed either in the limit as $\omega_1 \to 0$ to $D_1 = 6$ x10^{-15} $\frac{m^2}{s}$ (top rows), a value found for the mutual diffusivity at infinite dilution and ambient temperature from preliminary inverse gas chromatography experiments on the sorption of thin HPMCAS films [75], or to the SDD data (bottom rows).

Table 4.1. The pure acetone free volume parameters found in Hong et al. and Zielinski et al. (note the variation) [27, 28] and the resulting parameters from regression with weighting to either a sorption measurement at infinite dilution [75] or the SDD data.

Free Volume Parameter values used in fit			Note
Parameter	Hong (1994)	Zielinski (1992)	
$\frac{K_{11}}{\gamma}\left[\frac{m^3}{kg\,K}\right]$	1.86 x10^{-6}	9.83 x10^{-7}	Literature value for acetone
$K_{21}-T_{g1}\,[K]$	-53.33	-12.12	Literature value for acetone
$\hat{V}_1^*\left[\frac{m^3}{kg}\right]$	9.43 x10^{-4}	9.43 x10^{-4}	Literature value for acetone
$D_{01}\left[\frac{m^2}{s}\right]$	3.53 x10^{-8}	1.29 x10^{-7}	By linear regression of self-diffusion data to ω_1=1
Values found by 3-parameter NNLS regression of the free volume theory equation for self-diffusivity, (2.18) and (2.19) using the above parameters			The FVT was fit to self-diffusivity data while pinning to value at infinite dilution (top rows) or to SDD data (bottom rows)
$\frac{K_{12}}{\gamma}\left[\frac{m^3}{kg\,K}\right]$	3.67 x10^{-7}	2.71 x10^{-7}	
	5.56x10^{-7}	4.38x10^{-7}	
$K_{22}-T_{g2}\,[K]$	-154	-176	The glass transition temperature of HPMCAS is 393 K [73]
	-86.4	-131	
$\xi\hat{V}_2^*\left[\frac{m^3}{kg}\right]$	7.92 x10^{-4}	5.31 x10^{-4}	$\hat{V}_2^*$ was found by group contribution methods to be 6.5 x10^{-4} $\frac{m^3}{kg}$, and ξ is usually less than 1 [27, 28]
	1.05 x10^{-3}	7.42 x10^{-4}	

The physical significance of the free-volume parameters is discussed in Chapter 2. The regressed values of Table 4.1 are all within the range of the polymer FV parameter values tabulated for polymer-solvent systems [27, 28]. The tabulated value of $T_{g2} =$ 393 K [73], and the value found for $\hat{V}_2^* = 6.5\,\text{x}10^{-4}\,\frac{m^3}{kg}$ by group contribution methods [27] were used along with the regressed values for $K_{22}-T_{g2}$ and $\xi\hat{V}_2^*$ to solve for K_{22} and ξ. The ratio of solvent to polymer jumping units, ξ, is typically less than 1 [28], however this is the case only for the FV fit using Zielinski's parameters [28] and a pin at

infinite dilution. Additionally, K_{22} is greater than 200 K for all fits, whereas K_{22} values for other tabulated polymers are typically less than 100 K and not over 200 K [28].

Figure 4.3 shows the free-volume theory model for self-diffusivity, using the parameters in Table 4.1, along with the acetone self-diffusivity data. Pinning the free-volume theory fit to either $D_1 = 6 \text{ x}10^{-15} \frac{m^2}{s}$ at ω_1=0 or the SDD data, 7.2x10^{-12} m^2/s and 5.7x10^{-12} m^2/s at 2.3% wt. and 1.6% wt. respectively, was necessary to avoid the nonlinear regression from finding a single exponential fit, which more closely captured the self-diffusion behavior at acetone mass fractions greater than ω_1=0.4, but failed to predict the sharp decrease in diffusivity seen for one data point at ω_1=0.1 as well as the SDD samples. The value at ω_1=0 ($D_1 = 6 \text{ x}10^{-15} \frac{m^2}{s}$), was found from inverse gas chromatography experiments on the HPMCAS/acetone mutual diffusivity [22, 75] where theoretically $D_{mutual} = D_{1\,self}$ at infinite dilution of solvent. Using the free-volume parameter values for pure acetone, shown in Table 4.1, constrains the curves which can be obtained. The shape of the curve can have a sharper slope near ω_1=0, but this will bow the fit up and further away from the data greater than ω_1=0.4.

A future approach to find the HPMCAS free volume parameters by an alternative method, such as viscosity measurements of pure polymer melts near the glass transition [27] would allow for a free-volume theory model to be directly compared to the self-diffusivity data. The use of pure component parameters to correlate diffusivity over a wide range of temperatures and solvent content has worked for classical polymer-solvent systems such as polystyrene-ethylbenzene [76], and it will be interesting to test its validity for a polyelectrolyte with many functional groups such as HPMCAS.

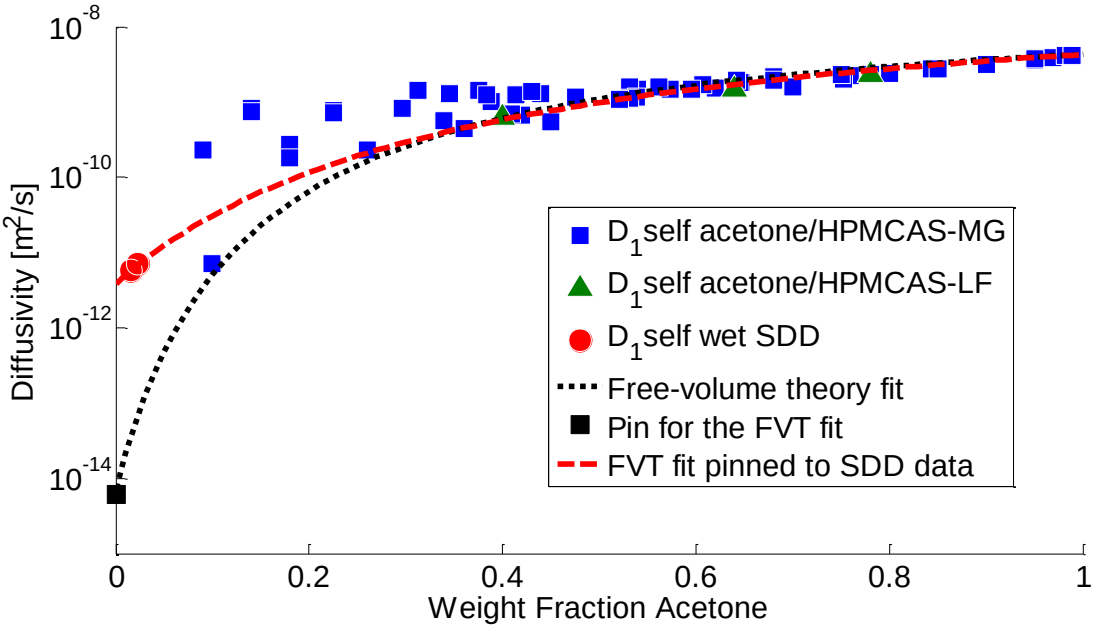

Figure 4.3. The self-diffusion data along with two possible free-volume theory fits

No fit can describe all of the data in Figure 4.3. In Figure 4.2 it was seen that self-diffusivity depended on the amount of time that the tube was capped before the PGSE NMR measurements were performed. Inconsistent measurements between samples may be due to differences in drying history varying the sample microstructure. For example, the drastically different self-diffusivities of $2.3\text{x}10^{-10}$ and $7.2\text{x}10^{-12}$ m^2/s for two separate samples at 9% wt. and 10% wt. acetone respectively may be due to heating the sample with the higher measured self-diffusivity to 40° C for roughly a month while the tube was capped and before running the PGSE experiment whereas the other tube only experienced ambient conditions. The difference in how these samples came to their measurement conditions of 10% wt. at ambient temperature, which is predicted to be near the glass transition by the Fox equation (2.24), may have caused variations in microstructure and led to drastically different acetone self-diffusivity values. With evidence that the drying

history affects the diffusivity, there appears to be a breakdown in the free-volume theory. This could be due to using a mean field theory to understand a binary system which can vary in microstructure.

Depending on whether the fit is weighted towards the mutual diffusivity value at infinite dilution or to the wet SDD samples, drastically different self-diffusion coefficients at infinite dilution can be predicted. With the goal of creating a self-diffusivity model for drying SDD droplets, it would seem that the curve fit to the self-diffusivities found for the wet SDD samples would be the correct fit for the process conditions.

It is unclear why the measurements of the acetone self-diffusivities in the wet SDD samples were three orders of magnitude different from the mutual diffusivity measurements performed in Dr. Danner's lab [75]. With inverse gas chromatography (IGC), the diffusion is measured through thin (3-10 μm) polymer films which are coated on the inside of the IGC column [22]. Differences in drying history between the HPMCAS films and the wet SDD could have resulted in varying microstructure. There may be limitations in either method (IGC or PGSE NMR) preventing the true diffusivity from being found at infinite dilution. The PGSE experiment has an inherent time (2τ) that transverse magnetization must last through in order to be observed. Because T_2 governs the decay of transverse magnetization, if the acetone within the SDD has multiple inherent T_2 values and these T_2 values are near the τ time, then the diffusivity will be weighted towards the larger T_2 population of acetone. It will be seen in later sections that the longest T_2 in the wet SDDs is roughly a millisecond and that there is

exchange (mixing) occurring on a millisecond timescale between this population and a population of T_2=200 μs. With τ = 2 ms, T_2 weighting towards the self-diffusivity of the population of T_2 = 1 ms is occurring. It is likely that the diffusivities of these populations are different, as the molecular rotational mobility, which T_2 is dependent on due to it averaging out the dephasing of transverse magnetization caused by dipolar interactions, often correlates to translational diffusion. If the self-diffusivity of the population of longer T_2 is greater than that of the population of shorter T_2, then the self-diffusivity measured by PGSE will be larger than the actual acetone self-diffusivity.

Chapter 2 gives the development of the equation for mutual diffusivity, (2.23), using the free-volume theory for self-diffusivity. Neglecting the Arrhenius temperature dependence of the pre-exponential factor D_{01}, (2.20), and approximating volume fractions as being equal to the weight fractions, the resulting equation for mutual diffusivity is:

$$D = 3.53 \times 10^{-8}(1-\omega_1)^2(1-2\chi\omega_1) \tag{4.1}$$
$$exp\left(\frac{-(9.43\ \times 10^{-4}\omega_1 + 1.05\ \times 10^{-3}\omega_2)}{1.86 \times 10^{-6}\omega_1(-53.33-T) + 5.56 \times 10^{-7}\omega_2(-86.4-T)}\right)$$

The Flory-Huggins interaction parameter, χ, is the only unknown, and in practice is a function of the solvent content. Tester and Model [26] state that χ is typically between 0.1 and 0.9 for polymer-solvent systems, however for the gelatin-water system studied by Yapel et al., χ is near -2.6 at 1% vol. solvent, increases to 0.6 by 30% vol. solvent, and decreases slightly, to 0.4, between 30% and 99% vol. solvent [24]. With no data on χ for HPMCAS/acetone available, (4.1) is plotted using a constant χ of 0.1 and 0.9 alongside

the self-diffusivity data in Figure 4.4 to demonstrate the χ dependence of the mutual diffusivity.

The mutual diffusivity curves align with the acetone self-diffusivity at infinite dilution, as expected, and are less than the self-diffusivity at all acetone mass fractions greater than zero. Note that negative χ values would predict an increase in mutual diffusivity from the self-diffusivity. The mutual diffusivity curves counter-intuitively drop off with increasing solvent content, and become physically unreasonable. The mutual diffusivity at infinite solvation ($\omega_1 \rightarrow 1$ and $\omega_2 \rightarrow 0$) must become equal to the self-diffusivity of the polymer, which will be seen in the next section to be 10^{-10} m^2/s. The reason for this discrepancy is that the closed form relation between the self-diffusivity and the mutual diffusivity (2.21) involves only the self-diffusivity of the solvent. However, as the SDDs have initial solvent contents less than 85% wt., the droplet drying model will not require knowledge of the mutual diffusivity between 85% wt. and 100% wt. solvent where the closed form relation between mutual and self-diffusion breaks down. Differences between the predicted mutual diffusivities using a constant χ of 0.1 versus 0.9 show that χ clearly affects the predicted mutual diffusivity. Following Yapel et al. [24], χ should be found over the solvent contents of interest in order to correctly predict the mutual diffusivity.

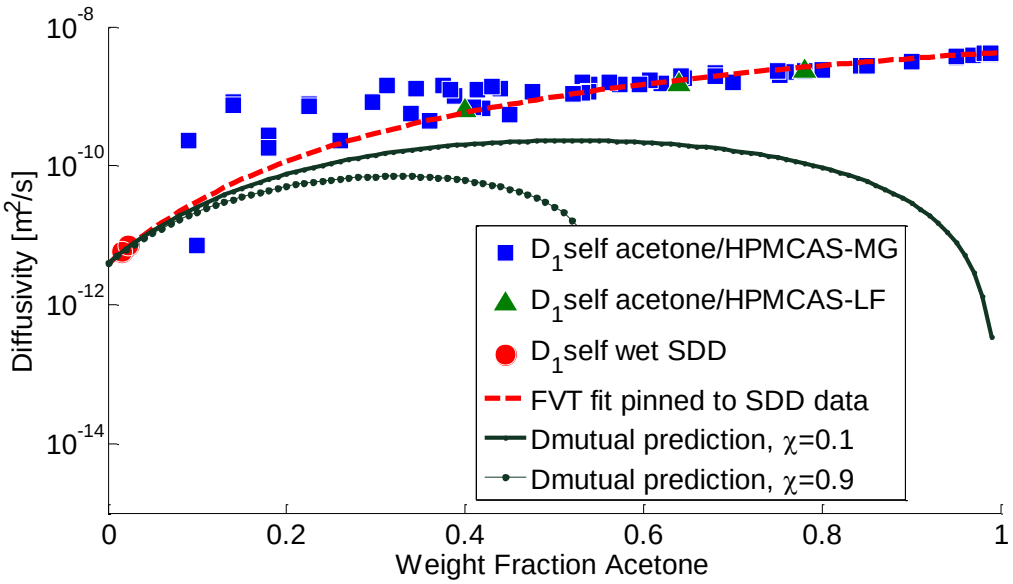

Figure 4.4. The mutual diffusivity predictions from (4.1), when using the FVT fit pinned to the SDD data, alongside the self-diffusivity data.

Self-Diffusivity of HPMCAS:
Weight Percent Dependence

Upon attenuation of the acetone NMR signal by application of gradients $g > 1$ T/m, Fourier transforms of the echoes showed the HPMCAS spectra. A typical spectrum is shown in Figure 4.5a. Broad peaks and chemical shifts are common among biopolymers, but no effort was made to match the spectral peaks to intermolecular proton locations. Such analysis would be better undertaken on a high resolution liquids NMR spectrometer since the goodness of shims on the 250 MHz spectrometer are limited by the wide-bore configuration, leading to broader spectral peaks. Figure 4.5b. shows the HPMCAS spectrum of a 90% wt. acetone mixture from a high-resolution spectrometer after zooming in on the polymer peaks not covered by the acetone peak. The high-resolution 300 MHz narrow bore spectrometer is commonly used for spectroscopy, whereas the 250 MHz wide bore spectrometer is not. Figure 4.5 shows comparable

chemical shifts between the polymer peaks in the spectra found by these two methods and gives confidence in their identification as HPMCAS peaks.

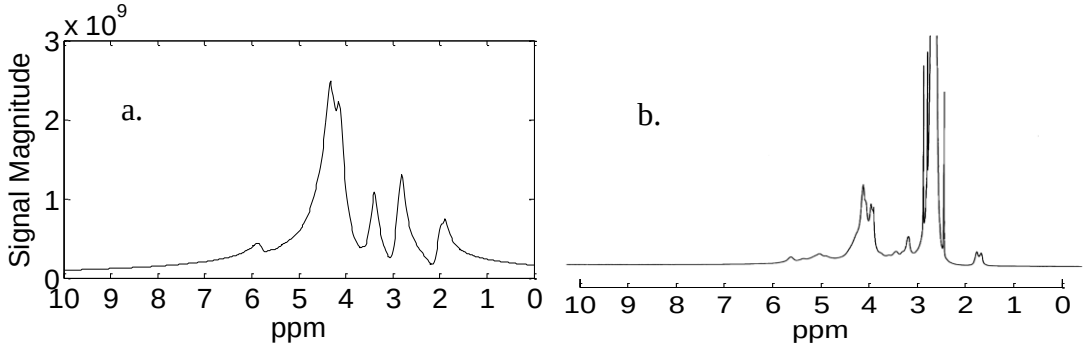

Figure 4.5. The HPMCAS spectra from a PGSE experiment upon attenuation of the acetone signal using a 250 MHz wide bore spectrometer (a.) and from a high-resolution 300 MHz narrow bore spectrometer when zooming in on the HPMCAS peaks and cropping the top of the acetone peak, at 2.9 ppm (b.).

Self-diffusion of HPMCAS was measured with the PGSE technique using displacement observation time $\Delta = 50$ ms. On this time-scale, the diffusive length scale of molecules with a self-diffusion coefficient of 10^{-12} m^2/s, the order of magnitude for the diffusion coefficient of HPMCAS in concentrated polymer samples, is $l_D \sim 300$ nm.

Based on the HPMCAS molecular structure and HPMCAS molecular weight of 180 kDa, found for similar batches by Bend Research Inc., a fair estimate on the number of mers per polymer is $N \approx 1000$. The average radius of gyration of the polymer molecule scales by $R_g \approx N^v b$, where v depends on solvent quality and $v = 3/5$ from the self-avoiding walk model, or with the effects of excluded volume, and b is the length of a mer [77]. Using $b \approx 1$ nm for HPMCAS, $R_g \approx 60$ nm with the self-avoiding walk model though R_g is highly dependent on v.

Since the diffusive length scale sampled in 50 ms is larger than the theoretical R_g of an HPMCAS molecule, it is expected that PGSE experiments observe polymer molecules that are undergoing diffusive motion rather than sub-diffusive motion as indicated by the reptation model (2.17) for times $\Delta > \tau_{rep}$. The mean squared displacement of polymer molecules undergoing diffusive motion will scale linearly with the observation time, $\langle Z^2 \rangle \sim t$ for times $\Delta > \tau_{rep}$, whereas the mean squared displacement of polymer molecules undergoing sub-diffusive motion will scale with time by a power n less than 1, $\langle Z^2 \rangle \sim t^n$, for regimes $\Delta < \tau_{rep}$ (see Eqn. (2.17)). The scaling powers predicted by theory for reptation, Rouse motion, and Zimm motion are discussed in the Polymer Dynamics section of Chapter 2.

As proof that diffusive regime motion of the HPMCAS polymer molecules occurs on the $\Delta = 50$ ms timescale, Figure 4.6 shows that the mean squared displacement of HPMCAS in five samples between 60% wt. and 20% wt. acetone scaled roughly linearly with time for observation times between 50 ms and 500 ms. Self-diffusion coefficients determined by integration over different spectrally resolved polymer peaks showed an average of less than 4% difference. Because hydrogens on acetone are covalently bondend, there is no protone exchange between acetone and polymer molecules and self-diffusion measurements of the polymer yield center of mass displacements of molecules.

The HPMCAS self-diffusion coefficient dependence on weight percent acetone, shown in Fig. 4.7, varied from 10^{-10} m^2/s for 99% wt. acetone to 10^{-12} m^2/s for some samples below 50% wt. acetone. The NMR signal from the HPMCAS became

undetectable with PGSE for samples of roughly 10% wt. acetone and less due to the T_2 of the HPMCAS shifting to less than $\tau = 2.5$ ms, as will be shown below.

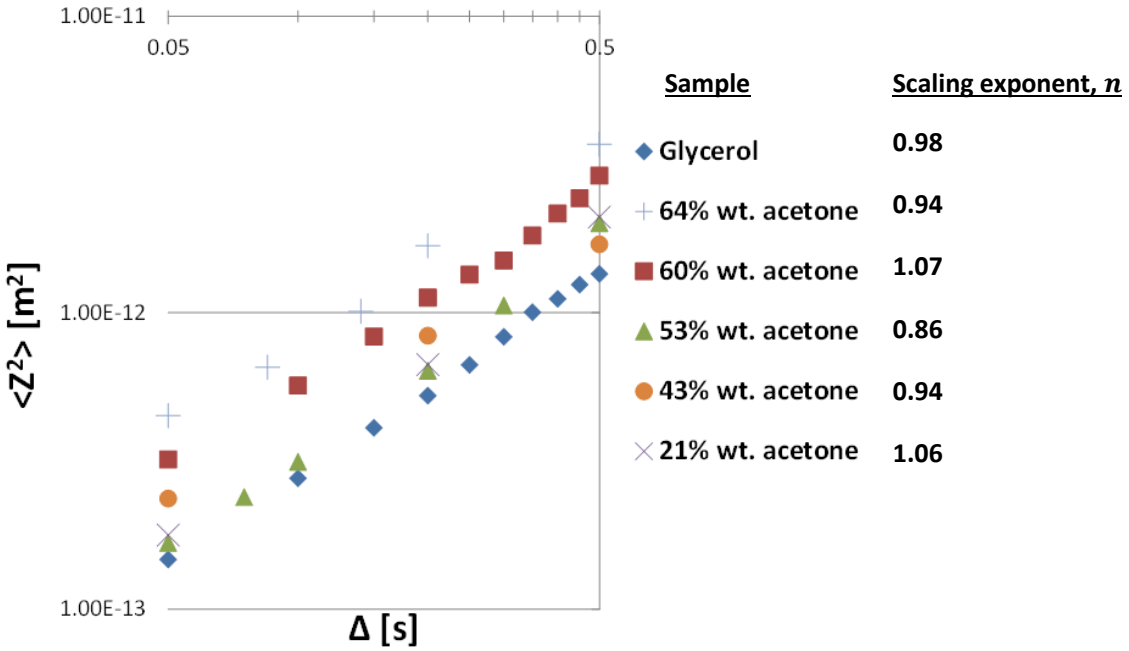

Figure 4.6. The scaling of HPMCAS polymer or pure glycerol mean squared displacement with observation time. The scaling n exponent is from fits to the form: $\langle Z^2 \rangle = Ct^n$, where $n = 1$ for diffusive motion.

The data in Figure 4.7 indicates that there are critical concentrations where scaling of diffusivity with acetone content changes. These critical weight percents, which should be linearly related to polymer or solvent concentration assuming negligible dependence of mixture density on component weight percent, are deemed to be roughly 90% wt. acetone and 50% wt. acetone. Between 99% wt. and 90% wt. acetone, HPMCAS self-diffusivity scales strongly with weight percent, decreasing nearly one order of magnitude over just a 9% wt. change. The HPMCAS self-diffusivity scales less strongly between 90% wt. and 50% wt. acetone as self-diffusivity decreased an order of

magnitude over a 40% wt. change. Between 10% wt. and 50% wt. acetone the weight percent dependence of HPMCAS self-diffusivity is negligible and unobservable when compared to the scatter of the measurements.

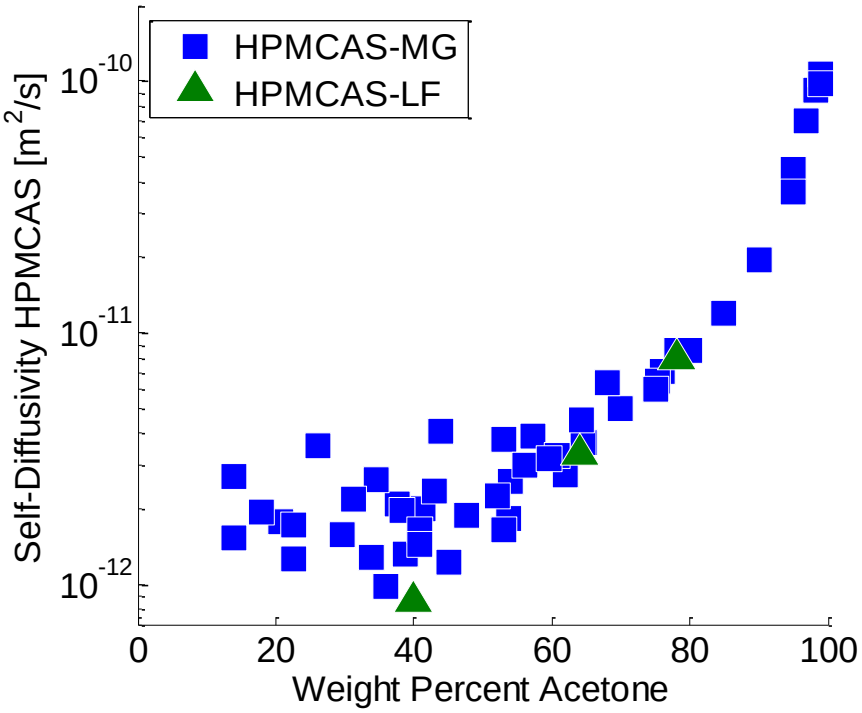

Figure 4.7. Self-diffusivity measurements of HPMCAS on mixtures of varying weight percent acetone in either the MG or the LF grade of HPMCAS.

In a review of polymer diffusion models my Mazaro and Zhu [55], particular models which take into account hydrodynamic interactions are discussed. The form of these models are $D_{self} = D_0 \exp(\alpha * x^v)$, where the polymer concentration, c, is replaced with the weight percent of solvent, x, to be applicable in the current situation. In many of the hydrodynamic models listed, α is inversely related to the hydrodynamic radius of the diffusing polymer and v varies between values of 0.5, 0.75, and 1. A value greater than 1, which would be needed to fit the HPMCAS self-diffusivity over a concentration range

greater than those split up by the critical concentrations, is not predicted. The hydrodynamic model equation was fit to the weight percent acetone regimes $90\%\ wt. < x < 99\%\ wt.$ and $50\%\ wt. < x < 90\%\ wt.$ A linear fit using $v = 1$ was used in order to solve for values of D_0, which were used in subsequent non-negative least squares fit where v was not specified. Three-parameter NNLS fits without specifying D_0 did not converge. The regressed values for D_0, α, and v are shown in Table 4.2.

Table 4.2. Hydrodynamic model parameters for HPMCAS self-diffusivity

Weight % acetone (x)	Hydrodynamic model: $D_{2\,self} = D_0 \exp(\alpha * x^v)\ \left[\frac{m^2}{s}\right]$		
	D_0	α	v
$90\%\ wt. < x < 99\%\ wt.$	1.51×10^{-21}	0.392	0.904
$50\%\ wt. < x < 90\%\ wt.$	1.92×10^{-13}	0.0152	1.27

In table 4.2 it is seen that α is considerably different between the two weight percent regimes which is expected due to the change in scaling of diffusivity with weight percent. The value of $v = 0.904$ for the weight percent acetone range $90\%\ wt. < x < 99\%\ wt.$ is between theoretical model values of $v = 0.75$ and $v = 1$, where $v = 1$ was proposed by work of Freed and Edwards [78] for undiluted polymer chains in solution in the absence of entanglements, and this result was re-examined by de Gennes [67, 79] who found that $v = 0.75$ for long flexible chains in good solvents [55]. From this, $v = 0.904$ seems consistent with theory of unentangled polymers not in the dilute polymer regime and it is proposed that $90\%\ wt. < x < 99\%\ wt.$ is roughly the semidilute regime of HPMCAS/acetone solutions at ambient conditions. The change in scaling with concentration, seen through the considerable difference in α, and the value of $v = 1.27$

being inconsistent with theory show that $50\%\ wt. < x < 90\%\ wt.$ acetone is a different polymer regime and that polymer self-diffusivity in this regime cannot be described by hydrodynamic theories.

The reptation plus scaling model for the self-diffusion of polymers in solution [67], discussed within Mazaro and Zhu [55], was also applied to the acetone weight percent regimes, $90\%\ wt. < x < 99\%\ wt.$ and $50\%\ wt. < x < 90\%\ wt.$ This simple power law scaling of the form $D_{self} = b * x^m$ predicts $m = 1.75$ for polymer in good solvents and $m = 3$ for polymer in θ solvents. The reptation plus scaling model parameter values regressed from the two regimes are shown in Table 4.3

Table 4.3. Reptation plus scaling model parameters for HPMCAS self-diffusivity

Weight % acetone (x)	Reptation plus scaling model: $D_{2\ self} = b * x^m \ \left[\frac{m^2}{s}\right]$	
	b	m
$90 < x < 99$	9.40	24.6
$50 < x < 90$	2.42×10^{-17}	2.93

The values regressed for the power law exponent are $m = 24.6$ for $90\%\ wt. < x < 99\%\ wt.$ acetone and $m = 2.93$ for $50\%\ wt. < x < 90\%\ wt.$ The power law exponent of the 90% wt. to 99% wt. acetone regime doesn't fit theoretical values of m in the reptation plus scaling model and may indicate that the polymers in this regime are unentangled and not reptating which is consistent with this being the semidilute regime. The power law exponent of the 50% wt. to 90% wt. acetone regime is close to 3, indicating that this regime fits the reptation plus scaling model and that the HPMCAS in this regime is acting as if in a θ solvent, a solvent in which each polymer molecule can be

modeled as a random walk of correlation blobs ideal [77]. The closeness of the regressed value of $m = 2.93$ to the theoretical value $m = 3$ for reptating polymers in a θ solvent indicates that this is the entangled polymer regime.

The progression of semidilute to entangled with the removal of solvent is consistent with polymer theory [14]. The polymer concentration which separates the entangled from the unentangled semidilute polymer regime is known as the entanglement concentration c_e. The entanglement concentration is roughly the polymer concentration corresponding to 90% wt. acetone, at which the density is unknown at the time of publication. The entanglement concentration is anticipated to be near this weight percent due to the decrease in polymer self-diffusivity from the measurement of 1.07 x 10^{-10} m^2/s at 98.9% wt. to 1.96 x 10^{-11} m^2/s at 90% wt. At c_e the solution viscosity should be roughly an order of magnitude higher than the pure solvent viscosity [63], and viscosity is inversely related to self-diffusivity by the Zimm model (2.12) which is based on the Stokes-Einstein-Sutherland Equation (2.8). This relation requires that the diffusing polymer pervaded volume is independent of concentration since it is for an isolated sphere of radius R, but estimation provides physical insight. Using R = 60 nm, the previously estimated radius of gyration using a self-avoiding walk model, viscosity estimates are $1.3 \times 10^{-4}\ \frac{kg}{m\ s}$ at 98.9% wt. acetone, and $6.8 \times 10^{-4}\ \frac{kg}{m\ s}$ at 90% wt. acetone. The viscosity of pure acetone at ambient conditions is $3.3 \times 10^{-4}\ \frac{kg}{m\ s}$, showing the viscosity estimate at 98.9% wt. acetone to be incorrect, as it cannot be less than the pure solvent. Regardless, the estimated viscosity increased nearly an order of magnitude

between 98.9% wt. and 90% wt. acetone, validating that the change in HPMCAS self-diffusivity scaling that occurs at 90% wt. acetone is the entanglement concentration.

The hydrodynamic model fit of the proposed semidilute regime, 90% wt. to 99% wt. acetone, from Table 4.2 as well as the reptation plus scaling model fit of the proposed entangled regime, 50% wt. to 90% wt. acetone, from Table 4.3 are plotted log-log over their relevant weight percents along with the HPMCAS self-diffusivity data in Figure 4.8.

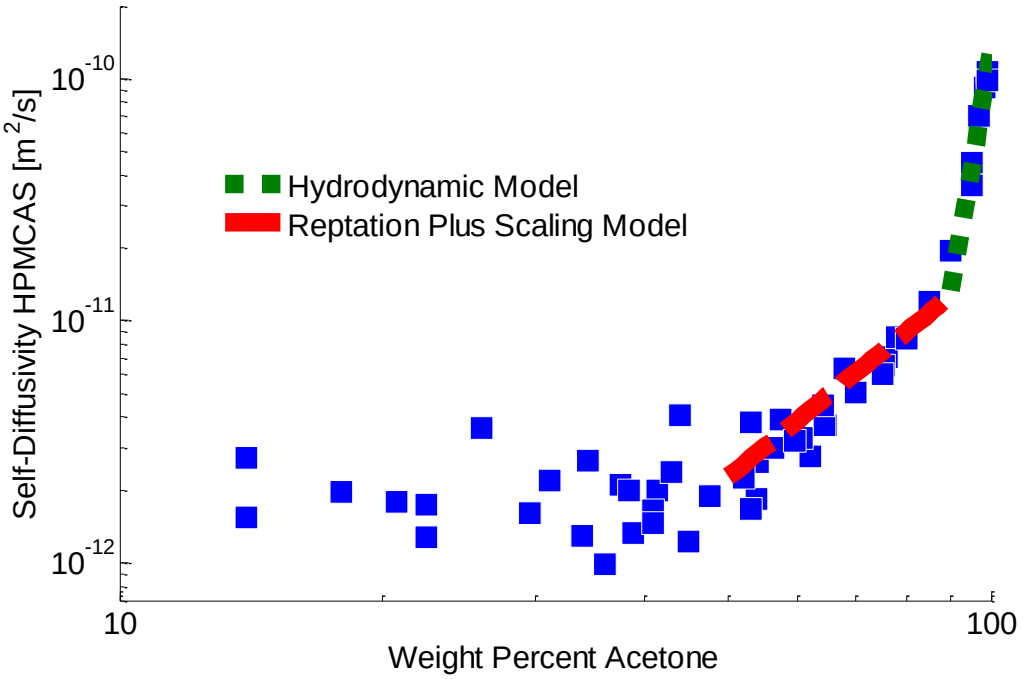

Figure 4.8. HPMCAS self-diffusivity data fit to the Hydrodynamic model over the 90% to 99% wt. acetone semidilute regime and to the reptation plus scaling model over the 50% to 90% wt. acetone entangled regime and plotted log-log.

Additional evidence of a critical concentration was revealed by the inverse Laplace transform (ILT) of the signal attenuation vs. *q*-space data. The ILT, discussed in Chapter 2, finds a distribution of diffusion coefficients and the weightings or magnitudes of populations with those diffusion coefficients necessary to describe the signal

attenuation. The log of signal attenuation vs $\gamma^2 g^2 \delta^2 (\Delta - \delta/3)$ or $q^2(\Delta - \delta/3)$ of experiments that used 64 or 128 *q*-points to give additional resolution to diffusivities when transformed are shown in Figure 4.9.

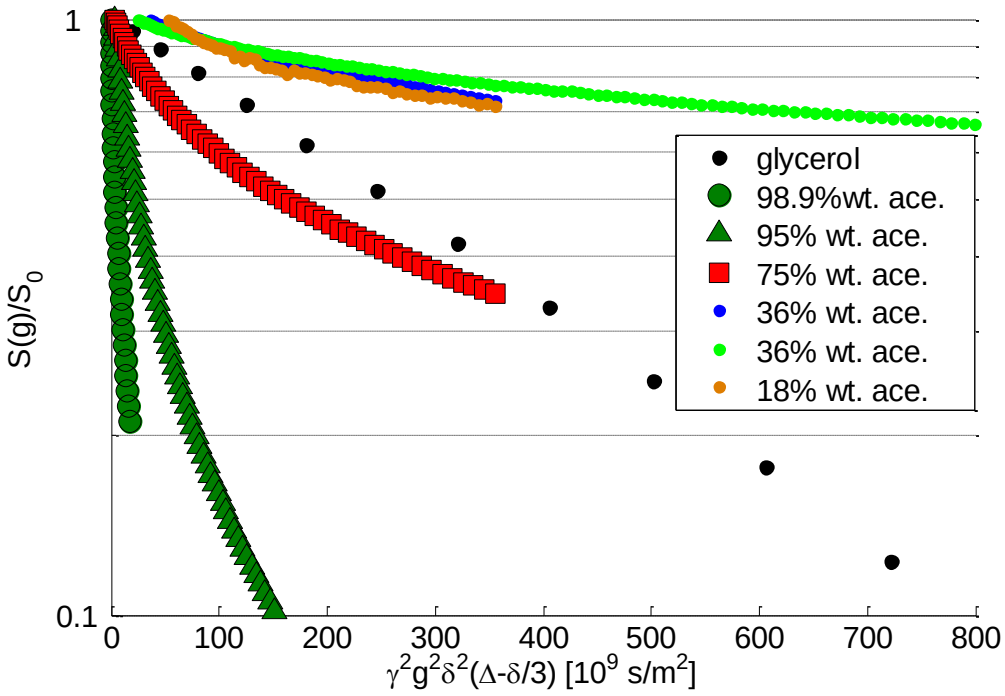

Figure 4.9. Stejskal-Tanner plots of the 64 and 128 gradient point experiments used for ILT. The Stejskal-Tanner plot of glycerol, which decays by a single exponential, is displayed to convince that the multiexponential behavior of the HPMCAS is not due to uncalibrated equipment.

Glycerol attenuates with a single exponential, seen by the linearity on the semi-log plot, meaning that a single diffusivity is present, as expected. The spectrally resolved HPMCAS signal attenuation is normalized such that the first point, which occurs at some value of q^2 that attenuates all of the acetone signal, is $M/M_0=1$. The HPMCAS signal attenuation is multiexponential at all concentrations, which indicated that the ILT will provide multiple diffusion populations.

It is apparent from Figure 4.9 that the attenuation range was not consistent between these experiments. Various portions of the entire multiexponential signal attenuation range are weighted towards different diffusion coefficients. Signal attenuation in the low *q*-space range is dominated by the faster diffusivities and signal attenuation in the high *q*-space range, after the signal from faster diffusing populations has attenuated, is dominated by the slower diffusivities.

The amount of attenuation of HPMCAS signal from the 36% and 18% wt. acetone samples was limited by the maximum gradient strength of the Diff30=17.8 T/m and the decreased signal to noise as the signal attenuated. The amount of attainable HPMCAS signal at 36% and 18% wt. acetone was low due to T_2 relaxation. The diffusion distribution of the 36% wt. acetone sample was nearly identical between a max $q^2(\Delta-\delta/3)$=3.6x10^{-11} s/m^2 with 64 gradient steps and a max $q^2(\Delta-\delta/3)$=8.0x10^{-11} s/m^2 with 128 gradient steps. The low *q*-rage with 64 gradient steps, which attenuated 30% of the HPMCAS signal for the 18% wt. and 36% wt. acetone samples, was used for subsequent samples less than 50% wt. acetone.

The HPMCAS signal attenuation rage of the 75% wt., the 95% wt., and the 98.9% wt. acetone samples were not limited by gradient strength or signal to noise, and the attenuation ranges varied due to incomplete knowledge of the diffusivities before experimentation. Ideally for comparison purposes, all experiments would have the same attenuation range. With the experiments analyzed by the Stejskal-Tanner method, the attenuation range was tailored to between 10-30% by removing *q*-points from the front end or back end of the experiment. This was not done for the experiments which the ILT

was used to analyze due to the loss of points leading to loss of information on the distribution of diffusions. Because consistent features were observed between the resulting diffusion distributions from the experiments in Figure 4.9, the experiments were deemed adequate for comparison purposes even though the attenuation ranges were inconsistent.

The ILT can ‘pearl’ a single broad distribution into multiple peaks, which may correctly or erroneously show the presence of multiple distinct populations [80]. Caution will be taken to not falsely interpret the diffusion distributions. Figure 4.10 shows the HPMCAS diffusivity distributions, found by inverse Laplace transform of the attenuation vs. *q*-space data seen in in Figure 4.9.

The HPMCAS diffusivity of 98.9% wt. acetone shows a single peak around 10^{-10} m^2/s, which is consistent with the Stejskal-Tanner measured diffusivity. There is some breadth to this peak, which is expected from the log of signal attenuation not showing complete q^2 dependence in Figure 4.9.

A polymer molecule in the dilute regime will experience a large enough number of random acetone-polymer interactions during the 50 ms observation time such that, as an Ornstein-Uhlenbeck process, the long-time limit of (2.7) is observed. In the dilute regime, polymer molecules interact negligibly with each other, whereas in the semi-dilute, in which 98.9% wt. is hypothesized to be, polymer-polymer interactions become important. A polymer molecule in the semi-dilute regime may not experience a sufficient number of polymer-polymer interactions to make the propagator completely Gaussian. This may be an added cause of the non-q^2 dependence of the signal attenuation. The 95%

wt. distribution shows a single peak with a breadth covering almost the entire range of the 99% wt. distribution and extending towards slower diffusivities and a slower peak value, to $3x10^{-11}$ m^2/s. The increased range in diffusivity indicates increased polymer-polymer interactions present in the semidilute regime.

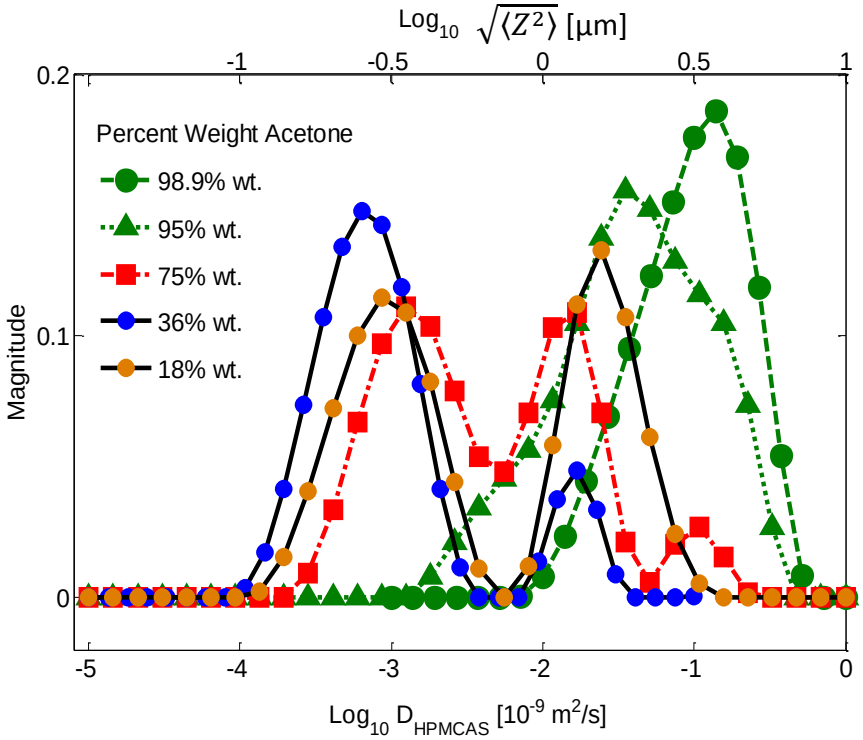

Figure 4.10. The HPMCAS self-diffusion distributions at various concentrations. The bottom axis shows log base 10 of the diffusivity plus 9, such that -1 on the axis corresponds to 10^{-10} m^2/s. The top axis shows the HPMCAS diffusive length scale based on the relation $\langle Z^2 \rangle = 2D\Delta$. The green lines and symbols are mixtures hypothesized to be in the semidilute regime, the red is for a mixture in the entangled regime, and the black lines with symbols represent mixtures in the regime of sample spanning network.

The diffusivity distribution of the 75% wt. acetone sample shows multiple diffusive populations. In the concentrated regime, polymer entanglements can form. The change from one diffusive population in the semi-dilute regime to more than one in the concentrated regime is consistent with the formation of polymer structures through

entanglements in the concentrated regime. The population with the greatest diffusivity, with a peak magnitude of 10^{-10} m^2/s, is similar in value to the peak magnitudes of the diffusive populations of the 98.9% wt. and the 95% wt. acetone mixtures. This may be polymer molecules which are diffusing as if they were in the semidilute regime; they are unentangled. The 36% wt. and 18% wt. acetone samples each show two peaks which are of roughly the same diffusivity. Additionally, these two peaks overlap with the two peaks of largest magnitude in the 75% wt. distribution.

Mixtures of weight percent higher than 90% wt. acetone show only a single HPMCAS diffusion population, while mixtures of weight percent less than 90% wt. acetone show multiple populations of HPMCAS diffusivity. This may be due to the transition in types and timescales of polymer-polymer interaction between the semidilute and concentrated polymer regimes. The distinct populations indicate the ILT of PGSE experiments of polymer mixtures provides a one-shot method of determining the concentration regime (semidilute or entangled) of a polymer/solvent mixture.

A PGSE experiment with an observation time of 500 ms was run on the 75% wt. acetone sample to compare with the sample's diffusivity distribution at 50 ms. These two distributions, shown in Figure 4.11, are nearly identical. If these populations are truly distinct and not erroneously pearled by the ILT, then there are no HPMCAS molecules sampling between these two states or domains during the 500 ms observation time. If there was diffusive sampling between these populations, then at 500 ms there would be blending between the diffusion populations seen at 50 ms.

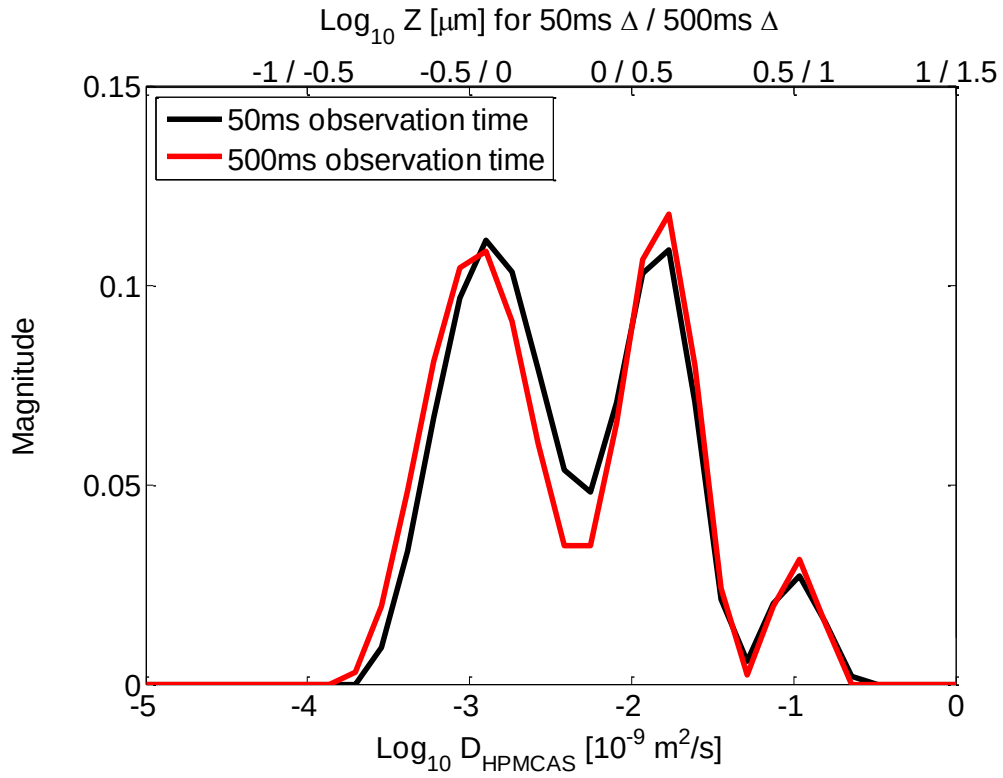

Figure 4.11. The HPMCAS diffusion distributions of 75% wt. acetone at an observation time, Δ, of 50 ms and 500 ms. The top axis shows the diffusive length scales for the two observation times.

HPMCAS molecules can entangle through excluded volume interactions or electrostatic forces. Associated with these entanglements are correlation times over which the molecules are attached to one another. Entanglements in de Gennes' model restrict an individual polymer molecule to a tube along its length created by the surrounding polymer matrix [17]. These entanglements are dependent on polymer relaxation times, and different confining tubes could form and dissipate many times over the observation time of diffusion resulting in the normal linear in time diffusion observed for $\Delta > \tau_{rep}$ (Fig. 4.6). In regards to gelation and network formation, sub-diffusion could be observed on timescales where the polymer molecule felt the shackling effects of a sample spanning

network that was chemically crosslinked or gelled. A similar example is restricted diffusion of water in a pore. Varying the observation time longer than the water needs to diffusively sample the pore, the mean squared displacement becomes constant [2]. However, in a physical gel, such as the HPMCAS mixtures, where crosslinks are not permanent, this is not necessarily true. Electrostatic interactions between polyelectrolyte molecules such as HPMCAS can be greater than the k_BT energy associated with thermal fluctuations and longer lived than the observation time, thus creating a transient network [81]. Rouse motion models the polymer molecule as a chain of beads attached together by springs [16]. Thermal energy which moves a bead is dampened by the spring on either side and imparts energy onto the neighboring beads. It is a straightforward step to imagine that multiple crosslinked polymers could be modeled in the same way. If crosslinks lasted longer than the observation time, and the diffusive length scale was shorter than the end-to end distance of the two (or more) crosslinked polymers, then Rouse motion would be observable through the sub-diffusive scaling of mean squared displacement with observation time, indicating that $\Delta < \tau_{rep}$ for the Δ times probed [14]. As shown in Figure 4.6, no evidence of sub-diffusion of HPMCAS was found in this research between $50 < \Delta < 500$ ms. One HPMCAS diffusion population turning to multiple with the transition from semidilute to concentrated mixtures in Figure 4.10 indicates entanglements. The shortest diffusion population may be due to electrostatic interactions between HPMCAS molecules, lasting longer than the observation time, increasing the effective size of the diffusing particle. The diffusion populations of the 75% wt. acetone mixture seen in in Figure 4.11 not blending together with an increasing

observation time reinforces this hypothesis, and means that the correlation times of entanglements, likely through electrostatic interactions, are longer than 500 ms. The diffusive length scale (top axis of Figure 4.10) of the slowest diffusivity peak at 50 ms is 300 nanometers for the 75% wt. acetone sample and decreased to 200 nm for the 36% wt. acetone sample. Rouse motion disappears on time scales greater than the Rouse time, τ_R, when the diffusive length scale becomes greater than the networked structure [14]. The polymer structures connected by long lasting entanglements are necessarily smaller than the diffusive length scale for Rouse motion to not be observed. Therefore, these structures are a maximum of 200 nm in size. The faster diffusivity peaks in Figure 4.11, in order to diffuse faster, are related to smaller structures than this.

An imaging technique capable of discerning multiple phases could be helpful. However, all the samples are transparent, meaning that phases larger than the wavelength of light do not exist. Visible light has a wavelength of 400-600 nm, and because the diffusive populations in Figure 4.10 sample length scales greater than this, discrete phases of varying density cannot be the primary reason for the populations.

In mixtures of less than 50% wt. acetone, the second critical concentration in Figure 4.8, HPMCAS self-diffusivity analyzed by the Stejskal-Tanner method no longer trended with concentration. Removing additional acetone from a 50% wt. sample didn't affect the polymer translational mobility. The HPMCAS diffusivity distributions of the 36% wt. and 18% wt. acetone mixtures, in Figure 4.10, show two similar population peak diffusivities. The polymer-polymer interactions at these two concentrations are similar when observed over 50 ms. The density of polymer molecules increasing would increase

the number of topological constraints on each polymer molecule. Figure 4.10 along with the HPMCAS self-diffusivity plateau in Figure 4.7 show that increasing the density of topological constraints at a certain point no longer affects the ability of a polymer molecule to diffuse. Another hypothesis is the presence of two different phases and that upon removal of acetone from 50% wt. acetone, the density of polymer in the polymer rich phase is no longer changing, only the phase volume fraction changes.

Shapiro discusses the molecular characteristics of organogels, which are gel systems with an organic solvent [82]. Entangled polymer chains stabilized by weak molecular forces including hydrogen bonding, van der Waals forces, and π-π stacking immobilize the organic solvent and form a three-dimensional network. One characteristic of gelators, which HPMCAS also has, is long alkyl side chains. Many factors can counter these forces in the self-assembly including steric effects, rigidity, and polarity. Through transmission electron microscopy (TEM), a common organogel network structure has been seen independent of the gelator. This structure is an interconnected, sponge-like network of gel fibers hundreds of nanometers in diameter surrounded by a solvent rich phase [82]. The term "weak" gel-like system is given to materials showing liquid-like viscoelastic behavior and made up of a transient network (physical crosslinks allow for the structure to change in time) [82].

The multiple HPMCAS diffusive populations give evidence for physical crosslinks which occur after the entanglement concentration. The similar diffusivity distributions at 50 and 500 ms for the 75% wt. solvent, in Figure 4.11, give evidence for long-lasting crosslinks. HPMCAS shares some characteristics with a "weak" gel-like

system. Oscillatory experiments on gel networks will show the storage modulus, G', higher than the loss modulus, G'', at all frequencies[14]. Through oscillatory experiments performed in house, HPMCAS/acetone mixtures have never been shown to meet this criterion of a network.

Brand et al. showed that the minimum in the ratio between the self-diffusivity of the gelator and the self-diffusivity of the solvent at variable temperatures could be used as a measure of the gelation temperature of a thermal gelling system [83]. This may serve as a marker for the onset of network formation with changing solvent weight percent. The plot of this for the acetone/HPMCAS system is shown in Figure 4.12**.** The ratio between the HPMCAS and acetone self-diffusivity plateaus for concentrations less than 60% wt. acetone, but does not show a clear minimum.

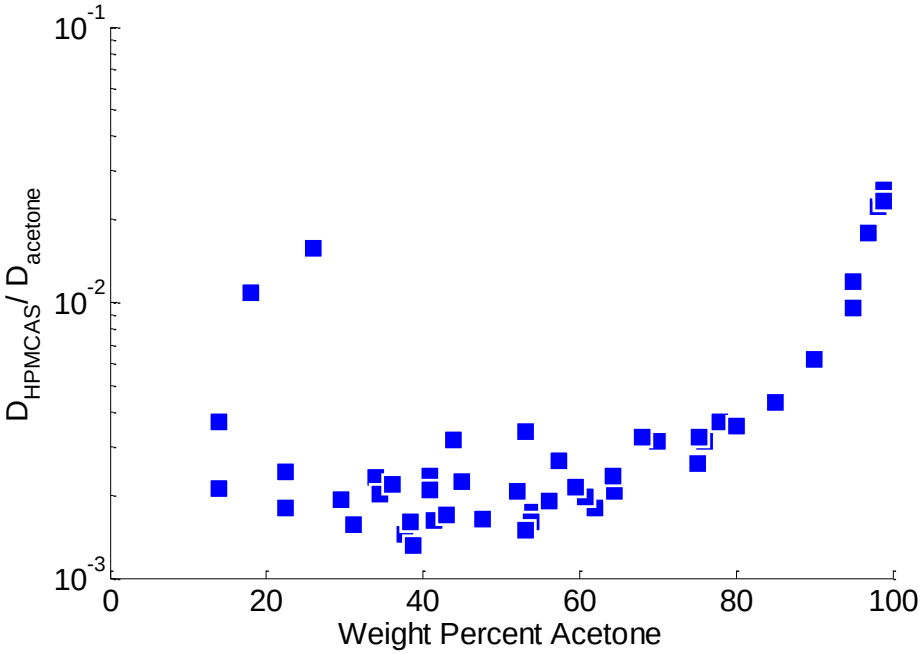

Figure 4.12. The ratio of HPMCAS to acetone self-diffusivity in mixtures of varying weight percent.

An interesting point is that the observed characteristics are advantageous towards its function in pharmaceutical applications. It is necessary that acetone/HPMCAS/drug mixtures flow at 80-90% wt. solvent so that it can be pumped through atomizers and produce small (10-100 μm) droplets. However, in-vitro testing of the dissolution of HPMCAS/Drug SDDs in solutions simulating the duodenal and intestinal contents show the primary structure formed to be amorphous nanostructures (20-300 nm) with fast exchange of drug between the dissolved state and can thus buffer the solution against precipitate formation[48]. Note that this is a completely different system from acetone/HPMCAS, with not only a water-based solvent and low pH but also the presence of amphiphilic, micelle forming molecules. Between these two states (spray drying and dissolution in the gut), HPMCAS SDDs show excellent physical stability, in part due to the weak molecular forces between polymer molecules which immobilize the drug.

As with the acetone diffusivity measurements, the non-repeatability of HPMCAS self-diffusivity measured on samples below 50% wt. can be explained in part by aging. The HPMCAS self-diffusivity on select samples as a function of the equilibration time, or time capped, is shown in Figure 4.13.

From a thermodynamic perspective, as the system becomes more stable, the diffusivities decrease. A kinetic perspective is somewhat harder to grasp. It was stated earlier that the polymer concentration has no effect on diffusivity of samples less than 50% wt. acetone. This would seem to equate to the number of entanglements having no effect on diffusivities of polymers that are entangled in the sample spanning network. With time, more polymers could join the sample spanning network, causing a shift

towards slower diffusivities. Additionally, as the acetone solvates the polymer in increasingly stable arrangements with time, the amount of bombardment from acetone would decrease, lowering the magnitude of the momentum transfer from these collisions. This effect is likely a relaxation of elastic stresses in the system.

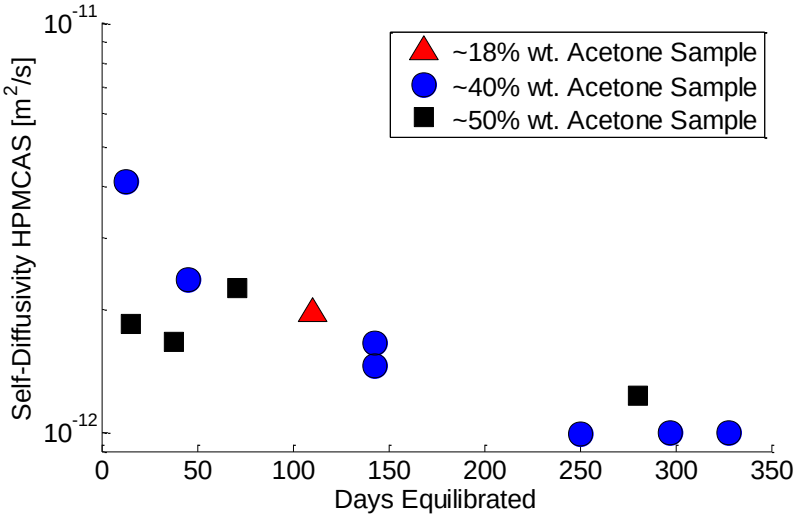

Figure 4.13. The effects of sample equilibration time on HPMCAS self-diffusivity.

Shown in figure 4.7, HPMCAS self-diffusivity measurements on HPMCAS-LF/acetone mixtures were consistent with the HPMCAS-MG/acetone mixtures at all concentrations measured. At these concentrations there are polymer-polymer interactions as well as acetone-polymer and acetone-acetone interactions. It may be that there is no difference in self-diffusion between these two grades over all acetone concentrations.

Self-Diffusivity: Temperature Dependence

PGSE experiments were performed on 45% wt. acetone and 10% wt. acetone samples at variable temperatures increased from 255 K to 303 K by 6 K increments. The dependence of acetone self-diffusivity on temperature for the two samples is shown in

Figure 4.14 on an Arrhenius scale, i.e. $\ln D = -E/k_B T$. The 45% wt. sample showed no difference in diffusivity between when the temperature was incrementally raised and when it was incrementally lowered.

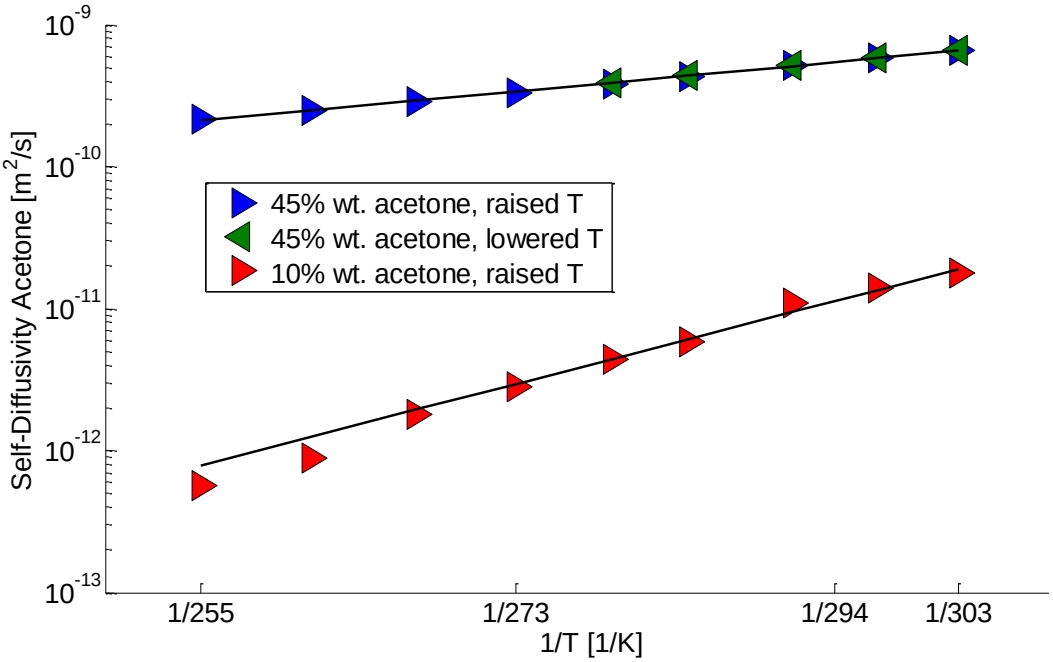

Figure 4.14. Arrhenius plot of the acetone self-diffusivity for a 45% wt. and a 10% wt. acetone sample. The lines are fits of the Arrhenius form. The glass transition temperature of the 10% wt. sample was predicted by the Fox equation to be 294 K.

The Arrhenius fit to the 45% wt. data is clearly good over the 255 to 303 K range and yields $E/k_B = 1830$ K. The 10% wt. sample was predicted by the Fox equation to experience a glass transition at 294 K. The slope of the Arrhenius fit $E/k_B = 5130$ K is different from that of the 45% wt., which could be seen as the effect of temperature change on the already limited amount of free-volume near the glass transition at 10% wt. having drastic effects on the diffusivity. The difference in Arrhenius behavior is well documented for viscosity measurements at $T_g/T \leq 1$ and indicates fragility [33], and

some have proposed a fragile to strong crossover for glass forming liquids which is associated with dynamic arrest [31]. Though more research is necessary to identify the critical point of dynamic arrest, the data seems to indicate that diffusive motion is sensitive to small changes in temperature and composition near the glass transition. With decreasing temperature, the acetone diffusivity of the 10% wt. sample dropped to and below the smallest measured HPMCAS diffusivities at ambient conditions (see Figure 4.7) and shows no sign of plateauing.

Similar to the effect of critical points, it is desirable to reduce the weight percent and temperature dependent self-diffusion data by the glass transition temperature (T_g). Angell and other researchers have reduced viscosity data using T_g/T as the abscissa and have used the relative non-Arrhenius shape of these plots (bowed rather than linear on a semi-log plot) to judge the degree of system fragility[33]. Through the Stokes-Einstein-Sutherland equation, self-diffusivity is inversely proportional to viscosity. The data in Figure 4.15 shows all of the acetone self-diffusion data plotted in this way.

Though Figure 4.15 doesn't reduce all of the data, it does show a discontinuity near the glass transition. Diffusivity plateaued near the glass transition, but once a concentration threshold was crossed the diffusivity plummeted. Note that these systems increased past the $T_g/T=1$ threshold by acetone evaporation. This raises an interesting question to whether there could be a difference between glass transitions by composition versus temperature.

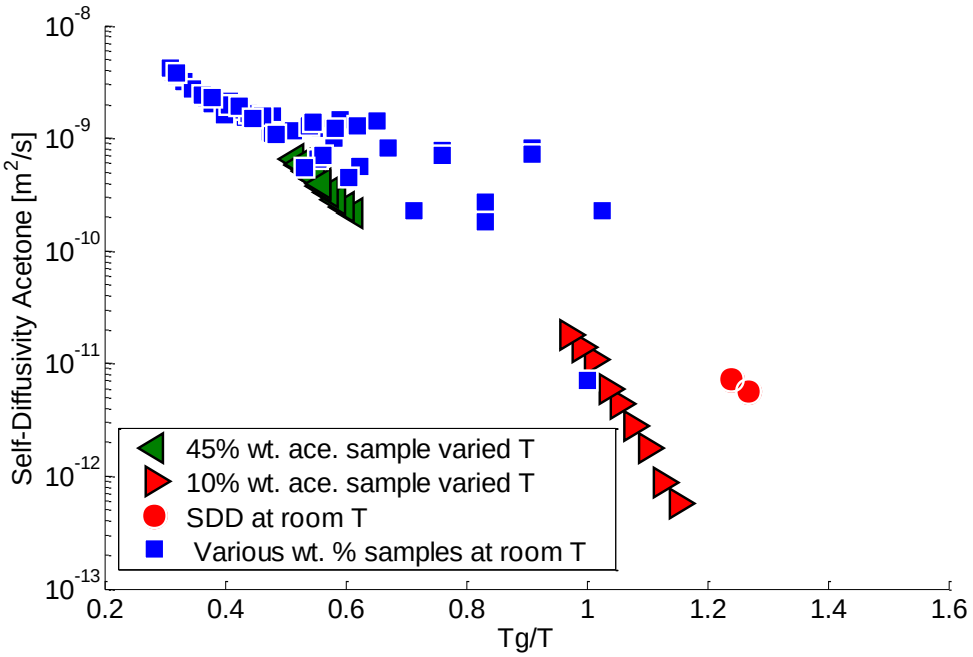

Figure 4.15. A plot of acetone self-diffusivity vs. T_g/T using the Fox equation to reduce the weight percent dependent data.

The Stokes-Einstein-Sutherland equation (2.8) can be used to relate acetone self-diffusivities in Figure 4.15 to viscosities. If the viscosity of acetone at 20° C is 3.3×10^{-4} Pa s [59], and the self-diffusivity of acetone was measured to be 4×10^{-9} m^2/s, then the radius of the acetone molecule is 1.6 angstroms. Angell found that most materials have a viscosity of 10^{12} Pa s at $T_g/T=1$ [39]. Using this value and the calculated acetone radius, the Stokes-Einstein-Sutherland equation predicts a self-diffusivity of 10^{-24} m^2/s. It is not known why this predicted value and the measured acetone self-diffusivity of 10^{-12} m^2/s at the glass transition are 12 orders of magnitude different. One possibility discussed previously is T_2 weighting of the measured self-diffusivity towards the most mobile acetone population. There could be acetone, as well as polymer, with a self-diffusivity of 10^{-24} m^2/s, that is not picked up by the PGSE experiment.

Previous researchers have plotted the mean squared displacement of proteins and biopolymers in solution vs T/T_g and have seen linear fits between the glassy state and rubbery state occurring near the glass transition [39]. Again reducing the data by the Fox equation calculation of T_g, such a plot for the acetone self-diffusivity data is shown in Figure 4.16. The fits to the 10% wt. (glassy state) and the 45% wt. (rubbery state) temperature dependent data indicates a glass transition; at this point little credence should be put into the transition occurring at T/T_g=1.5 rather than 1.

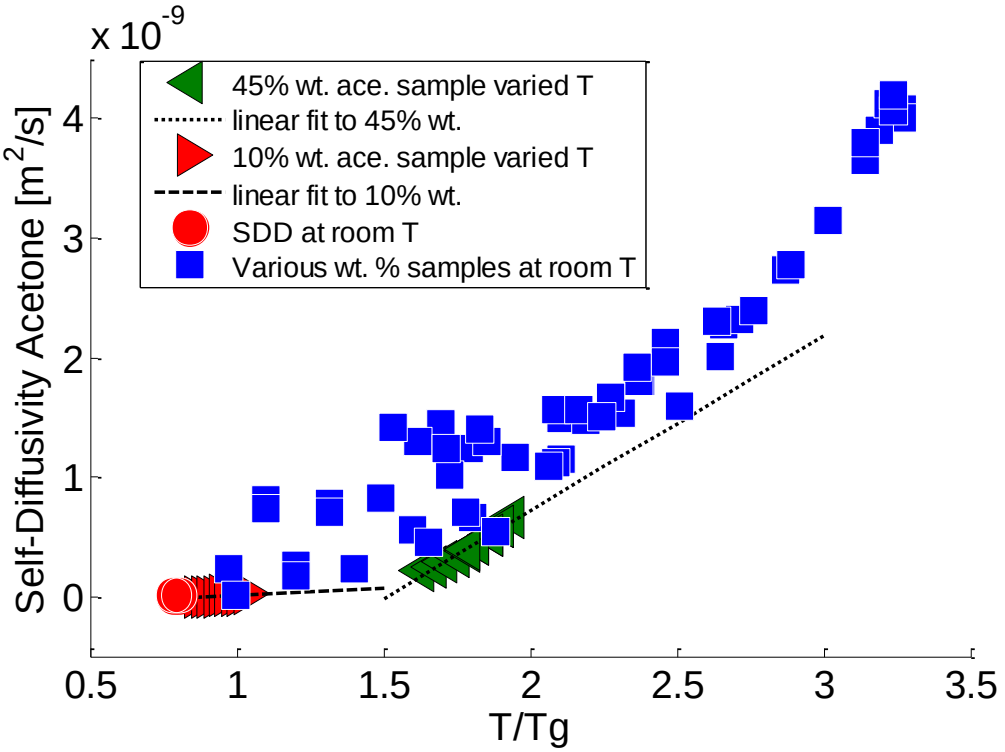

Figure 4.16. A plot of acetone self-diffusivity versus T/T_g using the Fox equation to reduce the data.

Due to signal loss from T_2 relaxation, the signal from the HPMCAS was detectable only for the 45% wt. acetone sample at 267 K and above. Temperature dependent HPMCAS self-diffusivity measurements on the 45% wt. acetone sample are

shown in Figure 4.17. The sample showed a maximum diffusivity at the coolest temperature measured, 267 K, and the diffusivity decreased as the temperature was raised to 291 K and increased only slightly upon further heating. This may be due to T_2 relaxation weighting between faster and slower diffusion populations. Physically, self-diffusivity must increase with increasing temperature.

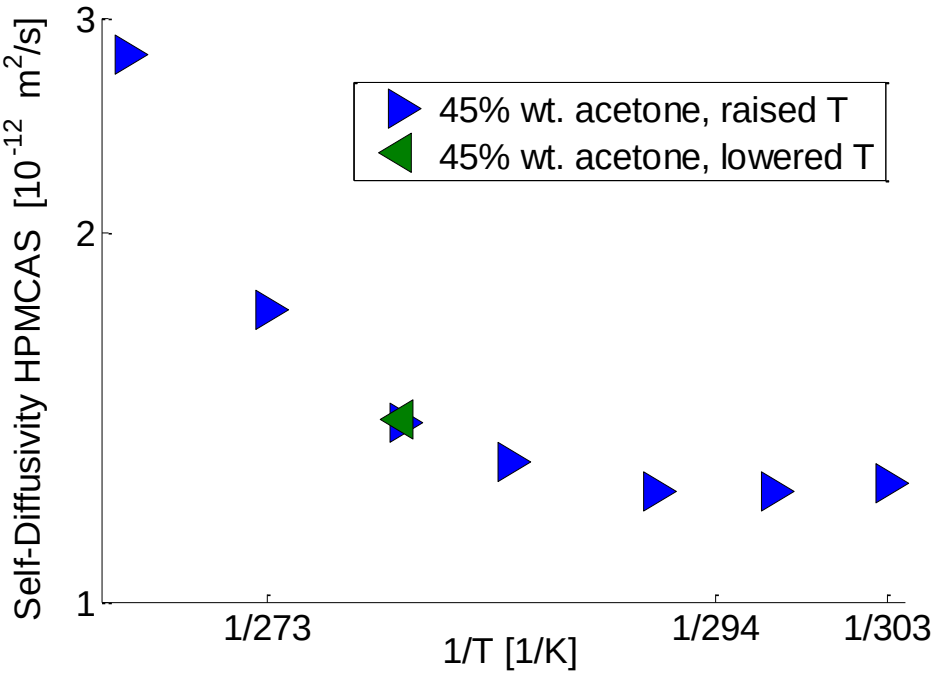

Figure 4.17. Temperature-dependent HPMCAS self-diffusivity of a 45% wt. acetone sample. The black line is an Arrhenius fit to the data.

PGSE experiments on the HPMCAS for inverse Laplace transform were run at 273 K, 284 K, and 303 K. The overlay of the three self-diffusion distributions is shown in Figure 4.18. There are consistently two diffusion populations, and the stationary population at 10^{-12} m^2/s dominates. The population of larger diffusivity values shifts

down from $3x10^{-11}$ m^2/s to $1x10^{-11}$ m^2/s between 273 K and 284 K and then shows the same peak value at 303 K.

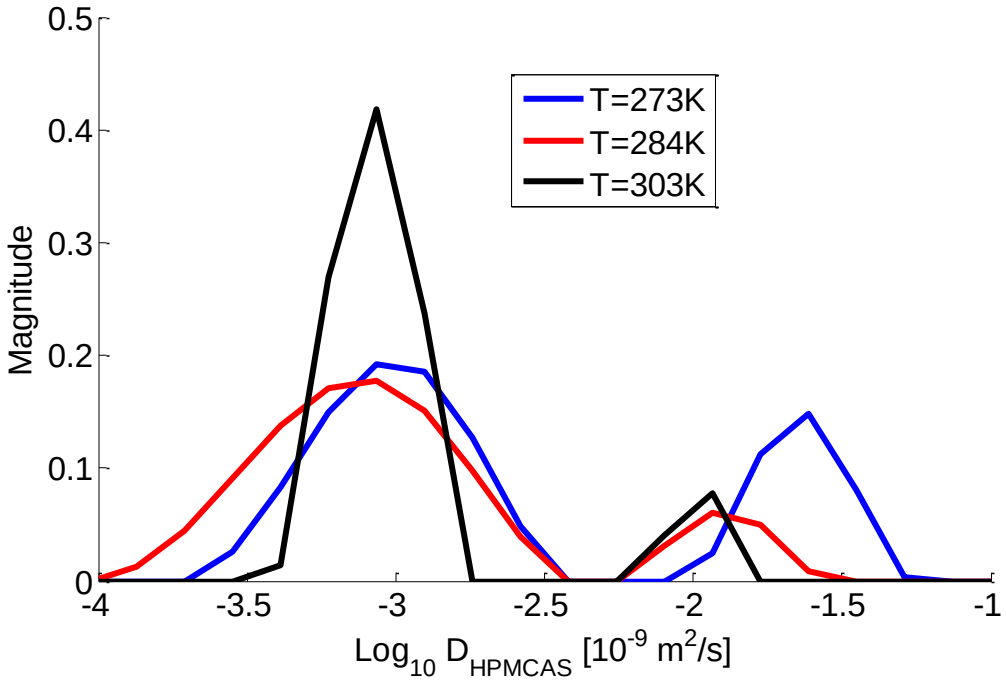

Figure 4.18. Temperature-dependent HPMCAS self-diffusivity distributions of a 45% wt. acetone sample.

The peak widths decrease with increasing temperature, which is consistent with the increase in interactions seen by the molecules due to increased thermal energy. This shows the validity of a distribution of diffusivities; rather than simply bi-exponential or two delta functions in the distribution, broad distributions are more indicative of the system.

It is seen below in figure 4.23 that T_2 populations of the 45% wt. acetone sample are near and below the PGSE $\tau = 2.5$ ms. Relaxation weighting of the PGSE signal towards the longest T_2 population must have occurred in the temperature dependent

PGSE experiments on HPMCAS in the 45% wt. acetone sample. Figure 4.24 will show that the relaxation populations near a millisecond increase in T_2 with increasing temperature. Within the distribution of T_2 populations near a millisecond are the two diffusive populations seen in Figure 4.18, and it is probable that the T_2 correlates to these diffusivities. As the temperature is lowered, signal from populations with T_2 less than 1 ms will become increasingly undetectable by PGSE, more so than the populations with T_2 greater than 1 ms, thus resulting in increased weighing towards the fastest diffusivity with decreasing temperature. The effects of T_2 weighting can't currently be separated from the temperature dependent PGSE measurements on HPMCAS.

T_1-T_2 Correlation Experiments

Two dimensional T_1-T_2 correlation experiments were run on HPMCAS/acetone mixtures. The two dimensional Laplace inversion of the experimental data gives a 2D contour plot showing the magnitudes of populations with a specific T_1 and T_2 [2]. Though it was found that populations were resolved generally in the T_2 direction rather than the T_1 direction, a T_1-T_2 versus a 1D T_2 more easily resolved distinct populations and the additional T_1 direction revealed artefacts when experimental parameters were not correct.

Six T_1-T_2 relaxation distributions for varying polymer-solvent concentrations are shown in Figure 4.19. In a single T_1-T_2 plot, the spread in T_2 relaxation times present covers 5 orders of magnitude. To sufficiently sample the signal decay from T_2 populations over this range is a challenge. Theoretically, the shortest and longest T_2 values that can be resolved are on the order of the time of the first acquired echo and the last acquired echo respectively. For a 15 μs τ and 6000 acquired echoes, this gives a

range from 30 μs to 180 ms, though in practice the range is larger than this. Additional echoes were not used due to the diminishing returns from each additional 1000 echoes being met with increased risk of the RF coil overheating or heating of the sample. Clearly the τ time is the key parameter to the resolution of these experiments.

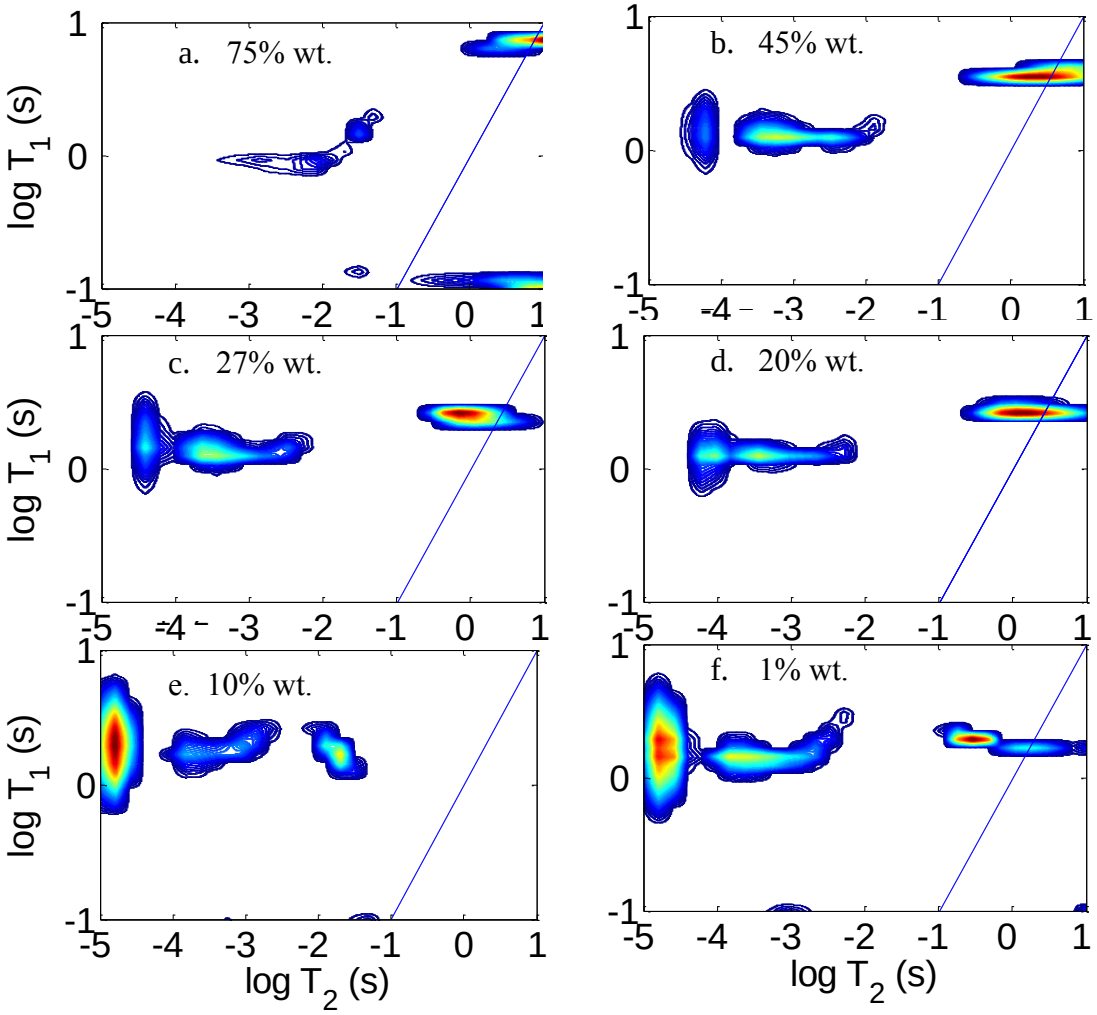

Figure 4.19. T_1-T_2 correlation maps of various percent weight acetone mixtures using τ = 15 μs (a., c., d. and f.) or τ = 12 μs (b. and e.)

In all of the correlation distributions, there are consistently 3 separate populations. The identity of spins which compose these three populations is not exact since unlike the

chemical shift spectrally resolved diffusion data the T_1-T_2 data is not spectrally resolved since a full echo is not acquired in each 2τ interval. One of the three populations has a T_2 around a second in all of the correlation maps and lies on or near the blue dotted line known as the parity line. The parity line is where T_1 is equal to T_2. Below this line is aphysical as T_1 cannot be less than T_2. Populations lying below this line are artefacts and have been seen when a sufficient fraction of the echo decay was not sampled.

T_1-T_2 populations lying on the parity line are small fluid phase molecules. The reasoning behind this can be traced back to the rotational correlation model, shown in Figure 1.3. In this model, T_1 is equal to T_2 for small molecules with large rotational mobility such as liquids and have values on the order of seconds [2]. Therefore, the T_1-T_2 population on the parity line is acetone. Decreasing the percent of acetone increased the number of acetone-polymer interactions relative to acetone-acetone interactions. The correlation time of acetone- polymer interactions is much longer than acetone-acetone interactions due to the relative rotational immobility of polymer molecules. This moved the acetone relaxation population in distributions 4.19a through 4.19d down to smaller values along the T_1=T_2 parity line. Reducing the percent of acetone further, to 10% wt. shown in 4.19e, the acetone population moved off of the parity line. A T_1 minimum and its divergence from T_2 are predicted by the rotational correlation model [2]. The acetone T_2 decreased roughly an order of magnitude between 75% wt. acetone and 20% wt. acetone. Note that over a similar weight percent range an order of magnitude decrease in the acetone self-diffusivity was seen in Figure 4.1. Between 20% and 10% wt., the acetone T_2 decreased almost two orders of magnitude, from 1 s down to 20 ms, which is

again similar to the acetone self-diffusivity change between these two concentrations. Acetone T_2 is sensitive to the glass transition, and though the glass transition is classically associated with a phenomenon of arrested translational motion [31], this shows that there is also arresting of rotational motion.

The T_1-T_2 relaxation distribution of the 1% wt. acetone sample, Fig. 4.19f, shows an acetone population, or possibly two acetone populations, much closer to the parity line than in the 10% wt. acetone sample. The break in the trending decrease of the acetone T_2 with concentration could be due to sample preparation. When the sample contained more acetone (13% wt.), it was capped and held at 40° C to remove bubbles. Though the Teflon NMR caps were found to successfully hold in volatile acetone at 20° C, this was not true for 40° C, and the sample slowly leaked acetone vapors to its final 1% concentration over roughly two months. This T_1-T_2 distribution could be indicative of phase separation. The short T_2 components are consistent with the T_1-T_2 distribution of the 10% wt. sample showing that there is a tightly entangled polymer-rich phase. The two overlapping acetone populations are consistent with acetone in an acetone rich phase having more mobility. Acetone which samples the polymer phase dephases more quickly and acetone which stays in the acetone phase dephases less quickly. There could be a third acetone relaxation population, masked by the short T_2 components, which is due to the minor amount of acetone in the polymer-rich phase. The glassy sample may be unable to release its elastic energy and re-absorb the acetone. More experimentation is necessary to test these hypotheses.

Spin dephasing or the loss of phase coherence is T_2 relaxation. The main cause of dephasing is dipole-dipole interactions. These directional interactions change the local electromagnetic field of the spins, which momentarily shifts the Larmor frequency. Hydrogens on acetone molecules experience enough interactions with enough neighbors from enough directions that the dephasing effects of these interactions cancel each other out. This averaging of the dephasing effects of dipole-dipole interactions is primarily due to fast rotational tumbling [2]. The HPMCAS T_2 relaxation times are much less than acetone due to the increased correlation time of interactions. Tumbling of the entire molecule as a mode of averaging the dephasing interactions is nearly cut off for a polymer molecule, particularly when a network is present. The hydrogens bonded to HPMCAS have a range of rotational mobility depending on their locations along the molecule. The rotational freedoms of hydrogens along the backbone are restricted when compared to hydrogens on functional groups. It is reasonable that a spread in the HPMCAS T_2 would exist. By this reasoning, it is believed that the two shortest T_2 peaks contain signal from the polymer.

The shortest T_2 relaxation time must be from HPMCAS signal, because acetone cannot have a shorter T_2 than HPMCAS. The peak that is of slightly larger T_2 values must also contain HPMCAS because the high-q^2 PGSE experiments at concentrations where the signal from the shortest T_2 component was filtered out by the experimental τ time still show the spectra of the polymer (Figure 4.5). As a final affirmation, it will be shown that the HPMCAS powder alone (without solvent) contains two populations.

The two fastest relaxing populations may not be distinctly HPMCAS, as highly polymer associated acetone taking on rotational mobility similar to the polymer could have short T_2 values which overlap with those of the polymer. However, for clarity in discussion, these peaks will be labeled, from largest to shortest T_2: HPMCAS peak #1 and HPMCAS peak #2. The peak names are labeled in Figure 4.20.

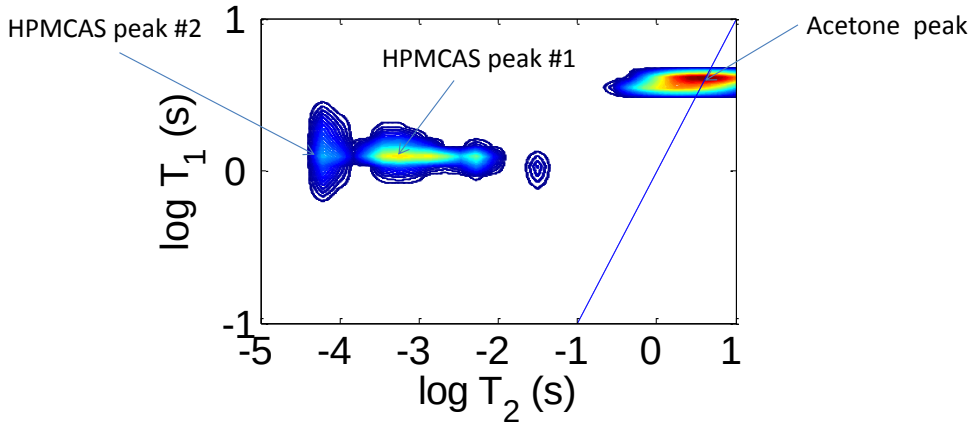

Figure 4.20. A relaxation map showing the names given to the three relaxation populations as well as the locations of the contour peaks for the 45% wt. acetone sample at 303K.

The HPMCAS peak #1 and peak #2 decreased 2 orders of magnitude in T_2, from 10 ms to 100 µs, between 75% wt. acetone and 20% wt. acetone (Fig. 4.19a-d). Interestingly, the HPMCAS self-diffusivity decreased by less than a single order of magnitude over this weight percent range in Figure 4.7. The T_2 is sensitive to additional entanglements, whereas after a point, the HPMCAS self-diffusivity is not. The HPMCAS peak #1 stretches almost two orders of magnitude for the 45% wt. acetone sample (Fig. 4.19b), but is much more localized in the 75% wt. sample (Fig. 4.19a). This may be due to the artefact present in the 75% wt. relaxation map, however it may also show sample to

sample variation and aging, similar to the scatter in the diffusivity plots (Figure 4.1 and 4.7).

The components' T_2 values define how long magnetization can spend in the transverse plane. This was important for the PGSE measurements, as most of the polymer signal becomes undetectable at low (less than 20% wt.) acetone content. The T_1-T_2 measurements can give a quantitative look at the polymer signal loss. T_2 Populations below the PGSE echo time of roughly 5 ms become undetectable with PGSE. The T_1-T_2 of the 75% wt. acetone sample shows the shortest T_2 relaxation time beginning to drop below a millisecond. The T_1-T_2 of the 38% wt. and 27% wt. acetone samples show this shortest population lying entirely below 1 ms, indicating that a portion of polymer signal from the fastest relaxing spins was lost in the low weight percent acetone samples due to T_2 relaxation. Additionally, PGSE measurements of the HPMCAS become increasingly T_2 weighted towards the slower relaxing population (peak #1). It is believed that HPMCAS peak #1 and peak #2 are intrinsic to every HPMCAS molecule in the system; every HPMCAS molecule has protons in both populations. In the case that the diffusive length scale is larger than a polymer molecule (Fig. 4.10), the diffusivity of any hydrogen on the molecule is the same as the center of mass diffusivity of the molecule itself, and T_2 weighting should not skew the diffusivity measurements. However, the distributions of translational diffusivities likely have a complex interrelation to the distributions of T_2 and rotational diffusion. Additional clarification may come from D-T_2 correlation experiments.

The T_1 values from all measurements of the polymer, and at low weight percent the acetone, hover around a second. As discussed in Chapter 1, T_1 relaxation is caused by coupling between the magnetic field of the spin and the lattice, and happens most efficiently (shortest T_1) when spins possess a certain frequency of motion. The rotational correlation model predicts the minimum in T_1 occurring when the correlation frequency associated with the molecular tumbling is equal to the Larmor frequency or twice the Larmor frequency [2]. Because there is no distinct minimum in T_1 for the polymer, it appears that the probability that a spin on the polymer has a correlation frequency of 300 or 600 MHz (the Larmor and double the Larmor frequency of the hydrogen) doesn't change with weight percent. Some level of fast-frequency fluctuations is intrinsic to the polymer. This affirms our understanding that polymers show liquid-like characteristics. Interestingly, this doesn't change in the glassy state.

In Figure 4.19, the acetone peak decreases in T_1 with decreasing acetone content until roughly 27% wt. acetone, at which point the T_1 is equal to the polymer populations present, and further decrease shows no change in T_1. The fast frequency motions of the acetone solvent become like those of the polymer at 27% wt.

T_1-T_2 correlation experiments were performed on the SDD samples. The resulting correlation maps in figure 4.22 show three populations that are qualitatively similar to the three populations seen in the correlation maps of the mixtures created in-house (Figure 4.19). The majority of the signal resides in the population around 10 μs. The breadth of this population in the T_1 direction may be due to insufficient sampling of the component's signal during acquisition in the CPMG train (Fig. 2.8) and not indicative of the sample. It

is an interesting property of the ILT of T_1-T_2 experiments that populations are typically always completely resolved. This is not the case for 1D T_2 experiments, even with a large number of averages. The minor component peaks are bridged together with one peak around 100 μs and the other around 1 ms.

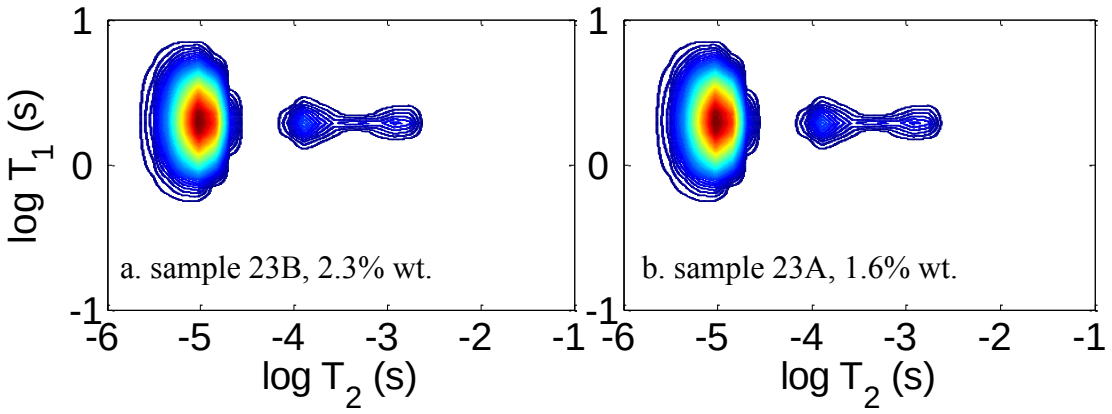

Figure 4.21. T_1-T_2 correlation maps of the wet (sample 23B, 2.3% wt. acetone) and dry (sample 23A, 1.6% wt. acetone) SDD samples.

A T_1-T_2 correlation experiment was performed on pure HPMCAS-MG powder. The resulting correlation map, shown in Figure 4.23, reveals two populations. The larger population, with a peak value of 9 μs, is clearly on the edge of the experimental resolution because of the τ, equal to 15 μs for this experiment. In comparison to the SDD samples (Figure 4.22), the two populations line up closely with the two shorter T_2 populations in the SDD. The presence of two T_2 populations intrinsic to the polymer was hypothesized for the HPMCAS mixtures, and is now confirmed in the absence of solvent, supporting the choice of peak names (HPMCAS peak #1 and peak #2) in Figure 4.20.

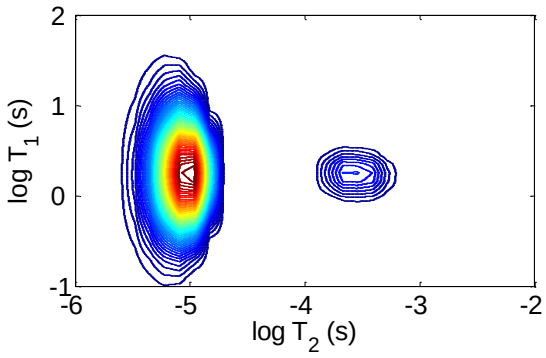

Figure 4.22. The T_1-T_2 correlation map of pure HPMCAS-MG powder

T_1-T_2 correlation experiments were performed on 45% wt. acetone and 10% wt. acetone samples at variable temperatures ramped down from 303 K to 255 K by 6 K increments. Following the experiments at 255 K, the temperature was ramped back up and select temperatures were re-tested. T_1-T_2 correlation maps from 303 K, 273 K, and 255 K are shown in Figure 4.23.

With decreasing temperature, for the 45% wt. acetone sample, the acetone population moved down and off the parity line and the HPMCAS peak #1 narrowed such that there was very little of the peak between 1 and 10 ms at 255 K. Temperature has a clear effect on the acetone T_2, for which thermal energy plays a key role in mobility. The T_1 of the acetone peak decreased from 4 s at 303K to 2 s, equal with the polymer, at 255 K. The fast molecular motions of the acetone become like that of the HPMCAS in the 45% wt. sample at 255 K. The 27% wt. acetone sample also showed this trait, and the T/T_g of the 45% wt. sample at 255 K is 1.6, and T/T_g of the 27% wt. sample at 294 K is 1.4. The similar values of T/T_g at the point when the T_1 plateaued may show the T_1-T_2 correlation experiment as a measure of glassiness. On HPMCAS peak #1, the re-allocation of the magnitude towards the T_2 of greatest magnitude with decreasing thermal

energy may be due to weak molecular forces acting for longer times, and thus increasing the rotational correlation time of the spins. The population of the shortest T_2, HPMCAS peak #2, shows little to no change with temperature; thermal energy has no effect on this group of spins.

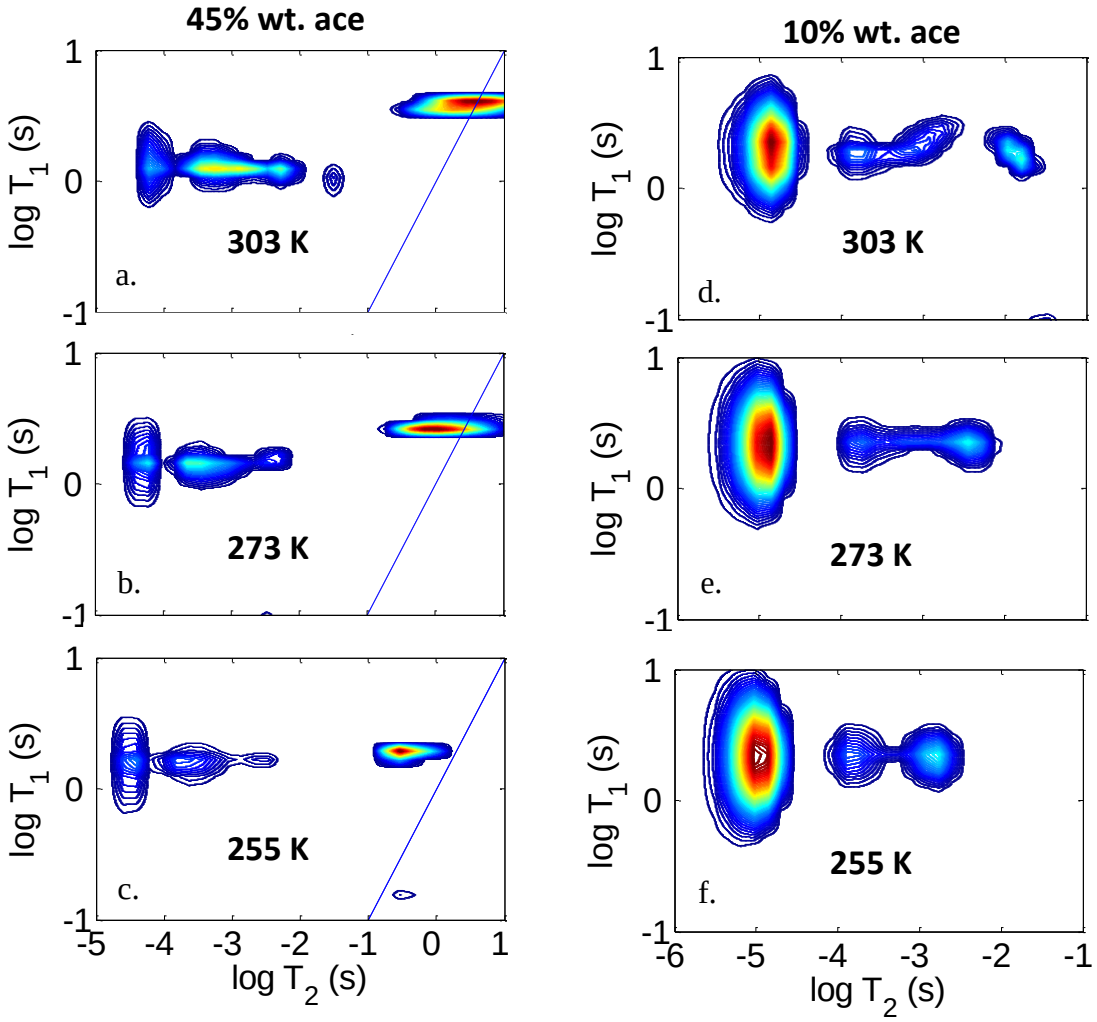

Figure 4.23. Temperature dependent T_1-T_2 correlation maps of a 45% wt. and a 10% wt. acetone sample.

For the 10% wt. acetone sample, the acetone population, far from the parity line, is more solid-like at all temperatures. With a peak value of 10 ms at 303 K, the acetone

population T_2 decreases with temperature and merges onto HPMCAS peak #1. One can imagine the hydrogen on acetone becoming similar in dynamics to the hydrogen on HPMCAS functional groups as the loss of thermal energy increases the length scales of molecular association. This is consistent with the growth of correlated regions which occurs near the crossover temperature of dynamic arrest (discussed in Chapter 2) [31].

The major signal contribution within the T_1-T_2 correlation maps of the 10% wt. acetone sample clearly comes from HPMCAS peak #2. The ratio between the signal magnitude of HPMCAS peak #2 and peak #1 is greater than 1 at 10% wt. and less than 1 at 45% wt. acetone. Because the ratio between hydrogens on the backbone to hydrogens on functional groups does not change, it appears that peak #2 is not solely backbone hydrogens and peak #1 not solely functional group hydrogens.

Note the qualitative similarity between the T_1-T_2 correlation maps of the 10% wt. sample at 255 K (Figure 4.22f) and the SDD samples at 294 K (Figure 4.21). One method of characterizing the dynamics of systems at varying temperatures and compositions is via the ratio of the temperature to the mixture's glass transition temperature [39]. The Fox equation (2.24) is an empirical and simplified correlation for Tg. Using this equation, the T/Tg of the 10% wt. acetone mixture at 255 K is 0.86 and the SDD samples at 294 K are 0.80. In this instance, T_1-T_2 correlation maps show the T/Tg for HPMCAS/acetone systems which were created in completely different ways.

All of the peak T_2 values at all experimental temperatures for both samples are shown in Figure 4.24 on an Arrhenius scale, i.e. $\ln T_2 = -E/k_B T$. T_2 values were roughly independent of whether the temperature was lowered or raised to set points,

indicating that hysteresis was negligible. The T_2 values of the acetone peak for both samples and the HPMCAS peak #1 for the 45% wt. sample change with temperature due to increased thermal motion which caused increased rotational mobility. From fits to the Arrhenius form, E/k_B was found to equal 3200 K for acetone peak of the 10% wt. acetone sample, 3500 K for the acetone peak of the 45% wt. acetone sample, and 2100 K for HPMCAS peak #1 of the 45% wt. acetone sample. The T_2 values of the other peaks remain roughly constant, with E/k_B values less than 500 K but greater than 0 K, due to thermal energy having little to no effect on the rotational mobility of hydrogens on polymer molecules within the entangled polymer network where electrostatic forces can dominate. The acetone populations at both concentrations change by one order of magnitude over the temperature range. Note that the change in acetone self-diffusivity over the extremes of temperatures tested was greater for the 10% wt. sample than it was for the 45% wt. sample (Fig. 4.14). Between the two weight percents, the acetone T_2 makes a drastic two orders of magnitude jump. This is significantly more than the T_2 changes of the other populations between 45% and 10% wt. This indicates the stronger association of the acetone with the polymer at 10% wt. than at 45% wt. acetone.

The two concentrations show equal HPMCAS peak #1 T_2 values between 255 K and 273 K. The rotational dynamics as well as the dipolar interaction experienced by this group of spins are the same between these two mixtures. Could it be that this group contains spins on the polymer which solvate the acetone? This would explain the change in the ratio of peak #2 magnitude to peak #1 magnitude between 45% wt. and 10% wt. The T_2 of Peak #2 decreased between 45% wt. and 10% wt. acetone but remained

constant with temperature. This population is intrinsically related to the mobility of the polymer network, which changed between the rubbery (45% wt.) and glassy (10% wt.) samples.

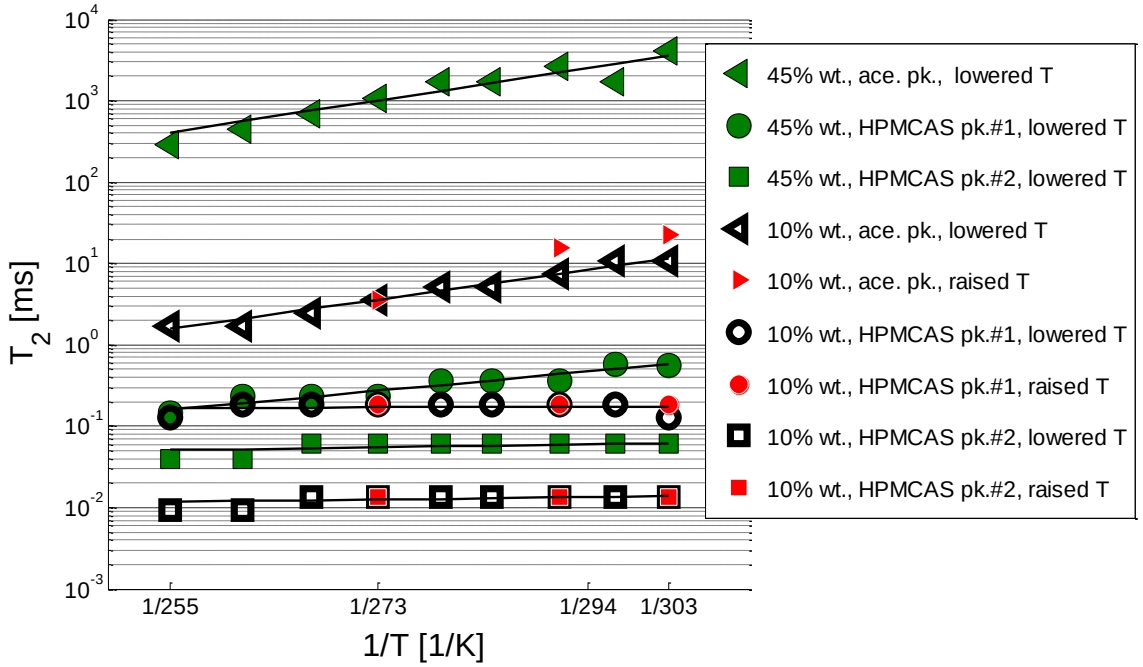

Figure 4.24. Temperature dependence of the peak T_2 values for the 45% wt. acetone and 10% wt. acetone samples.

<u>T_2-T_2 Exchange Experiments</u>

T_2-T_2 exchange experiments were performed on select samples. Figure 4.25 shows the T_2-T_2 exchange maps of a 47% wt. acetone sample with mixing time, τ_m, set to zero,100 ms, and 500 ms. Note that zero mixing time still has on the order of 10 μs of time between the two encoding periods when populations can mix. The T_2-T_2 exchange maps show all populations lying on the $T_2^{1st} = T_2^{2nd}$ axis when the mixing time was set to zero. This on-axis distribution is consistent with the T_2 distributions in Fig. 4.19-4.21 with the acetone peak around 3 s and HPMCAS peaks near 10ms and 100ms. This is to

be expected, as spins have insufficient time to exchange between environments and change their T_2. When the mixing time is set to 100 ms, off axis populations appear near the short T_2 components labeled HPMCAS peak #1 and HPMCAS peak #2, indicating the exchange of spins between these populations.

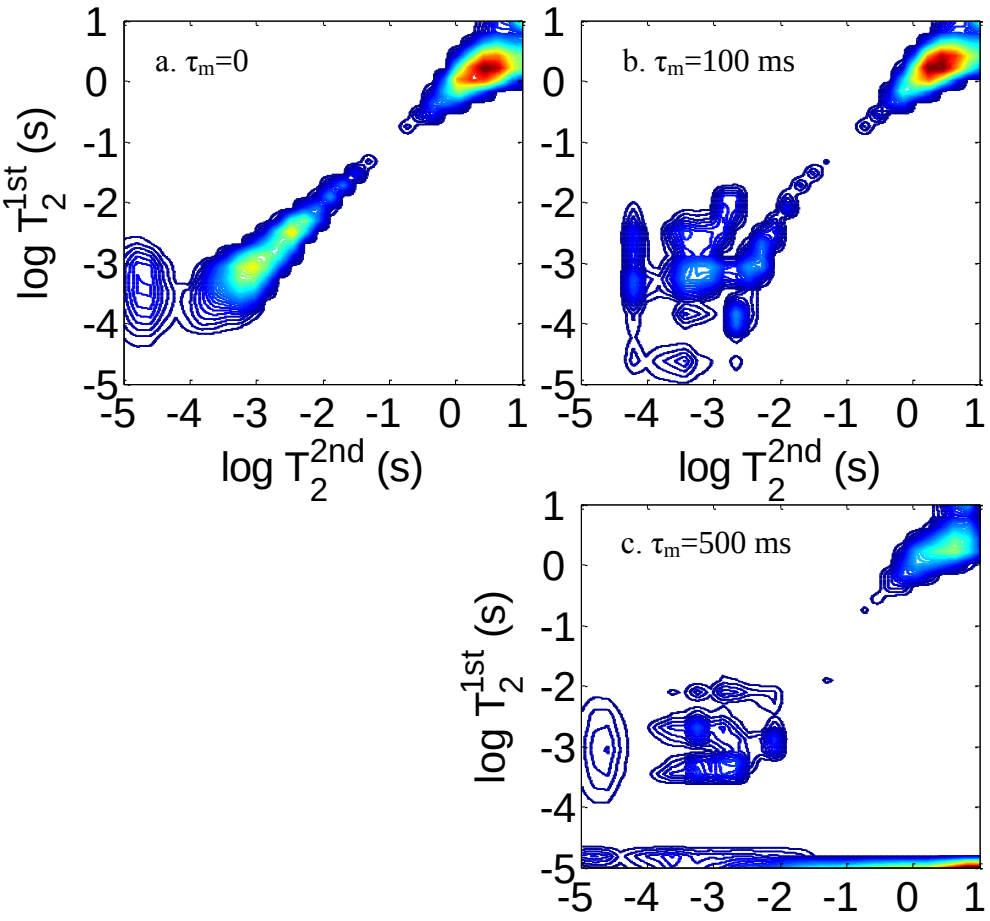

Figure 4.25. T_2-T_2 exchange maps of a 47% wt. ace. sample with mixing time, τ_m, set to 0 (a.), 100 ms (b.), and 500 ms (c.).

There are no off axis peaks associated to the population with T_2 between 1 and 10 seconds, labeled acetone peak in Figure 4.20. Earlier, in discussion of the T_1-T_2 distributions, it was unknown whether HPMCAS peak #1 and peak #2 contained acetone

signal. Acetone highly associated with the polymer could have a T_2 similar to the polymer as occurs in the merging of the acetone peak with the HPMCAS peak at 10% wt. acetone below the glass transition temperature in Fig. 4.23. Mixing between the acetone peak and the HPMCAS peaks is not seen in Fig. 4.25.

The T_2-T_2 exchange maps are undefined and have potential artefacts. The reason for this is the insufficient sampling of the echo signal decay associated with the acetone. Additionally, it was found that this experiment is best suited when T_2 is much less than T_1. Populations which have a T_1 roughly equal to T_2 will see variable amounts of T_1 weighting during the T_2 encoding periods, t_1 and t_2 in Figure 2.9. Figure 4.19b shows the acetone population with a T_2 roughly equal to T_1 for at 45% wt. ace. sample, therefore unaccounted for T_1 weighting is a problem for the acetone populations in the T_1-T_2 maps of Figure 4.25. To get around these problems, it was found that the acetone signal could be subtracted out from the data matrix by fitting exponentials backwards from the longest time points using the peak T_2 value found for the acetone. The resulting T_2-T_2 exchange maps, shown in Figure 4.26, are much cleaner than those in Figure 4.25.

The T_2-T_2 exchange map at zero mixing time shows the HPMCAS peak #1 and peak #2 along the T_2=T_2 axis. With the acetone signal removed, HPMCAS peak #1 and peak #2 are more pearled, binning the magnitude into these two anticipated populations. With 100 ms mixing time, off axis peaks appear, and there are more than just the peaks associated with exchange between HPMCAS peak #1 and peak #2. A fewer number of more defined mixing peaks are shown at the 500 ms mixing time. It is interesting that there are clear off axis peaks associated with the shortest T_2 of the HPMCAS peak #2 and

the longest T_2 of the HPMCAS peak #1. One explanation is that protons could be exchanging between locations in the entangled network through polymer reorientations.

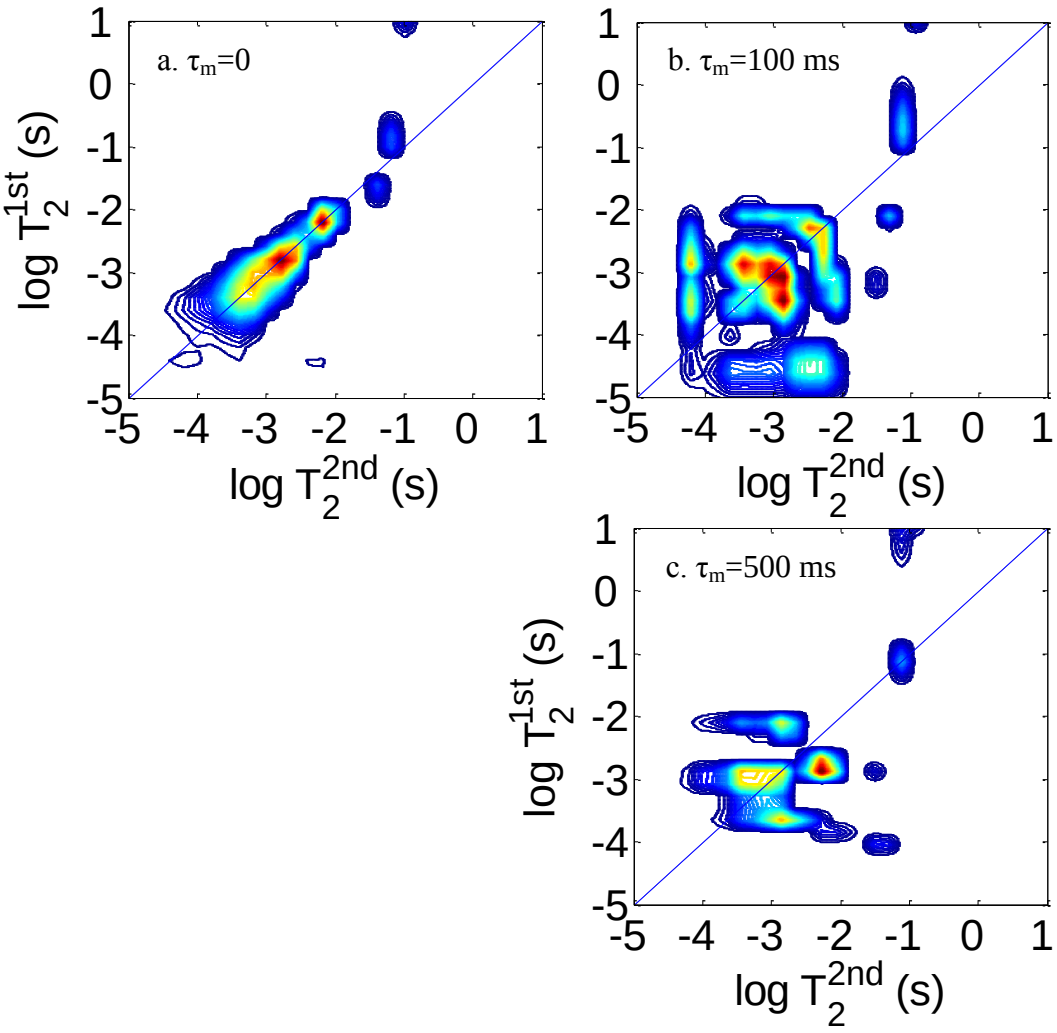

Figure 4.26. T_2-T_2 exchange maps of a 47% wt. sample with the mixing time, τ_m, set to 0 (a.), 100 ms (b.), and 500 ms (c.) after baseline subtracting the acetone signal from the data set.

T_2-T_2 exchange experiments were performed on the 1.6% wt. acetone wet SDD sample, 23A. The resulting exchange map for the 100 ms mixing time is shown in Figure 4.27. The distributions are not symmetric about the T_2^{1st}= T_2^{2nd} axis due to the major

signal component, resolved at slightly less than 10 µs from the second T_2 encoding period but unresolved and spread between 10 µs and 10 ms during the first encoding period. A 10 µs T_2 population was identified in the T_1-T_2 experiments on the SDD sample, and it is likely that the asymmetric peak occurs due to the insufficient sampling of signal from this T_2 population due to the T_2 being less than but on the order of the τ time.

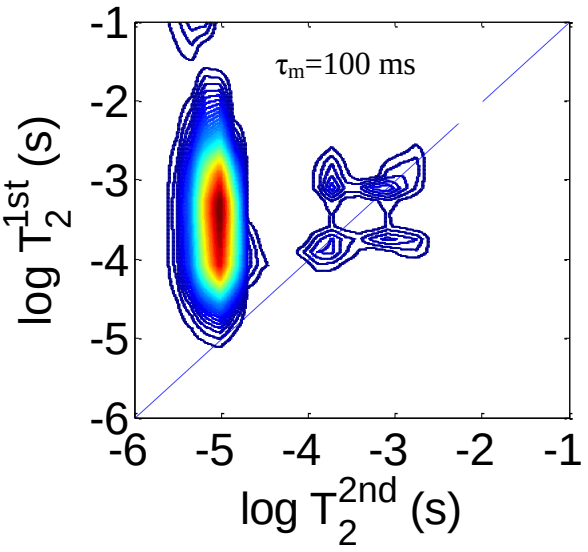

Figure 4.27. T_2-T_2 exchange map of the 1.6% wt. acetone wet SDD sample, 23A, with τ_m, set to 100 ms

Two tiny populations are resolved at T_2 values of 100 µs and 1 ms, and off axis peaks associated with their exchange are also seen. From the presence of off axis peaks, it is apparent that there is some finite mixing time associated with a mixing time of zero due to exchange during the time between the end of the first and start of the second T_2 encoding periods, roughly 10 µs. The off axis peaks contain more signal magnitude when a mixing time of 100 ms is used, as is expected. To create a cleaner view of these exchanging peaks, the signal from the short T_2 population was removed by removing the

signal associated with less than the 6th echo. Thus, a minimum of 288 µs ($24\,\mu s/echo\ \times 12\ echoes$) of T_2 relaxation was seen by all of the echoes in the data matrix. The resulting T_2-T_2 correlation maps are shown in Figure 4.28. The growth in the off axis peaks between no mixing time and 100 µs is much more apparent. It is unknown whether the off axis peaks are due to acetone or polymer. If they are due to acetone, then the growth of off axis peaks with increased mixing time could be used along with the diffusion coefficient information to show domain size.

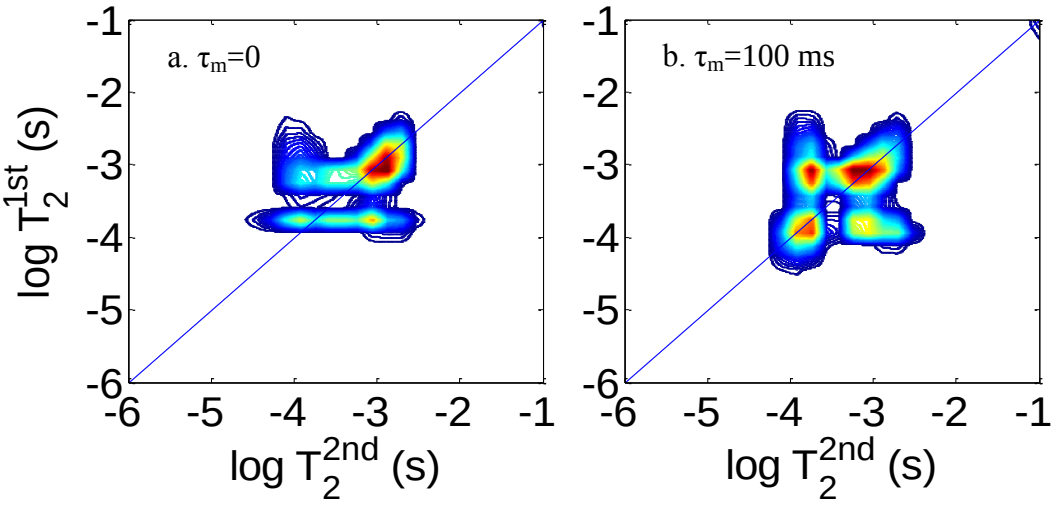

Figure 4.28. T_2-T_2 exchange maps of the 1.6% wt. acetone wet SDD sample, 23A, with τ_m, set to 0 (a.) and τ_m, set to 100 ms (b.) after removing points from the data matrix which contained signal from the 10 µs T_2 population.

In this section, the extraction of undesired signal by baselining as well as point removal from the data set has been shown. Though this can lead to incorrect interpretation of the results if done haphazardly, these methods have been useful here and are likely useful in other scenarios. Significant further research using τ_m times on the

order of 1 μs are needed to explore the potential of T_2-T_2 exchange experiments on polymer systems.

T_2 and T_1 Measurements of SDD

Prior to experimenting on the wet SDD with PGSE, T_1-T_2, and T_2-T_2 sequences, standard T_2 and T_1 measurements were made via CPMG and inversion recovery sequences. The T_2 distributions of the two wet SDD samples from a CPMG sequence using a 12 μs τ are shown in Figure 4.29 and are consistent with the T_1-T_2 distributions on these samples (Fig. 4.22). There is a small but measurable decrease in the longest T_2 peak. This peak shifts from 2.6 ms to 1.3 ms between the 2.3% wt. and the 1.6% wt. acetone samples. It is believed that this peak is signal from solvent, and it may be that the T_2 of this peak could be used to quantify residual solvent. This experiment, requiring 16 minutes to perform, could be an additional method of analyzing residual solvent.

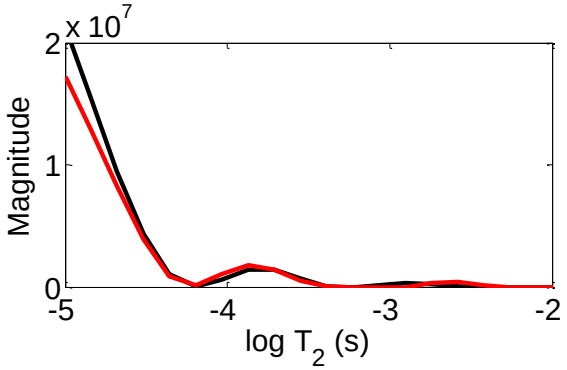

Figure 4.29. The T_2 distributions of the 1.6% wt. ace. (red line) and 2.3% wt. ace. (black line) SDD samples.

The realization that there could be minor amounts of signal from acetone within the wet SDDs which is attainable with PGSE using a τ =2 ms came from the T_2 distributions in Figure 4.28 consistently showing a slight T_2 population around a

millisecond. This is a great example of the complimentary nature of different NMR experiments.

The inversion recovery (T_1 IR) sequence doesn't use a spin echo and therefore has the potential to measure T_1 populations associated with T_2 values shorter than those measured by T_1-T_2 correlation experiments. A rule of thumb is that signal sees an amount of T_2 relaxation equal to half the pulse duration during 90° and 180° pulses. For the T_1 IR experiments on SDDs, the pulse times were set to 6 µs and 12 µs for the 90° and 180° pulses, so by rule of thumb the first points of the FIDs experience 9 µs of T_2 relaxation.

We were curious if SDD samples would show T_1 populations much greater than a second. From the rotational correlation model (Figure 1.3), it seemed that these solid samples could have very long T_1 relaxation times. T_1 distributions for the wet SDD samples are presented in Figure 4.30 and show a single T_1 population with relaxation time of 1.76 s and 1.64 s for the 2.3% wt. and 1.6% wt. acetone samples respectively. Multiple attempts at resolving more than a single T_1 population with inverse Laplace transform by using different variations of inversion times showed the same results. This value is consistent with the T_1-T_2 relaxation maps.

It is anticipated that crystalline drug would have T_1 values much greater than a second, and thus there is great potential for T_1 IR measurements analyzed by ILT to be a solid dosage quality control tool. Other techniques used in industry are able to spot crystalline drug in amounts greater that 5% wt. Of course it is all about how much of the signal is measureable, as T_2 will plummet upon crystallization, however it is plausible that the ILT analysis of a T_1 IR measurement with carefully placed inversion times could

show the presence of less than 5% wt. crystalline drug through additional T_1 populations. In this research it was found that components near one another begin to share relaxation characteristics with the increase in correlation lengths from dynamic arrest. It could be that though signal from crystal grains may not be measureable, molecules associated with the crystals with measurable signal would take on T_1 values closer to that of the crystal. This is a promising area of future research in solid-state NMR.

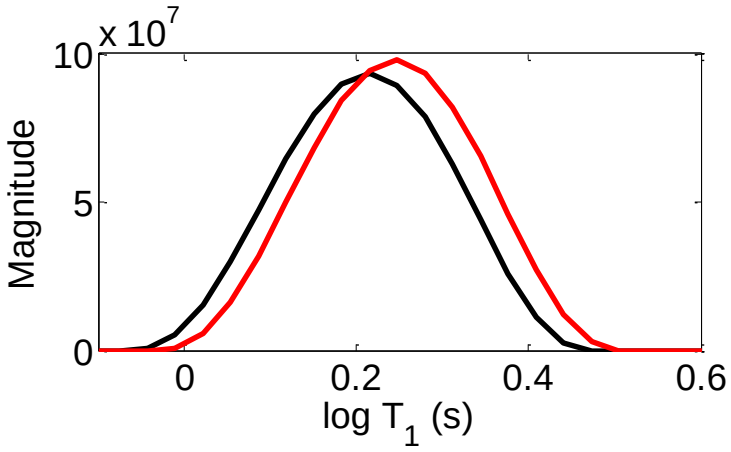

Figure 4.30. The T_1 distributions of the 1.6% wt. ace. (red line) and 2.3% wt. ace. (black line) SDD samples.

Conclusion

In this thesis, PGSE and multidimensional T_2-T_2 exchange and T_1-T_2 correlation NMR experiments were performed on variable weight percent HPMCAS-acetone mixtures. Certain concentrations were analyzed at variable temperatures around ambient.

The self-diffusivity of acetone showed an exponential decrease with decreasing acetone content, in agreement with certain theories [55], and a significant drop near the glass transition. Self-diffusion measurements were performed on acetone in wet SDD

granules. This data will be useful in the creation and validation of a model for diffusion through films formed during drying.

HPMCAS self-diffusivity decreased and plateaued with decreasing acetone content. Following the methodology of polymer characterization by rheological measurements, three polymer concentration regimes were proposed based on best-fits to exponentials [63] and validated by polymer self-diffusion models [55]. Inverse Laplace Transform of the HPMCAS PGSE signal attenuation revealed a broad, single peak at acetone weight percents greater than the proposed entanglement concentration (90% wt. ace.), becoming two peaks at concentrations less than the entanglement concentration. This may be due to long relaxation modes preventing the Brownian motion type dynamics from averaging out the causal polymer-polymer interactions over the NMR timescale. Additionally, this may be a consequence of polymer entanglement. Evidence of aging in rubbery mixtures was seen with both HPMCAS and acetone self-diffusion measurements on equilibrating samples. The term aging is currently reserved for glassy systems and its use in this research refers to the rearrangements of the polymer entanglement networks of rubbery systems. Self-diffusion measurements on mixtures of LF grade HPMCAS and acetone were similar to those of the MG grade mixtures.

The temperature-dependent self-diffusion measurements on a rubbery sample (45% wt.) and a sample near its glass transition (10% wt.) showed that NMR-measured solvent self-diffusion is sensitive to the glass transition. HPMCAS self-diffusivity in the 45% wt. sample was greatest at the lowest temperature measured and decreased with

increasing temperature. These counter-intuitive results are likely due to T_2 relaxation weighting.

T_1-T_2 correlation experiments consistently revealed three relaxation populations and it is believed that the two shortest times are primarily due to polymer signal and the longest relaxation time population is signal from acetone. Though populations plateaued to similar T_1 relaxation times with decreasing acetone content, the added time encoding dimension showed the presence of artefacts when parameters were not set precisely, and populations were more easily resolved in comparison to 1D T_2 measurements. Temperature-dependent T_1-T_2 correlation experiments showed that the T_2 relaxation time of the acetone population was sensitive to the glass transition, whereas the polymer populations' T_2 relaxation times were not. T_1-T_2 correlation maps of the SDD samples were similar in structure to that of the 10% wt. acetone sample at 255 K, below its predicted glass transition temperature. Using the Fox equation to estimate T_g showed that T/T_g, a measure of glassiness [39], was roughly equal in the samples. In this instance, T_1-T_2 distributions show the glassiness of HPMCAS/acetone systems which were created in completely different ways. From this preliminary research, the use of T_1-T_2 correlation experiments to characterize SDD shows promise. The next step will be to see if this experiment can reveal crystalline drug and glass phases in polymer-solvent systems.

T_2-T_2 exchange experiments showed mixing between the polymer populations in the samples made in-house and mixing between the longest T_2 components in the SDD samples. With the cause of mixing in these two instances still unknown, research should

be performed at more mixing times and more concentrations using solid state probes with RF pulses on the order of 1 μs.

T_2 and T_1 measurements on the SDD samples were consistent with the T_1-T_2 correlation maps. The longest T_2 relaxation time decreased with decreasing acetone content, and it may be possible to use PGSE experiments to quantify residual solvent if a standard curve is developed.

APPENDICES

APPENDIX A

SELF-DIFFUSIVITY IN SYSTEMS OF HPMCAS SOLVATED BY 90% WT. ACETONE, 10% WT. WATER

Introduction

In the creation of spray dried dispersions of drug (SDD), solvents are made up of a combination of volatile molecules based on the ability to keep the drug and polymer in solution. Other than acetone, used throughout this research, these combinations may include ethanol, methanol, and water. One solvent combination under current research is 9 parts acetone to 1 part water by mass, to be called 90-10 solvent upon further reference. The self-diffusivity of this solvent combination with HPMCAS was measured by PGSE NMR for mixtures of 80% wt. solvent and greater. One goal of this research is to see by how much the dynamics of these mixtures changes relative to HPMCAS mixtures with pure acetone solvent and to understand the science behind the changes.

Methods

Hydroxypropyl methylcellulose acetate succinate MG grade (HPMCAS-MG) polymer made by Shin-Etsu Chemical Co., Ltd. was mixed in various amounts with the 90-10 solvent and pipetted into NMR tubes. Five mixtures ranging from 100% wt. solvent to 80% wt. solvent were created. PGSE NMR experiments were performed on the samples with the same equipment and experimental parameters as the experiments performed on the HPMCAS/acetone mixtures, discussed in chapter 4. Diffusion coefficients of the water and acetone components were spectrally resolved from the same solvent-specific PGSE experiments. These experiments saw roughly 30% signal attenuation of the acetone signal and slightly less attenuation of the water signal. The smallest gradient value used in PGSE experiments to measure diffusion of HPMCAS

fully attenuated the water and acetone spectral peaks. The Stejskal-Tanner equation, discussed in chapter 2, was used to solve for the diffusivity of each component. The analysis methods are the same as those discussed with greater detail in Chapter 4.

Results and Discussion

The self-diffusivity measurements of acetone and water in HPMCAS/solvent mixtures are shown in Figure A.1 The acetone self-diffusivity data for HPMCAS/acetone mixtures less than 20% wt. acetone is re-presented for comparison. Measurements of pure component self-diffusivities are shown for comparison with the measurements of self-diffusion in the HPMCAS/90-10 solvent mixtures.

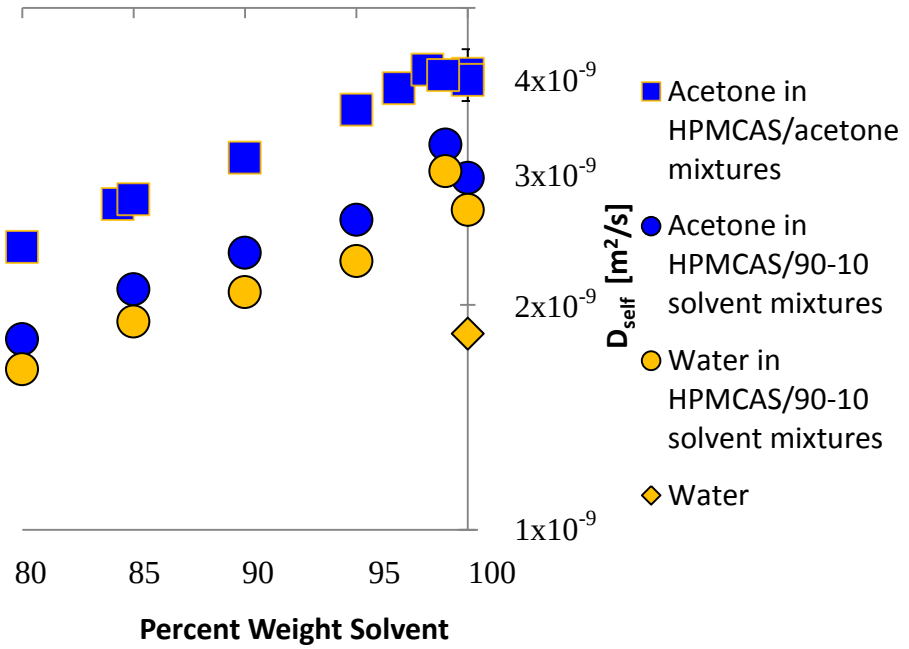

Figure A. 1. The solvent content dependence of solvent component self-diffusivity in HPMCAS/90-10 solvent mixtures as well as HPMCAS/acetone mixtures

From 99% wt. 90-10 solvent, self-diffusion of the acetone and water decreased logarithmically with decreasing solvent content over the range of concentrations tested. The logarithmic trend is the same for both components and runs parallel to the acetone self-diffusivity in the HPMCAS/acetone mixtures. Presented in Figure A.1, pure acetone has a higher diffusivity than pure water, 4.0×10^{-9} m^2/s vs. 1.8×10^{-9} m^2/s. In the HPMCAS/90-10 solvent mixtures the self-diffusivity values of the acetone are again higher than the water, but the difference is only 0.2 to 0.3 $X10^{-9}$ m^2/s.

Comparing the self-diffusivity of the acetone and water components alone to when in a 90-10 solution, the major component, acetone, showed a decreased diffusivity from 4.0×10^{-9} m^2/s to 3.0×10^{-9} m^2/s while the minor component, water, showed a raised diffusivity from 1.8×10^{-9} m^2/s to 2.7×10^{-9} m^2/s. This phenomenon is related to the colligative properties of solutions. When adding a soluble component in dilute amounts, the free energy of the major component decreases, making the component as well as the overall solution more stable. The increase in stability of the acetone resulted in the measured decrease in acetone diffusivity. Strengthening this conclusion, in the PhD thesis of A.L. Broadbent, the self-diffusivity of water in a solution of 8% wt. acetone/92% wt. water was measured at 1.8×10^{-9} m^2/s whereas she measured a higher value of 2.1×10^{-9} m^2/s for pure water; in the flip-flop of major-minor components the major component still decreased in diffusivity upon addition of the minor component. The self-diffusivity of the minor component, water, in the 90% wt. acetone/10% wt. water solvent increased from its pure component value, indicating that the free energy of this component increased.

The 99% wt. 90-10 solvent mixture showed increases in both acetone and water self-diffusivity from 100% 90-10 solvent. It may be that the addition of the excluded volume of the polymer obstructing the free path of the acetone was countered by the increased free energy of the mixture added by the polymer. This is only short lived and the effects of obstruction dominate at 5% wt.

The HPMCAS self-diffusion coefficient measurements on mixtures of HPMCAS/90-10 solvent are plotted in Figure A.2 alongside the measurements from HPMCAS/acetone mixtures. The HPMCAS self-diffusivity measurements for mixtures with 90-10 solvent are less than the HPMCAS self-diffusivity in pure acetone solvent for concentrations of 99, 95, and 90% wt. solvent, and become roughly equivalent at 85 and 80% wt. solvent.

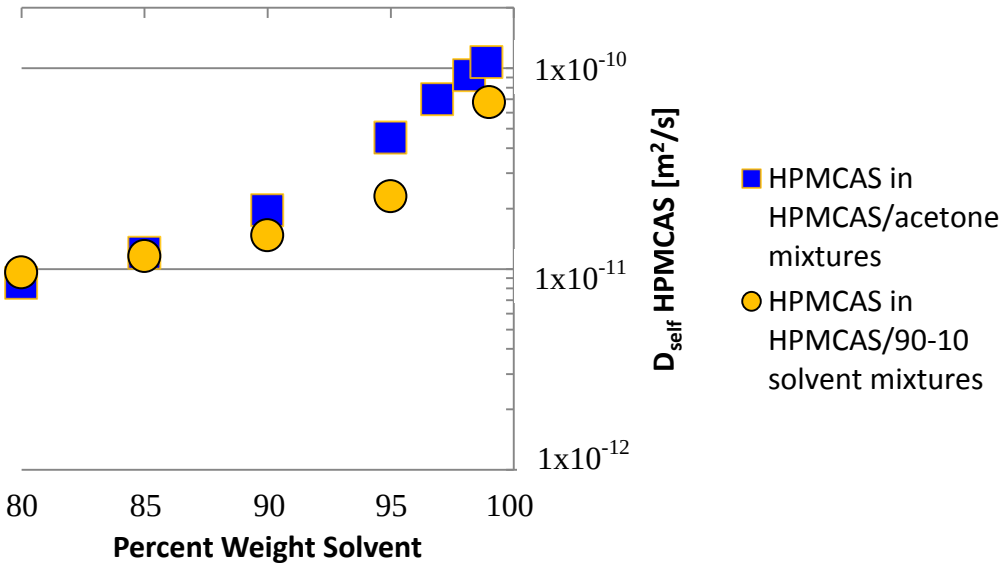

Figure A. 2. The solvent content dependence of HPMCAS self-diffusivity in HPMCAS/90-10 solvent mixtures as well as HPMCAS/acetone mixtures

The diffusivity of HPMCAS in HPMCAS/90-10 solvent mixtures may show two polymer regimes, similar to the two polymer regimes with pure acetone solvent seen in Figure 4.8, with a crossover near 95% wt. solvent, though more measurements between 1 and 5% wt. is necessary to support this conclusion. Nevertheless, in the study of HPMCAS/acetone mixtures in Chapter 4 this crossover was attributed to the entanglement concentration which separates the semidilute from the concentrated polymer regimes. The entanglement concentration is a large function of the solvent. In polymer physics, solvent quality ranges from poor to good and, among other characteristics, is seen with an increase in the polymer mean squared radius of gyration [14]. This increase in polymer radius of gyration increases the chance of topological constraints from the many polymer molecules, and thus one will expect to see the entanglement concentration of polymer molecules in better solvent occur at greater solvent concentrations. Visually, the entanglement concentration appears to shift to slightly larger solvent concentrations with the addition of water, indicating that the 90-10 solvent is a better solvent.

The HPMCAS self-diffusivities measured on mixtures solvated by 90% acetone/10% water are consistently less than the HPMCAS self-diffusivity measurements on mixtures with pure acetone solvent at solvent concentrations greater than 85% wt. In the Stokes-Einstein-Sutherland (SES) equation (2.8) the self-diffusivity is a ratio of the thermal energy to the hydrodynamic dissipation of that energy by the drag on the particle. With Stokes equation for drag on a sphere, the self-diffusivity is: $D = \frac{k_B T}{6\pi\mu R}$. From this equation it is seen that the increase in polymer radius, which occurs with increasing

solvent goodness, would result in decreased self-diffusivity. Though this scenario is plausible in the systems at hand, the water, which has a lower viscosity than acetone, also decreases the viscosity of the mixture, and from the SES equation it appears that the significance of these two causes cannot be separated without viscosity measurements. The equality of HPMCAS self-diffusivity for both mixture types at 85% wt. and 80% wt. solvent indicate that the polymer-polymer interactions have become more pertinent to the polymer dynamics than polymer-solvent interactions. At these concentrations, entanglements are the greatest decider in polymer mobility.

Conclusion

Spectrally resolved water, acetone, and HPMCAS self-diffusion coefficients were found by PGSE on mixtures of HPMCAS in 90% wt. acetone/10% wt. water solvent. The measurements allowed for comparison to the HPMCAS/acetone mixture data. The acetone diffusivity was roughly 25% less in the HPMCAS/90-10 solvent mixtures than the HPMCAS/acetone mixtures. The percent decrease in HPMCAS diffusivity was greatest, a 50% decrease, at 95% solvent and the diffusivities converged when solvent content decreased to 85%.The relationship between component free energy and diffusivity was observed, bridging thermodynamic and kinetic phenomena. Measurements on the self-diffusivity of HPMCAS in this solvent indicated an entanglement concentration near 95% wt. solvent and relationships between self-diffusivity, solvent goodness, and polymer radius were hypothesized. With such small differences in HPMCAS self-diffusivity between the HPMCAS/90-10 solvent mixtures and the HPMCAS/acetone mixtures, more diffusion coefficient measurements on

HPMCAS/90-10 solvent mixtures between 99% wt. and 95% wt. solvent as well as viscosity measurements of both solvent types are necessary to decisively conclude that the 90-10 solvent is a better solvent for HPMCAS.

APPENDIX B

SDD DRYING DROPLET MODEL MATLAB CODE

Notes on Code

The following MATLAB code, DiffWShell_Params.m, with its current parameters predicted the drying-time dependent mass fraction profiles and droplet radius seen in Figure 3.4. in July 2014. This code was built off of sphereDiffusion.m, which follows below and is easier to understand and run in MATLAB due to the normalized parameters, no shell, and the Robin boundary condition.

DiffWShell_Params.m

```
%A shell was implemented in order to capture a large
%evaporative flux at the bounday.
%The time steps are a polynomial function, S.T. there are smaller time
%steps at the start and bigger time steps at the end.
clear all;

R = 2E-5;        % radius of sphere [m]
shellThick= R/10;     %initial shell thickness
interface = R - shellThick; %location of interface betw. core and shell
final = 1;   % final time [s]
N = 10;         % number of spatial points including center and outer
%edge. Same for both core and shell.
M = 1000000;        % number of time steps including initial condition
h1 = interface/N;    % distance between spatial nodes in core not
%counting interface node N+1
h2 = shellThick/N; % not counting Radius node 2N+1
D = inline('4E-9*exp(-2.7183*(1-Ca))','Ca');     % diffusivity[m/s^2]
roe = 1000;        % density of droplet [kg/m^3]
roeace=roe;         %used to calculate the volume change due to
%evaporation. Currently density is assumed independent of wt. frac.

ECD = 1;        %ECD = 1 is equimolar counter diff. = 0 is conductively
%stagnant solute
%Parameters used for the evaporative flux calculation
roeg = 1.2; % kg/m^3  avg gas denisty in boundary layer
Dg = 1.3E-5; % m^2/s avg gas diffusivity in boundary layer
Sho = 2.6; %Sherwood Number
T=300; %T in K of droplet (for PsatP)
PsatP=exp(69.006+-5599.6/T+-7.0985*log(T)+6.2237E-6*T^2)/1.01325E5
%saturation pressure divided by total pressure [Pa/Pa]
Yfb = 0.1; %bulk acetone concentration
MWace = 58.08;
MWN2 = 28.01;
```

```
Cacore = 0.8*ones(1,N); %initial condition
Cashell = 0.8*ones(1,N+1); %initial condition for shell includes the
%shared point (interface)
Cainit=[Cacore, Cashell];
Caold=Cainit; % stores the nodal concentration values from the previous
%time step
Canew=Caold; %stores the nodal concentration values from the current
%time step
dR=0.0;      %the change in droplet radius between each time step

%setup plotting and storage
outCount=1;  % counts the number of saved concentration profiles
Nprofiles=50; %number of saved concentration profiles
txac = 0;    % if txac=0, allows for the time at which the mass fac. at
%center of droplet reaches a value to be placed onto the graph
xac = 0.3;   %the value that is deemed important for the center to
%reach
sol(:,outCount) = Canew;
pos(outCount,1) = 0.0; % pos holds the time and location of the Radius
pos(outCount,2) = R;
r = [linspace(0,interface-h1,N),linspace(interface,R,N+1)]; %initial
%nodal locations
rsave(:,outCount) = r;
figure('Color','white'); % white background for plot
plot(r*1E6,sol(:,outCount), 'b-'); %r is in um
title('Mass Fraction Profiles at Various time steps(time steps are
quadratially spaced)');
xlabel('Radius [um]');
ylabel('Mass Fraction of Acetone');
hold on;  % hold the plot so we can overlay later concentration
%profiles

%Solving the parabolic PDE in spherical coordinates by approximating
%the
%LHS with the forward difference approximation and the RHS with the
%central
%difference approximation
%this is "The Explicit Forward Euler Method"(pp.406 Yang, 2005)[58]

%loop through time.
for i=1:M
    time=final*(i/M)^2;
    dt=2*final/M*(i/M)^1;
    for j=2:N %loop through space. j=1 corresponds to r=0 and will be
%set equal to j=2 to satisfy the symmetry of flux.
        r(j) = (j-1)*h1;%location of jth node
        fraction = r(j)/interface; % fractional distance to interface
        if ECD == 1 % Equimolar counter diffusion
            Canew(j) = Caold(j) + dt * D(Caold(j)) * (Caold(j+1) - 2 *
Caold(j) + Caold(j-1)) / (h1^2); %RHS of parabolic PDE
            term3 = (-dR/dt * fraction)*(Caold(j+1) - Caold(j))/(h1);
% the virtual bulk flow
```

```
            Canew(j) = Canew(j) + dt * D(Caold(j))*(Caold(j+1) -
Caold(j-1)) / (r(j)*h1) + dt*term3;              %addition for
spherical coordinates
        elseif ECD == 0 % conductively stagnat solute
            Canew(j) = Caold(j) + dt * D(Caold(j)) * (2-Caold(j)) *
(Caold(j+1) - 2 * Caold(j) + Caold(j-1)) / ((1-Caold(j))^2*h1^2); %RHS
of parabolic PDE
            term3 = (-dR/dt * fraction)*(Caold(j+1) - Caold(j))/(h1);
% the virtual bulk flow
            Canew(j) = Canew(j) + dt * D(Caold(j)) * (Caold(j+1) -
Caold(j-1)) / (r(j)*h1*(1-Caold(j))) + dt*term3;
%addition for spherical coordinates
        end
    end
    %note that we are skipping Canew(N+1), the interface, which will be
caluclated via a
    %B.C. at the end
    for j=N+2:2*N %loop through space. j=1 corresponds to r=0 and will
be set equal to j=2 to satisfy the symmetry of flux.
        r(j) = N*h1+(j-N-1)*h2;%location of jth node
        fraction = 0.0; % currently no virtual bulk flow in the shell,
because interface and R move at same speed
        if ECD == 1 % Equimolar counter diffusion
            Canew(j) = Caold(j) + dt * D(Caold(j)) * (Caold(j+1) - 2 *
Caold(j) + Caold(j-1)) / (h2^2); %RHS of parabolic PDE
            term3 = (-dR/dt * fraction)*(Caold(j+1) - Caold(j))/(h2);
% the virtual bulk flow
            Canew(j) = Canew(j) + dt * D(Caold(j))*(Caold(j+1) -
Caold(j-1)) / (r(j)*h2) + dt*term3;              %addition for
spherical coordinates
        elseif ECD == 0 % conductively stagnat solute
            Canew(j) = Caold(j) + dt * D(Caold(j)) * (2-Caold(j)) *
(Caold(j+1) - 2 * Caold(j) + Caold(j-1)) / ((1-Caold(j))^2*h2^2); %RHS
of parabolic PDE
            term3 = (-dR/dt * fraction)*(Caold(j+1) - Caold(j))/(h2);
% the virtual bulk flow
            Canew(j) = Canew(j) + dt * D(Caold(j)) * (Caold(j+1) -
Caold(j-1)) / (r(j)*h2*(1-Caold(j))) + dt*term3;
%addition for spherical coordinates
        end
    end
    %note that we are skipping Canew(2N+1), the particle radius, which
will be caluclated via a
    %B.C. at the end

    %Implement B.C.'s
    Canew(1) = Canew(2);                    %no flux BC at r=0
    Canew(N+1) = h1*h2/(h1+h2)*(Canew(N)/h1+Canew(N+2)/h2); %equal mass
%flux on either side of interface
    %%%%%
    Yfsmol = Canew(2*N+1)/(Canew(2*N+1)^2-Canew(2*N+1)+1)*PsatP;
    Yfs = Yfsmol*MWace/(Yfsmol*MWace+(1-Yfsmol)*MWN2);
    Bm = (Yfs-Yfb)/(1-Yfs);
    Fm = (1+Bm)^0.7 * log(1+Bm)/Bm;
```

```
    Shm = 2+(Sho-2)/Fm;                    %modified Sherwood number
    Mflux = Dg/(2*R)*Shm*log(1+Bm);       %acetone mass flux from
%surface

    Canew(2*N+1) = Canew(2*N)/(1+Mflux*h2/(D(Caold(2*N+1))*roe));
%Robin B.C.: @ r=R, the flux from inside to the surface (D*dCa/dr) is
%equal to the flux from the surface to the bulk.
    r(N+1) = interface;
    r(2*N+1) = R;
    dR = -Mflux*dt/roeace;
    R = R+dR;
    interface = interface+dR;

    h1 = interface/N;    % distance between spatial nodes in core
    h2 = (R-interface)/N;
    if mod(i,M/Nprofiles) == 0
        outCount=outCount+1;  % increment outCount
        sol(:,outCount) = Canew;
        rsave(:,outCount) = r;
        pos(outCount,1) = time; % pos holds the time and location of
%the interface
        pos(outCount,2) = R;
        disp(pos(outCount,:));
        plot(rsave(:,outCount)*1E6,sol(:,outCount), 'b-'); %r is in um

    end
    if txac == 0
        if Canew(1) <=xac
            text(0.1,0.1,['time for mass fraction at droplet center to
equal ',num2str(xac),' = ',num2str(time),' s']);
            txac = 1;
        end
    end
    Caold=Canew;
end
figure('Color','white'); % white background for plot 2
title('The Simulated Droplet Radius')
xlabel('time (s)');
ylabel('Particle Radius(um)');
hold on
plot(pos(:,1),pos(:,2)*1E6); %radius is in um

%checking mass conservation; does the amount evaporated equal the
%initial minus final mass of acetone?
%note: assumes that roe=roeace
Maf=0;
Mai=0;
for k=1:2*N
    Maf=Maf + (Canew(k)+Canew(k+1))/2*(r(k+1)^3-r(k)^3); %the final
%mass of acetone in the droplet divided by 4/3pi*roe
    Mai=Mai + (Cainit(k)+Cainit(k+1))/2*(r(k+1)^3-r(k)^3); %the initial
%mass of acetone in the droplet divided by 4/3pi*roe
end
```

```
percentMconserved=100*(pos(1,2)^3-pos(end,2)^3)/(Mai-Maf); % the % of
mass that is conserved
display 'percent of mass conserved is:',percentMconserved,'%';
if abs(percentMconserved)-100> 10
    display 'WARNING: mass not conserved. Try more time steps';
end
```

sphereDiffusion.m

```
clear all;
R = 1.0;         % radius of sphere
final = 10.0;    % final time
N = 11;          % number of spatial points including center and outer
%edge
M = 10000;         % number of time steps including initial condition
dt = final/M;    % size of time step
h = R/(N-1);     % distance between spatial nodes
%D = inline('0.05*exp(-2.7183*(1-Ca))','Ca');     % diffusivity
D = inline('0.001+0*Ca','Ca');
kc = 2;          % external mass transfer coefficient
roe = 1;         % density of droplet
ECD = 1;         %ECD = 1 is equimolar counter diff. = 0 is conductively
%stagnant solute

Ca = 0.8*ones(1,N); %initial condition

Caold=Ca;
Canew=Caold;
dR=0.0;
%Solving the parabolic PDE in spherical coordinates by approximating
% the LHS with the forward difference approximation and the RHS with
% the central difference approximation
%this is called "The Explicit Forward Euler Method" (pp.406 Yang)

% step 4: setup plotting and storage

outCount=1;  % counts the number of saved concentration profiles
sol(:,outCount) = Canew;
pos(outCount,1) = 0.0; % pos holds the time and location of the Radius
pos(outCount,2) = R;
r = linspace(0,R,N); %initial nodal locations
figure('Color','white'); % white background for plot
plot(r,sol(:,outCount), 'b-');
xlabel('Radius');
ylabel('Ca');
hold on;  % hold the plot so we can overlay later temperature profiles

for i=1:M           %loop through time.
    time=i*dt;
```

```
    for j=2:N-1%loop through space. j=1 corresponds to r=0 and will be
%set equal to j=2 to satisfy the symmetry of flux.
        r(j) = (j-1)*h;%location of jth node
        fraction = r(j)/R; % fractional distance to Radius
        if ECD == 1 % Equimolar counter diffusion
            Canew(j) = Caold(j) + dt * D(Caold(j)) * (Caold(j+1) - 2 *
Caold(j) + Caold(j-1)) / (h^2); %RHS of parabolic PDE
            term3 = (-dR/dt * fraction)*(Caold(j+1) - Caold(j))/(h);
% the virtual bulk flow
            Canew(j) = Canew(j) + dt * D(Caold(j))*(Caold(j+1) -
Caold(j-1)) / (r(j)*h) + dt*term3;               %addition for
%spherical coordinates
        elseif ECD == 0 % conductively stagnat solute
            Canew(j) = Caold(j) + dt * D(Caold(j)) * (2-Caold(j)) *
(Caold(j+1) - 2 * Caold(j) + Caold(j-1)) / ((1-Caold(j))^2*h^2); %RHS
%of parabolic PDE
            term3 = (-dR/dt * fraction)*(Caold(j+1) - Caold(j))/(h);
% the virtual bulk flow
            Canew(j) = Canew(j) + dt * D(Caold(j)) * (Caold(j+1) -
Caold(j-1)) / (r(j)*h*(1-Caold(j))) + dt*term3;               %addition
%for spherical coordinates
        end
    end
    Canew(1) = Canew(2);                    %no flux BC at r=0
    Canew(N) = Canew(N-1)/(1.0+h* kc/D(Caold(N)));  %Robin B.C.: @ r=R,
%the flux from inside to the surface (D*dCa/dr) is equal to the flux
%from the surface to the bulk (-k*(Ca-Cao)) Cao is set to zero now.
    r(N) = R;
    dR = -kc*dt*(Caold(N)+Canew(N))/(2*roe);
    R = R+dR;
    h = R/(N-1);
    if mod(i,1000) == 0
        outCount=outCount+1;  % increment outCount
        sol(:,outCount) = Canew;
        pos(outCount,1) = time; % pos holds the time and location of
%the interface
        pos(outCount,2) = R;
        disp(pos(outCount,:));
        plot(r,sol(:,outCount), 'b-');
    end

    Caold=Canew;
end
figure('Color','white'); % white background for plot 2
xlabel('time (s)');
ylabel('Particle Radius(m)');
hold on
plot(pos(:,1),pos(:,2));
%plot(r,Ca);
%plot(Ca');
```

REFERENCES CITED

1. Handscomb, C.S., M. Kraft, and A.E. Bayly, *A new model for the drying of droplets containing suspended solids.* Chemical Engineering Science, 2009a. **64**(4): p. 628-637.

2. Callaghan, P.T., *Translational Dynamics and Magnetic Resonance,* 2011. Oxford University Press Inc.

3. Kubo, R., *A Stochastic Theory of Line-Shape and Relaxation,* in *Fluctuation, Relaxation and Resonance in Magnetic Systems,* D.t. Haar, Editor 1962, Oliver and Boyd: Edinburgh.

4. Hahn, E.L., *Spin Echoes.* Physical Review, 1950. **80**(4): p. 580-594.

5. Bloch, F., *Nuclear Induction.* Physical Review, 1946. **70**(7-8): p. 460-474.

6. Bloembergen, N., E.M. Purcell, and R.V. Pound, *Relaxation Effects in Nuclear Magnetic Resonance Absorption.* Physical Review, 1948. **73**(7): p. 679-712.

7. Abragam, A., *The principles of nuclear magnetism*. The International series of monographs on physics, 1961. Oxford, Clarendon Press.

8. Haberman, R., *Applied partial differential equations : with Fourier series and boundary value problems*. 4th ed, 2004. Upper Saddle River, N.J.: Pearson Prentice Hall.

9. Carr, H.Y. and E.M. Purcell, *Effects of Diffusion on Free Precession in Nuclear Magnetic Resonance Experiments.* Physical Review, 1954. **94**(3): p. 630-638.

10. Meiboom, S. and D. Gill, *Modified Spin-Echo Method for Measuring Nuclear Relaxation Times.* Review of Scientific Instruments, 1958. **29**(8): p. 688-691.

11. Vold, R.L., et al., *Measurement of Spin Relaxation in Complex Systems.* Journal of Chemical Physics, 1968. **48**(8): p. 3831-&.

12. Einstein, A., *The motion of elements suspended in static liquids as claimed in the molecular kinetic theory of heat.* Annalen Der Physik, 1905. **17**(8): p. 549-560.

13. *Product catalog AQOAT (HPMC-AS, Hypromellose-Acetate-Succinate)* [cited May 28th 2014]; Available from: http://www.harke.com/en/products/aqoat-hpmc-as-hypromellose-acetate-succinate.html.

14. Rubinstein, M. and R.H. Colby, *Polymer physics,* 2003. Oxford ; New York: Oxford University Press.

15. Zimm, B.H., *Dynamics of Polymer Molecules in Dilute Solution - Viscoelasticity, Flow Birefringence and Dielectric Loss.* Journal of Chemical Physics, 1956. **24**(2): p. 269-278.

16. Rouse, P.E., *A Theory of the Linear Viscoelastic Properties of Dilute Solutions of Coiling Polymers.* Journal of Chemical Physics, 1953. **21**(7): p. 1272-1280.

17. de Gennes, P.G., *Reptation of a Polymer Chain in Presence of Fixed Obstacles.* Journal of Chemical Physics, 1971. **55**(2): p. 572

18. Callaghan, P.T. and A. Coy, *Evidence for Reptational Motion and the Entanglement Tube in Semidilute Polymer-Solutions.* Physical Review Letters, 1992. **68**(21): p. 3176-3179.

19. Komlosh, M.E. and P.T. Callaghan, *Segmental motion of entangled random coil polymers studied by pulsed gradient spin echo nuclear magnetic resonance.* Journal of Chemical Physics, 1998. **109**(22): p. 10053-10067.

20. Vrentas, J.S. and J.L. Duda, *Diffusion in Polymer - Solvent Systems .1. Re-Examination of Free-Volume Theory.* Journal of Polymer Science Part B-Polymer Physics, 1977. **15**(3): p. 403-416.

21. Vrentas, J.S. and J.L. Duda, *Diffusion in Polymer-Solvent Systems .2. Predictive Theory for Dependence of Diffusion-Coefficients on Temperature, Concentration, and Molecular-Weight.* Journal of Polymer Science Part B-Polymer Physics, 1977. **15**(3): p. 417-439.

22. Danner, R.P., *Measuring and correlating diffusivity in polymer solvent systems using free-volume theory.* Fluid Phase Equilibria, 2014. **362**: p. 19-27.

23. Ferry, J.D., *Viscoelastic properties of polymers*. 3d ed, 1980. New York: Wiley.

24. Yapel, R.A., et al., *Mutual and Self-Diffusion of Water in Gelatin - Experimental-Measurement and Predictive Test of Free-Volume Theory.* Polymer, 1994. **35**(11): p. 2411-2416.

25. Bearman, R.J., *On Molecular Basis of Some Current Theories of Diffusion.* Journal of Physical Chemistry, 1961. **65**(11): p. 1961

26. Tester, J.W. and M. Modell, *Thermodynamics and its applications*. 3rd ed. Prentice-Hall, 1997. Upper Saddle River, N.J.

27. Hong, S.U., *Prediction of Polymer-Solvent Diffusion Behavior Using Free-Volume Theory.* Industrial & Engineering Chemistry Research, 1995. **34**(7): p. 2536-2544.

28. Zielinski, J.M. and J.L. Duda, *Predicting Polymer Solvent Diffusion-Coefficients Using Free-Volume Theory.* Aiche Journal, 1992. **38**(3): p. 405-415.

29. Chaikin, P.M. and T.C. Lubensky, *Principles of condensed matter physics*, 1995. Cambridge ; New York, NY, USA: Cambridge University Press.

30. Fox, T.G. and P.J. Flory, *2nd-Order Transition Temperatures and Related Properties of Polystyrene .1. Influence of Molecular Weight.* Journal of Applied Physics, 1950. **21**(6): p. 581-591.

31. Mallamace, F., et al., *The role of the dynamic crossover temperature and the arrest in glass-forming fluids.* European Physical Journal E, 2011. **34**(9).

32. Mallamace, F., et al., *Transport properties of glass-forming liquids suggest that dynamic crossover temperature is as important as the glass transition temperature.* Proceedings of the National Academy of Sciences of the United States of America, 2010. **107**(52): p. 22457-22462.

33. Angell, C.A., *Liquid fragility and the glass transition in water and aqueous solutions.* Chemical Reviews, 2002. **102**(8): p. 2627-2649.

34. de Wijn, A.S., et al., *Criticality in Dynamic Arrest: Correspondence between Glasses and Traffic.* Physical Review Letters, 2012. **109**(22).

35. Vrentas, J.S., H.T. Liu, and J.L. Duda, *Effect of Solvent Size on Diffusion in Polymer-Solvent Systems.* Journal of Applied Polymer Science, 1980. **25**(8): p. 1793-1797.

36. Fox, T.G., *Influence of Diluent and of Copolymer Composition on the Glass Temperature of a Polymer System.* Bulletin of the American Physical Society, 1956. **1**(2): p. 123.

37. Fox, T.G. and P.J. Flory, *The Glass Temperature and Related Properties of Polystyrene - Influence of Molecular Weight.* Journal of Polymer Science, 1954. **14**(75): p. 315-319.

38. Fox, T.G. and S. Loshaek, *Influence of Molecular Weight and Degree of Crosslinking on the Specific Volume and Glass Temperature of Polymers.* Journal of Polymer Science, 1955. **15**(80): p. 371-390.

39. Angell, C.A., *Formation of Glasses from Liquids and Biopolymers.* Science, 1995. **267**(5206): p. 1924-1935.

40. Bend Research Inc., *Tg/T as a measure of long-term SDD stability.* 2014. Personal communicaiton.

41. Edzes, H.T., D. van Dusschoten, and H. Van As, *Quantitative T-2 imaging of plant tissues by means of multi-echo MRI microscopy.* Magnetic Resonance Imaging, 1998. **16**(2): p. 185-196.

42. Xiang, Q.S. and O. Nalcioglu, *A Formalism for Generating Multiparametric Encoding Gradients in Nmr Tomography.* Ieee Transactions on Medical Imaging, 1987. **6**(1): p. 14-20.

43. Torrey, H.C., *Bloch Equations with Diffusion Terms.* Physical Review, 1956. **104**(3): p. 563-565.

44. Stejskal, E.O. and J.E. Tanner, *Spin Diffusion Measurements: Spin Echoes in the Presence of a Time-Dependent Field Gradient.* Journal of Chemical Physics, 1965. **42**(1): p. 288.

45. Callaghan, P.T., et al., *Recent Fourier and Laplace perspectives for multidimensional NMR in porous media.* Magnetic Resonance Imaging, 2007. **25**(4): p. 441-444.

46. Washburn, K.E. and P.T. Callaghan, *Tracking pore to pore exchange using relaxation exchange spectroscopy*. Physical Review Letters, 2006. **97**(17).

47. Moller, J.T. and S. Fredsted, *A Primer on Spray Drying.* Chemical Engineering, 2009. **116**(12): p. 34-40.

48. Friesen, D.T., et al., *Hydroxypropyl Methylcellulose Acetate Succinate-Based Spray-Dried Dispersions: An Overview*. Molecular Pharmaceutics, 2008. **5**(6): p. 1003-1019.

49. Handscomb, C.S., M. Kraft, and A.E. Bayly, *A new model for the drying of droplets containing suspended solids after shell formation.* Chemical Engineering Science, 2009b. **64**(2): p. 228-246.

50. Handscomb, C.S. and M. Kraft, *Simulating the structural evolution of droplets following shell formation.* Chemical Engineering Science, 2010. **65**(2): p. 713-725.

51. Cheong, H.W., G.V. Jeffreys, and C.J. Mumford, *A Receding Interface Model for the Drying of Slurry Droplets.* Aiche Journal, 1986. **32**(8): p. 1334-1346.

52. Felder, R.M. and R.W. Rousseau, *Elementary principles of chemical processes*. 3rd ed2005, Hoboken, NJ: Wiley. xxvi, 675 p.

53. Shallcross, D.C., *Psychrometric charts for hydrocarbon vapours in nitrogen.* Calphad-Computer Coupling of Phase Diagrams and Thermochemistry, 1996. **20**(3): p. 273-288.

54. Bird, R.B., W.E. Stewart, and E.N. Lightfoot, *Transport phenomena*. revised 2nd ed., Wiley international ed., 2007. New York: J. Wiley.

55. Masaro, L. and X.X. Zhu, *Physical models of diffusion for polymer solutions, gels and solids.* Progress in Polymer Science, 1999. **24**(5): p. 731-775.

56. Abramzon, B. and W.A. Sirignano, *Droplet Vaporization Model for Spray Combustion Calculations.* International Journal of Heat and Mass Transfer, 1989. **32**(9): p. 1605-1618.

57. Clague, D.S. and R.J. Phillips, *A numerical calculation of the hydraulic permeability of three-dimensional disordered fibrous media.* Physics of Fluids, 1997. **9**(6): p. 1562-1572.

58. Yang, W.n.-y.n., *Applied numerical methods using MATLAB,* 2005. Hoboken, N.J.: Wiley-Interscience.

59. Perry, R.H. and D.W. Green, *Perry's chemical engineers' handbook*. 8th ed., 2008. New York: McGraw-Hill.

60. Guillermo, A., M. Todica, and J.P. Cohenaddad, *Nuclear-Magnetic-Resonance Observation of Cyclohexane Self-Diffusion in Concentrated Polybutadiene Solutions.* Macromolecules, 1993. **26**(15): p. 3946-3952.

61. Dealy, J.M., *Weissenberg and Deborah Numbers - Their Definition and Use.* Rheology Bulletin, 2010. **79**(2): p. 14-18.

62. Reiner, M., *The Deborah Number.* Physics Today, 1964. **17**(1): p. 62-62.

63. Colby, R.H., *Structure and linear viscoelasticity of flexible polymer solutions: comparison of polyelectrolyte and neutral polymer solutions.* Rheologica Acta, 2010. **49**(5): p. 425-442.

64. Gao, P. and P.E. Fagerness, *Diffusion in Hpmc Gels .1. Determination of Drug and Water Diffusivity by Pulsed-Field-Gradient Spin-Echo Nmr.* Pharmaceutical Research, 1995. **12**(7): p. 955-964.

65. Ferrero, C., et al., *Towards elucidation of the drug release mechanism from compressed hydrophilic matrices made of cellulose ethers. I. Pulse-field-gradient spin-echo NMR study of sodium salicylate diffusivity in swollen hydrogels with respect to polymer matrix physical structure.* Journal of Controlled Release, 2008. **128**(1): p. 71-79.

66. von Meerwall, E.D., E.J. Amis, and J.D. Ferry, *Self-Diffusion in Solutions of Polystyrene in Tetrahydrofuran - Comparison of Concentration Dependences of*

the Diffusion-Coefficients of Polymer, Solvent, and a Ternary Probe Component. Macromolecules, 1985. **18**(2): p. 260-266.

67. de Gennes, P.G., *Dynamics of Entangled Polymer-Solutions .2. Inclusion of Hydrodynamic Interactions.* Macromolecules, 1976. **9**(4): p. 594-598.

68. Naumann, C., et al., *"Setting Paint" Analogy for the Hydrophobic Self-Association of Tropoelastin into Elastin-like Hydrogel.* Biopolymers, 2009. **91**(5): p. 321-330.

69. Mills, R., *Self-Diffusion in Normal and Heavy-Water in Range 1-45 Degrees.* Journal of Physical Chemistry, 1973. **77**(5): p. 685-688.

70. Tomlinson, D.J., *Temperature dependent self-diffusion coefficient measurements of glycerol by the pulsed N.M.R. technique.* Molecular Physics, 1973. **25**(3): p. 735-738.

71. Hodge, I.M., *Physical Aging in Polymer Glasses.* Science, 1995. **267**(5206): p. 1945-1947.

72. Bend Research Inc., *Acetone glass transition temperature*, 2013. Personal communication.

73. Ashland. *AquaSolve ant AquaSolve AS hydroxypropylmethylcellulose acetate succinate physical and chemical properties handbook*. [cited June 22, 2014]; Available from: http://www.ashland.com/Ashland/Static/Documents/ASI/PC_12624_AquaSolve_AS_Handbook.pdf.

74. Shin-Etsu Chemical Co., L. *Shin-Etsu AQOAT (Hypromellose Acetate Succinate)*. [cited April 22, 2014]; Available from: http://www.metolose.jp/e/pharmaceutical/aqoat.shtml.

75. Danner, R.P., *Mutual diffusivity at infinite dilution of acetone in HPMCAS.* 2014. Personal communications.

76. Duda, J.L., et al., *Prediction of Diffusion-Coefficients for Polymer-Solvent Systems.* Aiche Journal, 1982. **28**(2): p. 279-287.

77. Doi, M., *Introduction to Polymer Physics*, 1995. Oxford University Press Inc.

78. Freed, K.F. and S.F. Edwards, *Polymer Viscosity in Concentrated Solutions.* Journal of Chemical Physics, 1974. **61**(9): p. 3626-3633.

79. de Gennes, P.G., *Dynamics of Entangled Polymer-Solutions .1. Rouse Model.* Macromolecules, 1976. **9**(4): p. 587-593.

80. Washburn, K.E. and J.E. Birdwell, *Updated methodology for nuclear magnetic resonance characterization of shales.* Journal of Magnetic Resonance, 2013. **233**: p. 17-28.

81. Tanaka, F. and S.F. Edwards, *Viscoelastic Properties of Physically Cross-Linked Networks - Transient Network Theory.* Macromolecules, 1992. **25**(5): p. 1516-1523.

82. Shapiro, Y.E., *Structure and dynamics of hydrogels and organogels: An NMR spectroscopy approach.* Progress in Polymer Science, 2011. **36**(9): p. 1184-1253.

83. Brand, T., et al., *NMR study of the gelation of a designed gelator.* Magnetic Resonance in Chemistry, 2008. **46**(6): p. 545-549.